

AD-A145 672

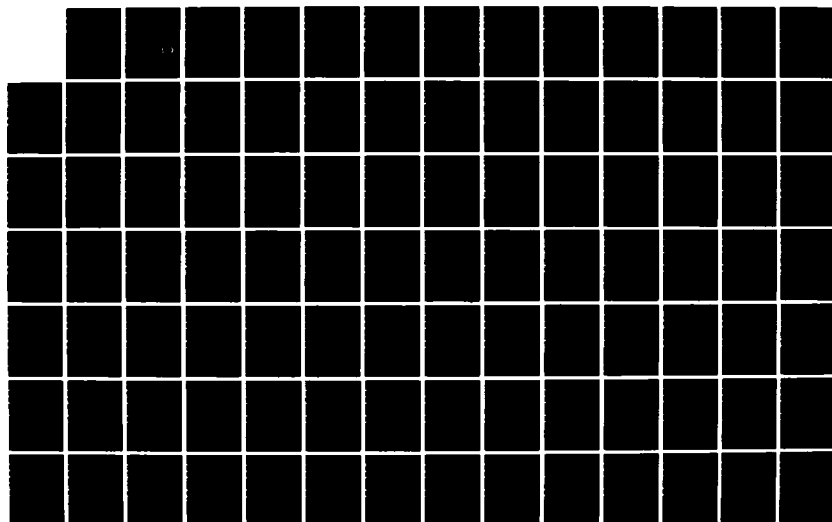
ACOUSTIC SCATTERING CROSS SECTIONS FOR TRULY COMPOSITE
WIND-WAVE SURFACES. (U) MIDDLETON (DAVID) NEW YORK
D MIDDLETON 20 AUG 84 NUSC-TD-7205 N00140-83-M-NA11

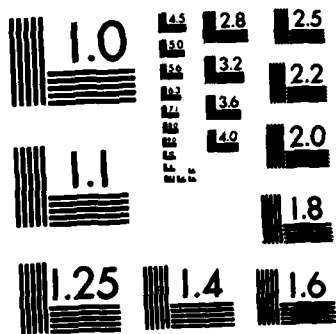
1/2

UNCLASSIFIED

F/G 20/1

NL





MICROCOPY RESOLUTION TEST CHART
NATIONAL BUREAU OF STANDARDS-1963-A

12

NUSC Technical Document 7205
20 August 1984

Acoustic Scattering Cross Sections for Truly Composite Wind-Wave Surfaces: Scattering Without Bubbles

David Middleton
(Consultant)

Associate Technical Director
for Technology

AD-A145 672



DTIC
ELECTE
SEP 17 1984
S B

DTIC FILE COPY

Naval Underwater Systems Center
Newport, Rhode Island / New London, Connecticut

Approved for public release;
distribution unlimited.

84 09 10 076

Preface

This work was accomplished under NUSC Project No. A67001, "Weapons Environmental Acoustics Program — Project WEAP," Principal Investigator, W. I. Roderick (Code 10). The sponsoring activity is the Naval Sea Systems Command, C. D. Smith (SEA-63R), Director. Funding is provided under Program Element 62759N, Subproject Program No. SF59-554, R. L. Martin (NORDA 110A), Manager. This document was prepared for the Research and Technology Staff by David Middleton, 127 E. 91 Street, New York, NY 10128, contract numbers N00140-83-M-NA11 (1983), N00140-83-C-KA23 and N00140-83-M-LZ39 (1983, 1984).

The Technical Reviewer for this document was William I. Roderick (Code 10).

Acknowledgments

The author wishes particularly to thank Dr. William I. Roderick for his strong interest in, and critique of, this research. The author also wishes to thank Dr. Robert Mellen (recently of NUSC) for his suggestions and comments regarding the possible soliton mechanism introduced in this study.

Reviewed and Approved: 20 August 1984



W. A. Von Winkle
Associate Technical Director for Technology

The principal investigator of this document is located at the
New London Laboratory, Naval Underwater Systems Center,
New London, Connecticut 06320.

Unclassified

SECURITY CLASSIFICATION OF THIS PAGE (When Data Entered)

REPORT DOCUMENTATION PAGE		READ INSTRUCTIONS BEFORE COMPLETING FORM
1. REPORT NUMBER TD 7205	2. GOVT ACCESSION NO.	3. RECIPIENT'S CATALOG NUMBER
4. TITLE (and Subtitle) ACOUSTIC SCATTERING CROSS SECTIONS FOR TRULY COMPOSITE WIND-WAVE SURFACES: SCATTERING WITHOUT BUBBLES		5. TYPE OF REPORT & PERIOD COVERED Technical Report Feb. , 1983 - April 19, 1984
7. AUTHOR(s) David Middleton		6. PERFORMING ORG. REPORT NUMBER
9. PERFORMING ORGANIZATION NAME AND ADDRESS Dr. David Middleton 127 E. 91 St. New York, NY 10128		8. CONTRACT OR GRANT NUMBER(s) N00140-83-M-NA11 N00140-83-C-KA23 N00140-84-M-LZ39
11. CONTROLLING OFFICE NAME AND ADDRESS Naval Underwater Systems Center, Code 10 New London, Conn. 06320		10. PROGRAM ELEMENT, PROJECT, TASK AREA & WORK UNIT NUMBERS
14. MONITORING AGENCY NAME & ADDRESS (if different from Controlling Office)		12. REPORT DATE 20 August 1984
		13. NUMBER OF PAGES 127 + x
		15. SECURITY CLASS. (of this report) Unclassified
		15a. DECLASSIFICATION/ DOWNGRADING SCHEDULE
16. DISTRIBUTION STATEMENT (of this Report) Approved for public release; distribution unlimited.		
17. DISTRIBUTION STATEMENT (of the abstract entered in Block 20, if different from Report)		
18. SUPPLEMENTARY NOTES		
19. KEY WORDS (Continue on reverse side if necessary and identify by block number) Underwater acoustic scattering; scattering cross sections; backscatter; Bragg scatter; soliton ripples; wind waves; wave surfaces; gravity- capillary wave surface; no bubbles; high frequency scatter; gaussian beam patterns; grazing angles; numerical examples; diffraction.		
20. ABSTRACT (Continue on reverse side if necessary and identify by block number) Underwater acoustic scattering cross sections for truly composite wind- wave surfaces are obtained analytically, where the composite surface consists of the usual single gravity-capillary wave surface and an independent ripple structure which rides upon the former. The latter consists of an ensemble of solitons, as hydraulic jumps, moving nondispersively in a very thin (moving) surface layer of the gravity-capillary waves. These soliton-ripples are postulated to provide a scattering mechanism of sufficient strength		

DD FORM 1473
1 JAN 73

EDITION OF 1 NOV 65 IS OBSOLETE
S/N 0102- LF- 014- 6601

Unclassified

SECURITY CLASSIFICATION OF THIS PAGE (When Data Entered)

Unclassified

SECURITY CLASSIFICATION OF THIS PAGE (When Data Entered)

potentially to account for the often large observed discrepancies $O(10-20 \text{ db})$ in the (back-)scattering cross sections between conventional theory and experiment when high frequencies $O(>10 \text{ kHz})$ and small grazing angles $O(5-20^\circ)$ are employed, without the assumption of near-surface bubble mechanisms. This is particularly important for the frequent situations when bubbles are demonstrably lacking, even at mean wind speeds up to $O(10 \text{ m/sec} = 20 \text{ knots})$, and possibly higher. Here, the "capillary" component of the gravity-capillary wave continuum is not large enough by itself to provide sufficient Bragg scatter, while the soliton-ripples appear capable of so doing. Of course, if near-surface bubbles are verified to be present in sufficient numbers, they by themselves, or with the soliton-ripples, can account for the noticeably larger (back-)scatter cross sections obtained experimentally.

New features of the present study are: (1) identification of the soliton-ripple phenomenon with its second-order statistical properties, e.g., correlation functions and wave number spectra, as a significant potential scattering mechanism; (2) development of a truly two-component wave surface model employing these ripples, and (3) determination of the resulting mono- and bi-static (acoustic) cross sections, for both incoherent and coherent scatter; (4) verification of general agreement between various analytic procedures and their results, which indicates that the problem of reconciliation between the observed data and calculated results (in the aforementioned cases of high-frequency, small grazing angles) lies in the choice of the physical model, which becomes particularly critical when there are no (or negligible) bubbles. (5) We note, also, that the contributions of diffraction are ignorable vis-à-vis the direct scatter terms of the (necessarily approximate) theory used above to obtain the scatter cross sections. A specific numerical example (20 kHz, 10 m/sec average wind, and 10° grazing angle) is used for numerical results and comparisons with previous approaches. Here gaussian and gaussian and omni-beam patterns are explicitly employed, and the quantitative rôle of the various approximations is extensively explored. A homogeneous Helmholtz medium is assumed, with absorption and no gradients ($\nabla c = 0$). The wind-wave surface is postulated to be locally stationary and homogeneous.

Finally, we stress that at this stage the soliton-ripple scattering mechanism, while promising, has not yet been established as such experimentally: its existence is not questioned, but its scattering properties remain to be verified.

S/N 0102- LF- 014- 6601

Unclassified

SECURITY CLASSIFICATION OF THIS PAGE(When Data Entered)

TABLE OF CONTENTS

List of Figures	viii
List of Principal Symbols	ix
1. Introduction	1
Part I. Acoustic Scattering Cross Sections	
2. Scattering Cross Sections for Composite Wave Surfaces	5
2.1 The New Wave-Surface Model: Surface Elevation	5
2.2 Scattering Cross-Sections: Definitions	8
A. Incoherent Scattering Cross Sections, $\sigma_{inc}^{(0)}$	9
B. Coherent Scattering Cross Sections, $\sigma_{coh}^{(0)}$	12
C. The Reference Area, A_{REF}	12
2.3 "High-Frequency" Scattering Cross Sections	13
A. Backscatter ($R \neq T$)	18
B. Bistatic Scatter in the Snell Direction ($R \neq T$)	19
2.4 "Low-Frequency" Acoustic Scatter Cross Sections	20
A. Backscatter	21
B. Bistatic Scatter in the Snell Direction	23
2.5 Analytic Comparisons with Recent Results	24
A. Tolstoy and Clay	24
B. McDaniel and Gorman	26
C. Kur'yanov	29
D. Barrick and Bahar	30
3. Preliminary Numerical Results: High Frequencies and Small Grazing Angles	32
3.1 Backscatter with Soliton Ripples: Numerical Examples	33
A. Calculations	33
B. Wave Number Spectra	34
C. A Numerical Example	36
3.2 Backscatter from Capillary Waves	38
A. Phillips' Spectrum	38
B. Brown's Spectrum	39
C. McDaniel's and Gorman's Results	40
3.3 Backscatter from Diffraction Terms ($k \geq 1$)	40

4.	Conclusions and Next Steps	42
4.1	Principal Results	42
4.2	Suggested Next Steps	46
	A. Some Experimental Topics	46
	B. Theoretical Extensions	46
	Part II. Analytical Models	
5.	The Received Scattered Field	47
5.1	The Received Scattered Field, I: Formulation	47
5.2	The Unscattered Field	50
5.3	Absorption and Doppler	51
5.4	The Received Scattered Field, II: Canonical Forms and Geometry	53
5.5	Discussion and Critique	60
6.	Beam Patterns and Apertures	62
6.1	Beam Patterns and Projections	63
6.2	Remarks	67
6.3	The "Narrow-Beam" Case	70
	A. Backscatter Geometry: $R\theta T$ (identical beams)	70
	B. Forward Scatter Geometry: <i>Specular Direction</i> (identical beams)	71
	C. Backscatter Geometry (Gauss x Omni): $\phi_L = 0$	71
	D. Forward Scatter Geometries (Gauss x Omni), in the Specular Direction	72
6.4	Beam Convolutions	74
6.5	Beam Integrals for Scatter Intensities	76
	A. Approximations	79
	A.1 Change of Dimensions	80
	B. Explicit Forms: b_{TR} , $2\alpha_0 - b_{TR}$	81
	C. Projected Beam Area on the Reference Wave Surface ($\langle \zeta \rangle = 0$)	82
	D. The Reference Surface Area, A_{REF}	83
6.6	Summary Remarks	84
7.	Surface Models: General Scatter Intensity	86
7.1	Wave Surface Models	87
7.2	The Second-Moment Functions of the Received Scattered Field, $X(t)$	89
	A. Total "Classical" Component $k = 0$	89
	B. The Coherent Component ($k = 0$).	90
	C. Higher-Order (Diffraction) Terms ($k \geq 1$).	91

7.3	Explicit Surface Scatter Statistics: Two-Scale Models	92
A.	The Coherent Component ($k = 0$)	93
B.	The Incoherent Component ($k = 0$).	95
C.	Remarks on Spectra and Covariance Functions	100
D.	Capillary Wave-Number Spectra	104
7.4	Extensions	106
A.	The Diffraction Terms ($k \geq 1$)	106
B.	The Evaluation of the "Tilt-Factor," $N_{G-inc}^{(0)}$	107
C.	Shadowing Functions \bar{S} , \bar{S}^2	109
8.	Limiting Cases of Scatter Intensities for Random, Two-Scale Surface Models	110
8.1	Scattering Intensities: General Forms for "High Frequencies".	110
8.2	Scattering Intensities: General Forms for "Low Frequencies" .	113
8.3	(Monostatic) Backscatter Intensities	114
8.4	(Bistatic) Scatter Intensities	116
8.5	Scatter Intensity of the Diffuse Diffraction Term ($k = 1$) . .	117
8.6	Extension to Include Explicit Capillary Waves	118
A.	The Coherent Component ($k = 0$)	119
B.	The Incoherent Component ($k = 0$).	120
9.	References	123

Accession For	
NTIS GRA&I	<input checked="checked" type="checkbox"/>
DTIC TAB	<input type="checkbox"/>
Unannounced	<input type="checkbox"/>
Justification	
By _____	
Distribution/	
Availability Codes	
Dist	Avail and/or Special
A-1	



LIST OF ILLUSTRATIONS

Figure		Page
2.1	Cross-section of a moving wind-wave surface, showing soliton ripples (greatly exaggerated) riding on the gravity-capillary wave surface ζ_G	7
2.2a	Backscatter geometry (far-field): monostatic scattering ($R \equiv T$), vide Fig. 5.1	9
2.2b	Bistatic scattering ($R \neq T$); "forward" or oblique scattering geometry, vide Fig. 5.1	9
5.1	Geometry of the transmitter ($@ O_T$), wave surface (Σ), receiver (at O_R), showing surface elevation ζ above $\zeta = 0: S_0$, and the common region of illumination (shaded), on S_0 , due to overlapping beam patterns Q_T, Q_R : (here $\nabla c = 0$)	56
6.1	Geometry of effective beam width, $\Delta\beta_T$, in the far-field, $r_{b-\max}/R_{OT} \ll 1$, showing illumination by "short" pulses . . .	72

LIST OF PRINCIPAL SYMBOLS

A_0 = signal amplitude	$G^{(1)}$ = geometric factor, with absorption
A_R = receiver aperture weighting	G_T = source function
A_{RT} = beam integral	g_∞ = green's function
A, A_T = beam-pattern parameter	g = gravitational acceleration (also, subscript)
A_{REF}, A_1 = beam-projected surface areas	g_T, g_R = aperture gain factors
$Q_{T,R}$ = beam patterns	G = gravity-capillary wave surface
a_T = beam pattern parameter	I_1, I_2, I_3 = beam integrals
$\hat{\alpha}_1, \hat{\alpha}_0$ = wave direction angles	\hat{I} = unit dyadic
$2\alpha_0$ = (vector) angular direction function	$\hat{i}_x, \hat{i}_y, \hat{i}_z, \hat{i}_{OR}, \hat{i}_{OT}$ = unit vectors
α_H = (homogeneous) acoustic field	$J_{c,g}$ = surface curvature measure
$\hat{a}_{OT,OR}$ = beam dyadics	K_a, K_S = directional covariances
\hat{A} = aperture dyadic	K_{0-in} = intensity of applied signal
\hat{B}_{TR} = composite beam dyadic	$\underline{K}, \underline{K}_S$ = (vector) wave numbers
B, B_T = beam pattern parameter; also a spectrum level	$k, k_0, \underline{k}, \underline{k}_D$ = wave numbers
b = scaling factor	$\underline{\xi}, \underline{\xi}_0$ = source element locations
$b_0 = \cos\theta_{OT} + \cos\theta_{OR} = 2\alpha_{OZ}$	L_S = { spatial duration of soliton
b_T = beam pattern parameter	L_0 = { (horizontal) separation between source and receiver
b_{TR} = beam pattern parameter	ℓ_c, ℓ_S, ℓ_g = (horizontal) correlation distances
ΔB = beam width	λ_0 = acoustic wavelength in water
$\langle \rangle$ = statistical averages	$\ell_{Tx}, \ell_{Rx}, \text{etc.}$ } = aperture dimensions
C = beam parameter	$\ell_{x,y,z}$
c_0 = (min.) wave propagation speed in water	\hat{M}_∞ = green's function operator
D = beam parameter	$M_{\langle X \rangle}, M_{X-\langle X \rangle}, M_X$ = second-moment function of received scattered waves
$\delta, \delta_{tt}, \delta_{RR}$ = delta functions	
\hat{D} = surface dyadic	
$\hat{\eta}_\infty$ = field renormalization operator	
F_1, F_2 = characteristic functions	
\mathfrak{F} = fourier transform operator	
f_s = wave frequency	

$N_{GS}^{(0)}, N_{Gc}^{(0)}$ = "tilt" factor

\hat{n} = unit normal

\hat{n}_G = unit normal to surface G

$\underline{v}, \underline{v}_R, \underline{v}_T, \underline{v}_0$ = vector spatial frequency;
 $v = |\underline{v}|$

$\Delta v(k)$ = fluctuation density

$\hat{1}$ = unit operator

ω_0, ω_s = angular frequencies

$\Psi(k)$ = wave number spectrum

ϕ_{OT}, ϕ_{OR} = beam angles

ϕ_T, ϕ_R = beam pattern phases

$\hat{Q}, \hat{Q}_{S,V}$ = scattering operators

$Q^{(k)}$ = weighting function

\hat{R} = receiver operator

R_G, R_g = Raleigh numbers

R_{OT}, R_{OR} = source and receiver distances

R = spatial distance

R_0 = reflection coefficient

$\underline{r} = \hat{i}_x x + \hat{i}_y y$ = vector in (x,y)-plane

ρ, ρ_S = normalized covariances

$\underline{\rho}$ = vector distance

ρ_w = density of water

S_0 = reference surface

$S_{in}(s)$ = signal spectrum

$\overline{S}, \overline{S^2}$ = (moments of) shadowing function

s = complex (angular) frequency

$\hat{\sigma}_0, \hat{\sigma}_1, \hat{\sigma}(k)$ = scattering cross sections

S = (subscript) soliton component

$\sigma_g^2, \sigma_c^2, \sigma_G^2$ = mean square wave heights

$\sigma_{gx}^2, \sigma_{Gx}^2$, etc. = mean square wave slopes

T_0 = path delay

γ = surface tension constant

θ_{OT}, θ_{OR} = beam angles

t, t' = time variables

τ_s = duration of pulses

τ = time delay, difference

τ_{ox} = relaxation time

Δt_{dS} = doppler delay

V_T, V_R = regions occupied by transmitter, receiver

W_G, W_g, W_c, W_s = directional surface wave number intensity spectra

$W, W_{g,c}$ = point spectrum of surface waves

\hat{W}_S, \hat{W}_G = normalized wave number spectrum

$x^{(k)}, x_I, x(t), x(l)$ = received waveforms

$\zeta, \zeta_c, \zeta_g, \zeta_G, \zeta_S$ = wave surface elevations

$\zeta_x, \zeta_y, \zeta_{gx}, \zeta_{Gx}$, etc. = derivatives of surface elevations (e.g., slopes)

$Y_{0,\infty}, Y$ = medium response functions

ACOUSTIC SCATTERING CROSS-SECTIONS FOR
TRULY COMPOSITE WIND-WAVE SURFACES:
SCATTERING WITHOUT BUBBLES*

by

David Middleton**

1. Introduction

The study of scattering from random rough surfaces and in particular here, acoustic scattering from moving random, wind-generated wave surfaces, is a venerable subject [1]-[4], [6], [7]-[13], which is of continuing interest and importance. This is true scientifically, because of both analytical and physical problems. The former center around methods of approximation needed for explicit theoretical results; the latter, in choosing physical models appropriate to the wave-surface in question. Scattering from such surfaces is also of critical concern in applications, where reverberation is often a controlling factor, including under-ice, ocean surface, bottom and similar active underwater acoustic environments. Analogous problems and applications arise in the scattering of electromagnetic waves from the atmosphere-ocean interface.

Here we are concerned primarily with determining the intensity of underwater acoustic radiation scattered from random moving wave surfaces. In particular, our first aim is to derive explicit relations for the coherent and incoherent (acoustic) scattering cross-sections for such surfaces, by somewhat different procedures and assumptions from those used in previous work. Both mono- and bi-static cross-sections are included.

Our second goal is to construct a surface wave model which, when applied to our cross-sectional results, has the potential for explaining

*Work supported under contracts with Naval Underwater Systems Center, New London, Conn., 1983, Contract N00140-83-M-NA11 (1983), and in part under Contracts N00140-83-C-KA23, and N00140-84-M-LZ39 (1983, 1984).

**Contractor, Physics and Applied Mathematics, 127 E. 91 St., New York, NY 10128.

the discrepancies between theory and experiment in the important régimes involving backscattering at high frequencies and small grazing angles [1]-[4], without recourse to a bubble mechanism [1]-[4].

Here the dominant scatter contribution is no longer provided by the specular-point (or "facet") scatter [5], but by the small-scale surface components (e.g., Bragg scatter), which now strongly dominates the former, provided, of course, that there is an adequate small-scale component in the first place. This second aim is stimulated by the fact that backscatter data exhibiting the above discrepancies can occur without bubbles [6], [7]. It is also encouraged by the additional observation that in most of the earlier reported data [1], [3], [4] there appears to be no quantitative verification of the presence (or absence) of near-surface bubble layers, sufficient to account for the noted discrepancy. In addition, the empirical scatter data vary with (input signal) frequency in a way not adequately predicted by earlier theoretical models. Furthermore, comparisons of (above-surface) radar and (below-surface) acoustic (backscatter) data [4] are not really convincing, because they were obtained for different oceans (at different times), and with unknown or inadequate "ground-truth": for example, without simultaneous determination of bubble densities below the surface and above-surface water droplet populations, which latter can noticeably affect refraction and the scatter intensity.

In short, we consider it reasonable to state that, at the least, bubble mechanisms are not necessarily the explanation of the aforementioned discrepancies between theory and observation (particularly in the absence of bubbles!). In fact, there is evidence for a wave surface mechanism which can possibly account for the observed scatter levels (at high frequencies and small grazing angles), within the generally available theoretical methods employed earlier, and with the generalizations employed here. The postulated scattering mechanism (suggested by R. H. Mellen [14]) is the ensemble of soliton-ripples [cf. Sec. 2.1 ff.]. These are generated by the near-surface wind impinging on the (irregular) gravity-capillary wave surface, upon which ride the soliton-ripples. (These solitons are found to be the limiting solution of the Korteweg-de Vries equation and are discussed in some detail by Lighthill [16], see also [47].) "Solitons," here "hydraulic jumps," are, among other things, characterized by the fact that they preserve their shape and speed [16]; [47]; Sec. III. Preliminary investigations [17]-[21] suggest that these hydraulic jumps not only embody the non-linear mechanisms

whereby the wave surface itself can be generated by the wind, but may also be sufficiently large to produce the observed scattering levels. What we have here is a truly two-component surface: the soliton ripples ride upon the gravity-capillary wave surface which is their (quasi)-equilibrium result. Unlike the latter, these ripples* are non-dispersive and essentially move down-wind locally, and travel with the same velocity $O(0.4 \text{ m/sec, [15], [47]})$. For acoustic and electromagnetic analyses of two- (or more-) component surfaces, see [2], [4], [21]-[26], [29].

The usual difficulties with the theory arise in the inevitable approximations: the Tangent-Plane or Kirchoff approach used for the (moving) large-scale wave surface components [34], and perturbations [1]-[3], [8]-[11], [29], or other modifications (as used by the author here, cf. Sec. 7 ff.) for the small-scale surface elements. However, the resulting discrepancies can be shown to be quite small $O(1-2.5 \text{ db})$ vis-à-vis the uncorrected Kirchoff method ([4], for example). Diffraction terms are usually neglected in the analysis, but can also be shown to be negligible in most cases with respect to the principal, direct-scatter contributions [cf. Sec. 3.3 ff.]. As we shall see in the text following, the various current theoretical procedures yield analytical results which are formally very similar. However, they can diverge numerically because of different choices of the physical scatter mechanism: capillary waves do not provide sufficient cross-section, for instance, to account for the high-frequency, low-grazing angle discrepancies in (backscatter) cross sections, which have been observed empirically. Their (Bragg-scatter) contributions are $O(10-20 \text{ db})$ too small. Thus, we shall conclude that the observed difficulties stem not from fundamental inadequacies of theory and approximation thereto, but rather from the selection of a suitable physical model. As noted above, our proposed solution is the soliton-ripple mechanism for the principal Bragg scatter contributions, without the intervention of a bubble mechanism.

Our analytical innovations here are: (1) the use of a physically independent scatter surface (the solution-ripples) riding on the gravity-capillary wave surface which in turn is generated by the energy transferred nonlinearly via these ripples [14]-[12], with a non-vanishing "tilt-factor"--produced by the large-scale surface--now determined by: (2) the Kirchoff approximation applied to the development of the Bragg

*Often called "cat's paw" in the initial stages of wind-wave surface excitation, [15].

scatter terms (instead of a perturbational approach [4]). This removes the restrictions of small rms heights and slopes required in the perturbation procedures when applied to the small-scale components, and permits calculation of higher order Bragg-scatter terms if needed [24].

(3) We treat the gravity-capillary wave surface component as the single surface it is, and use the approximate but justifiable technique of splitting this surface into low- and high-frequency components. (The associated "tilt-factor" here, however, vanishes with vanishing grazing angle ($\theta_{OT} \rightarrow \pi/2$.) An insightful justification of this procedure, from a more general theoretical viewpoint, has been given recently by Bahar, Barrick, and Fitzwalter [24], [25], in the analogous but more complex situation of electromagnetic scattering from (simple, i.e., single component) wave surfaces. (4) We develop, and employ, a correlation function and corresponding intensity wave number spectrum for the soliton waves, obtaining estimates which indicate the potentiality of the new mechanisms here.

This Report is organized as follows: Section 2 provides a detailed analytical summary of the mono- and bi-static scattering cross sections, for high and low frequencies (i.e., large and small Rayleigh numbers), and includes comparisons with the results of Tolstoy and Clay [9], McDaniel and Gorman [4], Kur'yanov [21], [1], and Bahar et al. [25]. In Section 3 some preliminary numerical results are obtained, based on the soliton wave model described in Sec. 2.1. Included also are comparisons with backscatter from capillary waves and a short account of the potential contributions from diffraction effects, which are seen to be negligible. Section 4 completes Part I with a concise review of the principal new results and some next steps in the experimental and theoretical analysis of this class of scattering problems. Part II consists of Sections 5-8, where the mathematical details of this study are developed; (see the Table of Contents).

Finally, we emphasize that bubble mechanisms can (and in some instances, do) account for the observed larger (back-) scattering cross sections observed at high frequencies and small grazing angles. However, here we offer a competing mechanism, in the form of soliton ripples [11]-[19]. Preliminary observations and the present analysis

indicate that these ripples can potentially account for the observed data when bubbles are absent [6], [7]. Further experimental results are needed to establish this possibility conclusively, but already the work of Roderick ([6], and Table 3.2 ff.) indicates encouraging potential support for this mechanism.

Part I. Acoustic Scattering Cross Sections

2. Scattering Cross Sections for Composite Wave Surfaces

As noted above (and subsequently in Sections 7, 8) the principal aim of this initial study is to obtain analytic expressions for the acoustic scattering cross sections of a truly two-component or composite moving wave surface. This includes an initial numerical demonstration that values comparable to those observed experimentally can be obtained with the introduction of a suitable physical model, without having to postulate a bubble-scattering mechanism [3], [4]. This is particularly important in situations where no (or negligible) bubbles are found to be present [6].

2.1 The New Wave-Surface Model: Surface Elevation

We postulate the following potential mechanism for the small-scale scattering component of a typical wind-wave surface: ensembles of solitons, or hydraulic jumps, produced, as shock waves, by the impact of the local wind on the gravity-capillary wave structure. These solutions, which mathematically are the limiting solution of the Korteweg-de Vries equation for cnoidal waves ([16], pp. 465-467), travel in all directions on the rough, large-scale surface, with constant speed. They travel on a thin viscous layer and probably represent the principal (and nonlinear) mechanism whereby wind energy is transferred to the overall wave surface. On initially still surfaces they appear as the familiar "cats-paw" effect and have rather many ripples in a typical "wave" packet. As the surface builds a wave structure, with the transfer of energy from these soliton trains progressively into the small (capillary and then gravity) wave numbers, the wave surface becomes quite irregular and the soliton packets lose their directionality and structure, becoming essentially a collection of individual solitons traveling over the new rough gravity-

capillary surface. (See, for example the illustration in [26] opposite the inside book title page.) Here we are concerned with the amplitudes and durations of these solitons (as discussed in Sec. 3.1 ff.) from the present viewpoint of acoustical scattering, rather than with their oceanographic implications for wave generation. (See Mellen [14], [15]; also [17], [20], and in particular, Lighthill [16]; also, generally, [47].)

Unlike the soliton-ripple component, which is nondispersive, rides upon, and is essentially independent of the underlying gravity-capillary wave surface, this latter (or "G"-surface) is a single, directional surface, with a wave structure obeying the dispersion law $\omega_s = [qK_s + (\mathfrak{J}/\rho_w)K_s^3]^{1/2}$, with $K_s = 2\pi/\lambda_s$, where $f_s (= \omega_s/2\pi)$ is the frequency of a typical Fourier component of the (moving) G-wave surface [26]-[28] and \mathfrak{J} is the surface tension (force \times distance) coefficient of water, with ρ_w the water density. It is convenient to divide this wave surface spectrally into a large-scale or "gravity-wave" component (g) and an essentially independent small-scale "capillary" component (c), at some representative wave number, k_0 . This, of course, is a mathematical device, since there is no abrupt transition between the gravity wave number domain and the capillary domain. This surface is really a single rough surface, where the "capillary" component consequently does not ride upon the gravity component.

With the above in mind we can write for the wave surface elevation

$$\underline{\zeta}(\underline{r}, t) = \hat{\underline{i}}_z [\zeta_g(\underline{r}, t) + \zeta_c(\underline{r}, t)] + \hat{\underline{n}}_G(\underline{r}, t) \zeta_S(\underline{r}, t), \quad \underline{r} = \hat{\underline{i}}_x x + \hat{\underline{i}}_y y \quad (2.1)$$

where $G (= g+c)$ denotes the single capillary-gravity wave surface and S indicates the elevation of the soliton-ripples, which ride on $\hat{\underline{i}}_z \zeta_G = \hat{\underline{i}}_z (\zeta_g + \zeta_c)$, cf. Fig. 2.1. Here $\hat{\underline{n}}_G$ is the normal [at (\underline{r}, t)] to the G-surface, viz.,

$$\hat{\underline{n}}_G = \{(\hat{\underline{i}}_x \zeta_x + \hat{\underline{i}}_y \zeta_y - \hat{\underline{i}}_z) / (1 + \zeta_x^2 + \zeta_y^2)^{1/2}\}_{G=g+c} \doteq \hat{\underline{n}}_g, \quad (\zeta_x = \frac{\partial \zeta}{\partial x}, \text{ etc.}), \quad (2.2a)$$

with generally

$$n_z = (1 + \zeta_x^2 + \zeta_y^2)^{-1/2}, \quad \therefore \hat{\underline{n}} \equiv (\hat{\underline{i}}_x \zeta_x + \hat{\underline{i}}_y \zeta_y - \hat{\underline{i}}_z) n_z, \quad (2.2b)$$

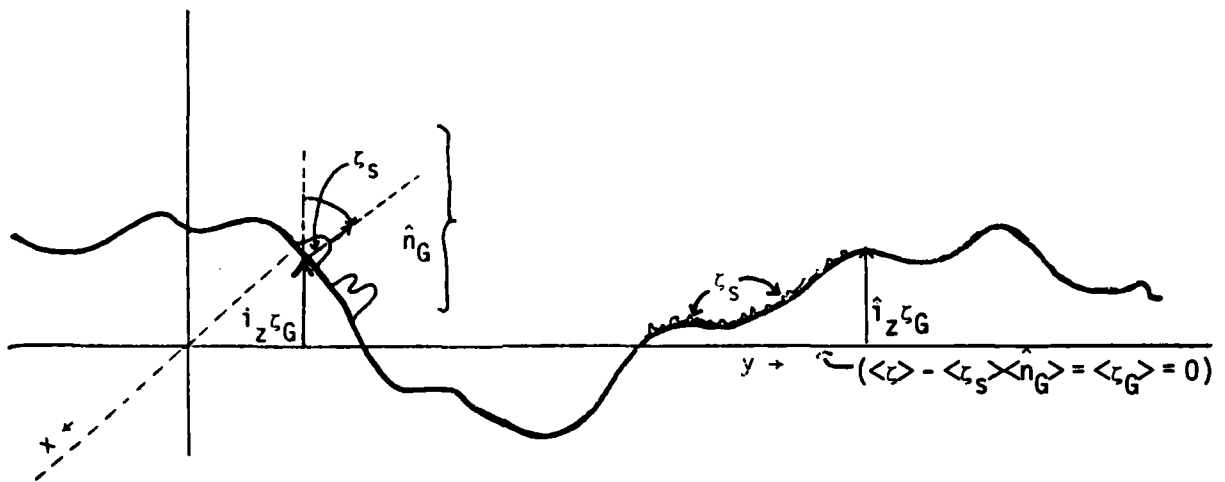


Fig. 2.1. Cross section of a moving wind-wave surface, showing soliton ripples (greatly exaggerated) riding on the gravity-capillary wave surface ζ_G .

since the rms capillary elevation and slopes of the gravity components are small, cf. Eqs. (7.18)-(7.18a). Here ζ_g and ζ_c are, respectively, the elevation of the "gravity" and "capillary" components, in our artificial division of the single wave surface ζ_g . The equilibrium surface* is $\langle \zeta \rangle = 0$.

The spectral division of the G-surface is formally indicated by the (surface) wave-number-time (intensity) spectrum $W(k|\tau)$, here with $\tau = 0$.

$$\left. \begin{aligned} w_G(\underline{k}|0) &= w_g(\underline{k}|0), & 0 < |\underline{k}| < |\underline{k}_D|, \\ &= w_c(\underline{k}|0), & |\underline{k}_D| < |\underline{k}|. \end{aligned} \right\} \quad (2.3)$$

The two components of W_G have a common directional character, determined by

$$W_G(\underline{k}|0) = \frac{1}{2} \int_{-\infty}^{\infty} W_G(f_s) \langle \delta[\underline{k}/2\pi - \underline{k}_s(\hat{\alpha})/2\pi] \rangle_{\hat{\alpha}} df_s, \quad f_s \geq 0, \quad (2.4a)$$

*Since the solitons, or hydraulic jumps, are one-sided [16], we see that $\langle \zeta \rangle = \langle \hat{\eta}_G \times \zeta_S \rangle$, $\langle \zeta_S \rangle = 0$: the equilibrium surface is $\langle \zeta_G \rangle = 0$. For practical purposes, $\langle \zeta_S \rangle \ll \langle \zeta_G^2 \rangle^{1/2}$, so that we may regard $\langle \zeta \rangle \approx 0$ here, as we shall do henceforth.

$$\begin{aligned}
&= \int_{0-}^{f_{SD}} W_g(f_s) \langle \delta(\underline{\nu} - \underline{K}_S(\hat{\alpha})/2\pi) \rangle_{\hat{\alpha}} df_s \\
&\quad + \int_{f_{SD}}^{\infty} W_c(f_s) \langle \delta(\underline{\nu} - \underline{K}_S(\hat{\alpha})/2\pi) \rangle_{\hat{\alpha}} df_s,
\end{aligned} \tag{2.4b}$$

where $\underline{\nu} = \underline{k}/2\pi$ and $\underline{K}_S(\hat{\alpha}) = K_S(f_s)\hat{\underline{i}}_W$, in which $\hat{\underline{i}}_W$ is the unit vector for wave components of frequency f_s , e.g., $\hat{\underline{i}}_W = \hat{\underline{i}}_x \cos \hat{\alpha} + \hat{\underline{i}}_y \sin \hat{\alpha}$, and $\hat{\alpha}$ obeys a probability density $w_1(\hat{\alpha}) \neq 0$, $\hat{\alpha}_0 - \pi/2 < \hat{\alpha} < \hat{\alpha}_0 + \pi/2 = 0$ elsewhere; (there are no g,c-waves against the mean wind in this model). In fact, from D, Sec. 7.3, we have explicitly

$$\langle \delta(\underline{\nu} - \underline{K}_S(\hat{\alpha})) \rangle_{\hat{\alpha}} = \frac{3}{2} \frac{\sqrt{2\pi\nu}}{(\rho_w/\mathfrak{J})^{1/2}} \delta(f_s - \frac{1}{2\pi}[gK_S + (\frac{\tau}{\rho_w})K_S^3]^{1/2}) w_1(\hat{\alpha} - \hat{\alpha}_0), \tag{2.5}$$

which when applied to (2.4b) gives the desired wave number intensity spectrum of the G-surface, in terms of its two (artificially) designated components (g,c). The quantity $W_G(f_s)$ is the point, or directionless intensity spectrum of the G (=g+c) surface elevation $\zeta_G = \zeta_g + \zeta_c$. One choice for W_G is the Pearson-Moskowitz spectrum [8]. (For a wave number spectrum of the soliton ripples, see (3.6b) and Section 3.1B ff.)

2.2 Scattering Cross-Sections: Definitions

There is a number of variations on the concept and definitions of scattering cross section. It is therefore important to define the term explicitly, so that the different definitions can be calibrated with one another, as we shall need to do in order to effect comparisons with both the analytic results of others and the corresponding measurements (cf. Secs. 2.A,B and Sec. 3 ff.).

We begin with:

A. Incoherent Scattering Cross Sections, $\hat{\sigma}_{inc}^{(0)}$:

Here we define

$$\hat{\sigma}_{inc}^{(0)} \equiv \frac{I_{incoh}^{(k=0)} \text{ (scattering at receiver R)} \cdot R_{OR}^2}{I_{incident} \text{ (at surface)} A_{REF}} [(\text{path loss}) \times (g_T g_R)^2]^{-1}, \quad (2.6)$$

where I_{incoh} , $I_{incident}$ are, respectively, the intensities of the scattered and incident fields at the points indicated. The basic concept of the scattering cross section (for surfaces) is to eliminate the effects of source level and propagation, i.e., the effects of the medium--which are handled separately--when computing energy loss, and to focus on the effects of the random scattering surface itself. For this reason path loss (absorption), beam pattern gains (g_T , g_R), signal levels, and source and receiver distances are removed, where possible, as (2.6) indicates. To keep $\hat{\sigma}_{inc}^{(0)}$ dimensionless, a reference "illumination" area, A_{REF} , is employed, whose specific form is suggested by the composite beam pattern projection on the reference or equilibrium surface $\langle z \rangle \doteq 0$: S_0 . Figure 2.2 shows the relevant geometry.

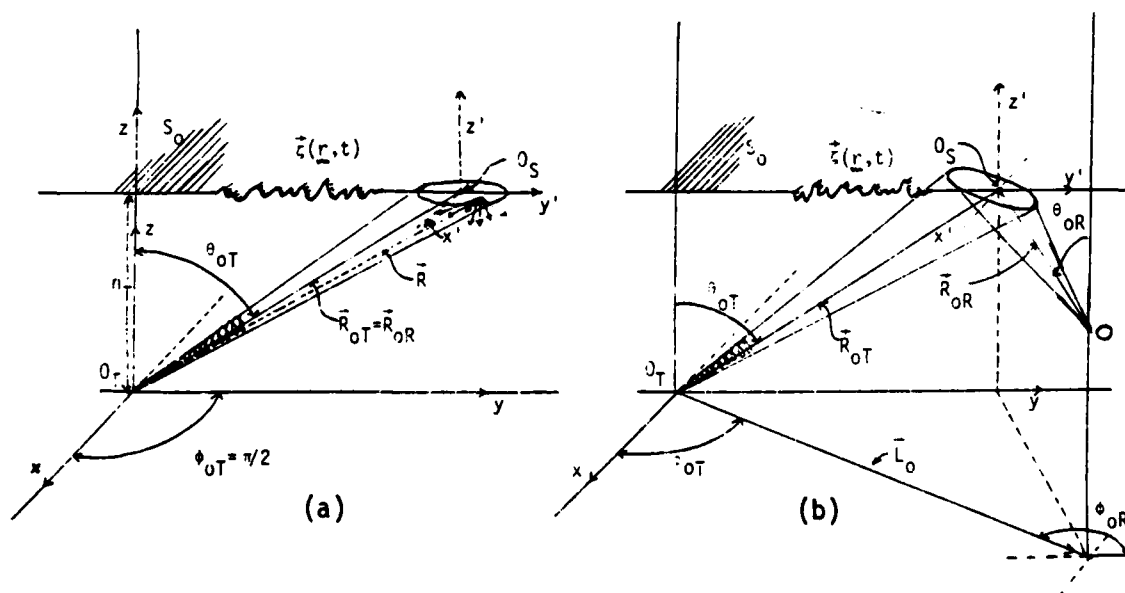


Fig. 2.2. (a) Backscatter Geometry (far-field): Monostatic scattering ($R=T$), vide Fig. 5.1; (b) Bistatic Scattering ($R \neq T$); "forward" or oblique scattering geometry; vide Fig. 5.1.

The various factors in Eq. (2.6) are given by

$$(2.7a) \quad I_{\text{incoh}}^{(k=0)} (\text{scat. at receiver}) = M_{X-\langle X \rangle}^{(0)}(0) = \text{intensity of the (incoherent) scattered field at the receiver (R), cf. Sec. 7.2 et seq.; Sec. 8 ff.};$$

$$(2.7b) \quad I_{\text{incident}}(\text{at surface}) = K_0(0)_{\text{in}} / (4\pi R_{OT})^2 = \text{intensity of the incident field at } O_S, \text{ on the equilibrium scattering surface } S_0;$$

$$(2.7c) \quad g_T, g_R = \text{the aperture "gain" of the transmitting and receiving systems, cf. (6.3), (6.7);}$$

$$(2.7d) \quad A_{\text{REF}} = \text{a reference area on the equilibrium surface } S_0, \text{ cf. Fig. 2.2, projected by the composite T and R beam patterns. (See C ff.);}$$

$$(2.7e) \quad \left\{ \begin{array}{l} \text{"path loss"} \\ \text{(absorption)} \end{array} \right. = e^{-2a\omega_0^2 c_0 T_0}; \quad c_0 T_0 = R_{OT} + R_{OR}; \text{ cf. Sec. 5.3, Eq. (5.18); } \omega_0 (=2\pi f_0) \text{ is the (angular) frequency of the emitted signal; } a \text{ is an absorption coefficient; } c_0 = \text{(mean) wave front speed of sound in the water medium;}$$

$$(2.7f) \quad R_{OR} = \text{distance of the receiver (origin) from } O_S, \text{ Fig 2.2;}$$

$$(2.7g) \quad R_{OT} = \text{distance of the transmitter (origin) from } O_S, \text{ Fig. 2.2;}$$

$$(2.7h) \quad \underline{z}(\underline{r}, t) = \text{(vector) wave surface elevation, cf. (2.1).}$$

The definition (2.6) for the incoherent scattering cross section, and those similar to it ([3]-[5], [8], [9], [23]-[25], [29], for example) are formally independent of range (R_{OT}, R_{OR}). This is not an inherent property of the definition, however; it is a direct consequence of the far-field assumption, whereby the effective coherent scattering area is sufficiently small vis-à-vis source and receiver distances (R_{OT}, R_{OR}) and dimensions, cf. Sec. 5.5 and Eq. (5.31). It also depends on the correlation distances (l_x, l_y) of the (components of the) random wave surface. Thus, $\hat{\sigma}_{inc}^{(0)}$ is implicitly a function of geometry, where care must be taken in its use to ensure that the conditions governing the derivation of $I_{incoh}^{(k=0)} (= M_{X-\langle X \rangle}^{(0)}(0))$, (2.7a), are obeyed*.

A complete definition of the incoherent scattering cross section includes the effects of diffraction

$$\hat{\sigma}_{incoh} \equiv \hat{\sigma}_{incoh}^{(0)} + \sum_{k=1}^{\infty} \hat{\sigma}_{incoh}^{(k)}, \quad (2.8)$$

where the $\hat{\sigma}_{incoh}^{(k)}$, $k \geq 1$, are formally given by (2.6), with $I_{incoh}^{(0)}$ replaced by the scattering intensities $I_{incoh}^{(k \geq 1)} = M_{X-\langle X \rangle}^{(k)}(0)$, cf. Secs. 7.2C, 8.5 ff.

Preliminary estimates (Sec. 3.3 ff.) of the magnitude of the leading diffraction component, $\hat{\sigma}_{incoh}^{(1)}$ ($\gg \hat{\sigma}_{incoh}^{(k \geq 2)}$), indicate that it is ordinarily considerably smaller than the components of the "classical" term, $\hat{\sigma}_{incoh}^{(0)}$, so that in this study we shall be able to neglect the diffraction contributions.

*The factors 4π in (2.7a), (2.7b), and in (2.9), (2.10b) ff., etc., arise because of our definition of the green's function, (5.8), and source function (5.3a) in the equations of propagation (here a Helmholtz medium). Thus, our acoustic field is $\alpha_M = \alpha/4\pi$, where α is derived from a green's function source of the form $-4\pi\delta(\underline{R}-\underline{R}')\delta(t-t')$. However, because of the particular form of the definition of $\hat{\sigma}^{(0)}$ used here and generally, the scaling of the field is immaterial, as is required in any useful definition.

B. Coherent Scattering Cross Sections, $\hat{\sigma}_{coh}^{(0)}$:

The coherent scattering cross section, $\hat{\sigma}_{coh}^{(0)}$, is formally the same as $\hat{\sigma}_{incoh}^{(0)}$, (2.6), except that now the incident intensity (2.7b) becomes

$$I_{incident}(\text{at the receiver})_{coh} = K_0(0)_{in} / \{4\pi(R_{OT} + R_{OR})\}^2 \quad (2.9)$$

which is the "mirror reflection" term. Thus, $I_{incid-coh} = (1/4)I_{incid-incoh}$, cf. (2.7b). In addition, $I_{incoh}^{(k=0)}$ is replaced by the coherent component $M_{<X>}^{(0)}(0)$, cf. Sec. 7.2B, Eq. (8.7). Since only the "classical" or ($k=0$) component of the scattered field, contains a potentially coherent contribution (excluding any direct field which may be received under certain mutual geometries), the complete coherent scatter cross section is now specifically

$$\hat{\sigma}_{coh}^{(0)} \equiv \frac{I_{coh}^{(0)}(\text{scattering at R}) R_{OR}^2}{I_{incid}(\text{at the receiver R}) A_{REF}} \{ \text{path loss} \times (g_T g_R)^2 \}^{-1}, \quad (2.10a)$$

or

$$\hat{\sigma}_{coh}^{(0)} = \frac{R_{OR}^2 \{4\pi(R_{OR} + R_{OT})\}^2 M_{<X>}^{(0)}(0)}{(g_T g_R)^2 A_{REF} K_0(0)_{in} \cdot (\text{path loss})}. \quad (2.10b)$$

C. The Reference Area, A_{REF} :

The reference area, A_{REF} , appearing in the above definitions of the scattering cross sections, (2.6), (2.10), while arbitrary, is dependent on the beam pattern projections on S_0 . From Section 6.5 IV, (6.56), our choice of reference area is specifically

$$A_{REF} = A_1/2, \quad A_1 = 2\pi/\sqrt{AB(\theta_{OT})}, \quad (2.11)$$

where A_1 is the projected area (on S_0) of the combined gaussian-omni-directional beam pattern used specifically in this study.

2.3 "High-Frequency" Scattering Cross Sections:

By "high-frequency" we mean here large Rayleigh numbers, e.g., $R_g \equiv (k_0 b_0 \sigma_g)^2 \gg 1$, specifically for the large-scale gravity component of the wave surface. Thus, we have for the elements of R_g :

$$\left. \begin{aligned} k_0 &\equiv 2\pi/\lambda_0 = 2\pi f_0/c_0 = \text{wave number (rad}\cdot\text{meter}^{-1}) \text{ of the (central) frequency of the applied (narrow-band) signal;} \\ b_0 &\equiv \cos \theta_{0T} + \cos \theta_{0R}; \text{ cf. Fig. (5.1) and Sec. 5.4 ff.;} \\ \sigma_G^2 &\equiv \langle \zeta_G^2 \rangle, \text{ the mean-square (gravity-capillary) wave surface height, about } \langle \zeta_G \rangle = 0. \end{aligned} \right\} (2.12)$$

Accordingly, from the results of Sections 8.1, 8.3, 8.4 for the scatter intensities $M_{X-\langle X \rangle}^{(0)}(0)$, $M_{\langle X \rangle}^{(0)}(0)$ applied directly to the scatter cross sections as defined by (2.6), (2.10b), with the reference area given here by (2.11), we get the following "high-frequency" forms:

$$\begin{aligned} \sigma_{\text{incoh}}^{(0)} \Big|_{R_g \gg 1} &= \frac{\overline{R_0^2} \overline{s_0^2}}{R_0^2 s_0^2} \left[\left(\frac{\alpha_{0x}^2 + \alpha_{0y}^2 + \alpha_{0z}^2}{\alpha_{0z}^2/2} \right)^2 e^{-\frac{1}{2b_0^2} \left[\frac{(2\alpha_{0x})^2}{\sigma_{Gx}^2} + \frac{(2\alpha_{0y})^2}{\sigma_{Gy}^2} \right]} \right. \\ &\quad \left. + \frac{k_0^4}{16\pi^2} N_{Gc}^{(0)} (2\alpha_0|_{x,y})_{\text{inc}} W_c(2\alpha_0 k_0|_{x,y}|0) \right]_G \\ &\quad \left. + \frac{k_0^4}{16\pi^2} N_{GS}^{(0)} (2\alpha_0|_{x,y})_{\text{inc}} \sigma_{S\hat{W}S} (2\alpha_0 k_0|_{x,y}|0) \right] \end{aligned} \quad (2.13)$$

where we have used (8.6), (8.7), extended to (8.29), with $\alpha_0|_{x,y} = (\alpha_{0x}, \alpha_{0y})$, a two-dimensional vector in the reference (x,y-) or S_0 -plane. The terms in $\{ \}_G$ represents the results of the "physical-optics" cum "perturbational" approach, cf. Sec. 7.3 for the single gravity-capillary wave surface, while the remaining term embodies the contribution of the soliton-ripples. [See (2.17)-(2.20) below for explicit descriptions of the various elements in (2.13).]

Here, $N_{gc}^{(0)}$ and $N_{gs}^{(0)}$ are respectively the "tilt factors" for the capillary and soliton-ripple components of the wave surface. Specifically, from (7.33) we have here ($\phi_{0T} = \pi/2$)

$$N_{gs}^{(0)}(\alpha_0)_{\text{incoh}} = \left\langle \frac{(2\alpha_{0x}\zeta_x + 2\alpha_{0y}\zeta_y - 2\alpha_{0z})^4}{1 + \zeta_x^2 + \zeta_y^2} \right\rangle_G \quad (2.14a)$$

$$\doteq 16\{\alpha_{0y}^4 \langle \zeta_{Gy}^4 \rangle + 6\alpha_{0y}^2 \alpha_{0z}^2 \langle \zeta_{Gy}^2 \rangle + \alpha_{0z}^4\},$$

since $n_z^2 = (1 + \zeta_{Gx}^2 + \zeta_{Gy}^2)^{-1} = 1 - O(10^{-2}) \doteq 1$ for the accuracy needed here. Similarly, we get

$$N_{gc}^{(0)}(\alpha_0)_{\text{incoh}} = \langle (2\alpha_{0x}\zeta_x + 2\alpha_{0y}\zeta_y - 2\alpha_{0z})^2 \rangle_G (2\alpha_{0z})^2 \quad (2.14b)$$

$$\doteq 16\alpha_{0z}^2 (\alpha_{0y}^2 \sigma_{Gy}^2 + \alpha_{0z}^2), \quad \sigma_{Gy}^2 = \langle \zeta_{Gy}^2 \rangle,$$

cf. (8.28a). For the gaussian gravity wave elevations assumed here, we have $\langle \zeta_{gy}^4 \rangle = 3\sigma_{gy}^4$. We note that the tilt-factor for the capillary component, (2.14b), vanishes as $\theta_{0T} \rightarrow \pi/2$ (zero grazing angle), because ζ_0 is really part of a single surface: the capillary waves do not "ride" on the gravity components, cf. (2.1) above. On the other hand, the "tilt-factor" $N_{gs}^{(0)}$, (2.14a), for the soliton-ripples is nonvanishing (as $\theta_{0T} \rightarrow \pi/2$), as expected, since these ripples, or hydraulic jumps, do ride upon the gravity-capillary surface, ζ_G . These "capillary" and ripple components show up as Bragg (or resonant) scatter terms (\sim wave number

spectra at $\underline{k} = 2k_0 \alpha_0 |_{x,y}$ ([1], [2], [21]-[23], etc.). These are first-order scatter components, since $\sigma_c^2, \sigma_s^2 \ll 1$, with small-scale spatial correlations [24]. The specular-point term in (2.13) is independent of frequency, generally, in this "physical-optics" limit.

Also, we have for all $R_g \geq 0$ in the coherent cases (8.7), (8.21),

$$\hat{\sigma}_{coh}^{(0)} = \frac{A_1 \overline{R_0^2} \overline{S^2} k_0^2}{16\pi^2} \left\{ (2\alpha_{0z})^2 e^{-b_0^2 k_0^2 \sigma_G^2} \cdot e^{-3k_0^2 [\alpha_{0x}^2/A + \alpha_{0y}^2/B]} \right\} \rightarrow 0: "hi-freq", \quad (2.15)$$

where $\sigma_g^2 \gg \sigma_c^2, \sigma_s^2$, since $R_g \gg 1$ here: very rough surfaces destroy coherence, as expected. [In addition, since $A, B \ll 1$, cf. (6.32), the second exponential also ensures the vanishing of $\hat{\sigma}_{coh}$, unless the Snell angle ($\alpha_{0x} = \alpha_{0y} = 0$) is chosen.] Note that this coherent-scatter cross section depends on the area illuminated (via A_1), as distinct from the incoherent cases, (2.13), which are always area-independent, subject, of course, to the conditions (2.20) ff.

In compact fashion, we can rewrite (2.13) as

$$\hat{\sigma}_{incoh}^{(0)}|_{R_g \gg 1} \approx [\hat{\sigma}_{g-inc}^{(0)} + \hat{\sigma}_{c-inc}^{(0)}] + \hat{\sigma}_{s-inc}^{(0)} = \hat{\sigma}_{G-inc}^{(0)} + \hat{\sigma}_{S-inc}^{(0)}, \quad (2.16)$$

where the first two terms of (2.13) correspond to $\hat{\sigma}_{G-inc}^{(0)}$, and the last, to that portion of the scattering cross section attributable to the soliton-ripple component. Our results (2.13)-(2.16) hold for arbitrary directions of illumination and observation.

The various elements of (2.10), (2.13) are specifically:

$$(2.17) \left\{ \begin{array}{ll} \overline{R_0^2}, \overline{R_0} & = \text{mean-square, mean, reflection coefficients (=1, for} \\ & \text{water/air interfaces);} \\ \overline{S^2}, \overline{S} & = \text{mean-square, mean, shadowing function, see Sec. 7.4C.} \end{array} \right.$$

$$\begin{aligned}
 (2.17) \quad & \sigma_{Gx}^2, \sigma_{Gy}^2 = \langle \zeta_{Gx}^2 \rangle, \langle \zeta_{Gy}^2 \rangle: (\zeta_{Gx} = \frac{\partial \zeta_G}{\partial x}, \text{ etc.}): \text{mean-square slopes of} \\
 & \quad \text{the gravity-capillary wave component, cf. Sec. 7.4B;} \\
 & \sigma_c^2 = \langle \zeta_c^2 \rangle: \text{mean-square height (about } \langle \zeta_c \rangle = 0 \text{) of the} \\
 & \quad \text{"capillary" wave surface;} \\
 & \sigma_S^2 = \langle \zeta_S^2 \rangle: \text{mean-square height of the soliton humps;} \\
 & W_c = \text{surface wave number intensity spectrum of } \zeta_c \text{ (cf. (2.3)) with} \\
 & \quad \sigma_{Gc}^2(\underline{\Delta r}, 0) = \int_{-\infty}^{\infty} W_c(\underline{k}|0) \cos(\underline{k} \cdot \underline{\Delta r}) \frac{d\underline{k}}{2\pi^2}, \text{ cf. (8.25);} \\
 & W_S = \text{wave number spectrum of the soliton-ripple} \\
 & \quad \sigma_S^2 \hat{W}_S = \int_{-\infty}^{\infty} K_S(\underline{\Delta r}|0) e^{i\underline{k} \cdot \underline{\Delta r}} d(\underline{\Delta r}) \\
 & \quad \text{and } \hat{W}_S = W_S / \sigma_S^2 = \text{normalized spectrum;} \\
 & A_1 = \text{Eq. (2.11);} \\
 & b_0 = \cos \theta_{OT} + \cos \theta_{OR}, \text{ (2.12).}
 \end{aligned}$$

The directional vector $2\underline{\alpha}_0$ is (cf. Sec. 5.5, Fig. 5.1),

$$\begin{aligned}
 2\underline{\alpha}_0 = \hat{\underline{i}}_{OT} - \hat{\underline{i}}_{OR} &= \hat{\underline{i}}_x \left(1 + \frac{R_{OT}}{R_{OR}}\right) \cos \phi_{OT} \sin \theta_{OT} \\
 &+ \hat{\underline{i}}_y \left\{ \left(1 + \frac{R_{OT}}{R_{OR}}\right) \sin \phi_{OT} \sin \theta_{OT} - L_0/R_{OR} \right\} + \hat{\underline{i}}_z b_0
 \end{aligned} \quad (2.18)$$

for arbitrary angles of illumination and observation.

Important special cases of (2.18) are:

(i). Backscatter (R^{BT}): ($L_0 = 0$; $\theta_{OR} = \theta_{OT}$; $\hat{\underline{i}}_{OR} = -\hat{\underline{i}}_{OT}$; $R_{OR} = R_{OT}$;
 $h_R = h_T$; $\phi_{OR} = \phi_{OT} + \pi/2$; cf. Fig. 2.2).

$$\therefore 2\underline{\alpha}_0 = 2(\hat{\underline{i}}_x \cos \phi_{OT} \sin \theta_{OT} + \hat{\underline{i}}_y \sin \phi_{OT} \sin \theta_{OT} + \hat{\underline{i}}_z \cos \theta_{OT}); \quad (2.18a)$$

$$(\alpha_{ox}^2 + \alpha_{oy}^2 + \alpha_{oz}^2)/\alpha_{oz}^2 = 2/\cos \theta_{OT}. \quad (2.18b)$$

(ii). Bistatic at the Snell Angle ($R \neq T$): $L_0 \neq 0$

$$\left. \begin{aligned} (\hat{i}_{OR})_x &= (\hat{i}_{OT})_x & \text{when } \phi_{OT} = \pi/2 = (\phi_{OR} - \pi/2); \\ (\hat{i}_{OR})_y &= (\hat{i}_{OT})_y & \text{when } L_0 = (R_{OT} + R_{OR}) \sin \theta_{OT}; \\ (\hat{i}_{OR})_z &= -(\hat{i}_{OT})_z & \text{when } \theta_{OR} = \theta_{OT}. \end{aligned} \right\} \text{Snell plane} \quad (2.19a)$$

$$\therefore 2\alpha_0 = 2\hat{i}_z \cos \theta_{OT}, \text{ or } \alpha_0 = \hat{i}_z \cos \theta_{OT}; \quad (2.19b)$$

$$(\alpha_{ox}^2 + \alpha_{oy}^2 + \alpha_{oz}^2)/\alpha_{oz}/2 = 2 \cos \theta_{OT}. \quad (2.19c)$$

Otherwise, (2.18) is the general relation.

The principal assumptions and approximations pertaining to our general high-frequency results (2.13), (2.15), are:

- (2.20) {
- (1). Far-field (Fraunhofer) geometries, cf. Sec. 5.5;
 - (2). Narrow-band signals (so that we may treat time parametrically in the moving wave surface vis-à-vis the acoustic signal); cf. remarks after Eq. (5.21b);
 - (3). Narrow beams (cf. Sec. 6.6); at least one narrow-beam;
 - (4). Neglects diffraction terms: $k=1$: "Diffuse" scatter; $k \geq 2$: multiple scatter (cf. Sec. 3.3; also Sec. 8.5);
 - (5). Small Rayleigh numbers for the small-scale surfaces, $\zeta_{c,S}$:
 $R_{c,S} \equiv (k_0 b_0 \sigma_{c,S})^2 \ll 1$;
 - (6). The capillary and soliton surfaces (ζ_c, ζ_s) are "small-scale," e.g., $\lambda_{c,S} \ll \lambda_g$: the correlation distance of the gravity-wave component is much larger than that of the capillary and soliton waves;
 - (7). The small-scale surfaces are statistically independent of the gravity wave surface component (vide remarks in Sec. 7.3A, Eq. (7.19) et seq.);
 - (8). Both components of the wave surface are essentially homogeneous and stationary, at least over the "illuminated" area and for times long compared to the duration of the incident signal.

[For a more detailed discussion, see Secs. 5.5, 6.6, and Sec. 7.]

A. Backscatter (R@T)

First, by (2.15) the coherent backscatter cross section $\sigma_{\text{coh}}^{(0)}$ vanishes for these high frequencies. On the other hand, the incoherent backscatter cross section, $\sigma_{\text{inc}}^{(0)}$, is clearly nonvanishing. It is obtained at once from (2.18) in (2.13). On setting $\phi_{\text{OT}} = \pi/2$, cf. Fig. 2.2a, we have

$$\sigma_{\text{inc}}^{(0)} \Big|_{\substack{\text{R@T} \\ R_g \gg 1}} = \overline{R_0^2} \overline{S^2} \left[\left\{ \frac{e^{-(\tan^2 \theta_{\text{OT}})/2\sigma_{\text{Gy}}^2}}{8\pi \cos^4 \theta_{\text{OT}} \sigma_{\text{Gx}} \sigma_{\text{Gy}}} \right. \right. \\ \left. \left. + \frac{k_0^4}{16\pi^2} N_{\text{GC}}^{(0)}(\theta_{\text{OT}})_{\text{inc}} W_{\text{C}}(0, 2k_0 \sin \theta_{\text{OT}} | 0) \right\}_{\text{G}} \right. \\ \left. + k_0^4 N_{\text{GS}}^{(0)}(\theta_{\text{OT}})_{\text{inc}} \sigma_{\text{S}}^2 \hat{W}_{\text{S}}(0, 2k_0 \sin \theta_{\text{OT}} | 0) \right] \quad (2.21)$$

$$= \{ \sigma_{\text{g-inc}}^{(0)} + \sigma_{\text{c-inc}}^{(0)} \}_{\text{G}} + \sigma_{\text{S-inc}}^{(0)} \quad (2.21a)$$

The first term of (2.21), $\sigma_{\text{g-inc}}^{(0)}$, is independent of frequency in this high-frequency approximation, which is recognized as the "specular-point," facet-, or geometrical acoustics solution form of the full-wave approach of Bahar [23], [24], [30], [31] and Barrick et al. [5], [22], [24], [25]. The second term, $\sigma_{\text{c-inc}}^{(0)}$, embodies the (first-order) Bragg scatter associated with the small-scale small Rayleigh number capillary wave surface, while the third term, $\sigma_{\text{S-inc}}^{(0)}$, gives the Bragg scatter due to the soliton ripples. Whereas the specular-point contribution $\sigma_{\text{g-inc}}^{(0)}$ is the dominant part of the cross section at moderate angles ($\theta_{\text{OT}} < 60^\circ$), it rapidly vanishes for small grazing angles ($\theta_{\text{OT}} \rightarrow \pi/2$), cf. Fig. 3a of [5], leaving $\sigma_{\text{c-inc}}^{(0)}$ and $\sigma_{\text{S-inc}}^{(0)}$, of which only the latter remains nonvanishing* as $\theta_{\text{OT}} \rightarrow \pi/2$, cf. (2.14). In fact, as we shall presently see (Sec. 3), for ($\theta_{\text{OT}} \geq 70^\circ$), where $\sigma_{\text{g-inc}}^{(0)} \doteq 0$, $\sigma_{\text{S-inc}}^{(0)}$ dominates $\sigma_{\text{c-inc}}^{(0)}$ by 0(10 or more db). It is this latter component, $\sigma_{\text{S-inc}}^{(0)}$, with which

*Apart from the shadowing function $\overline{S^2}$, which $\rightarrow 0$, of course, as $\theta_{\text{OT}} \rightarrow \pi/2$.

we are chiefly concerned here. Some preliminary numerical evaluations and comparisons are given in Secs. 3.1, 3.2, following. In particular, from (7.33) we easily find for the isotropic cases that ($\phi_{OT} = \pi/2$)

$$N_{GC-back}^{(0)} \triangleq 16 \cos^2 \theta_{OT} (\sigma_{g(y=x)}^2 \sin^2 \theta_{OT} + \cos^2 \theta_{OT}) \quad (2.22a)$$

and

$$N_{GS-back}^{(0)} \triangleq 16 \{ 3 \sigma_{g(y=x)}^4 \sin^4 \theta_{OT} + 6 \sigma_{g(x=y)}^2 \cos^2 \theta_{OT} \sin^2 \theta_{OT} + \cos^4 \theta_{OT} \}. \quad (2.22b)$$

(For the more general, nonisotropic cases we must use (2.14a,b).)

B. Bistatic Scatter in the Snell Direction ($R \neq T$)

Here we use (2.19) in (2.13) [with the help of (8.14) alternatively in (2.6)], since $\alpha_{ox} = \alpha_{oy} = 0$, $\alpha_{oz} = \cos \theta_{OT}$, to get directly

$$\begin{aligned} \sigma_{incoh}^{(0)} \Big|_{\substack{R \neq T: \text{Snell} \\ R_g \gg 1}} &= \overline{R_0^2} \overline{S^2} \left[\left\{ \frac{1}{8\pi\sigma_{Gx}\sigma_{Gy} \cos^4 \theta_{OT}} + \frac{k_0^4}{\pi^2} \cos^4 \theta_{OT} W_C(0,0|0) \right\}_G \right. \\ &\quad \left. + \frac{k_0^4}{\pi^2} \cos^4 \theta_{OT} \sigma_S^2 \hat{W}_S(0,0|0) \right]. \end{aligned} \quad (2.23)$$

At small grazing angles ($\theta_{OT} \sim \pi/2$) the facet term vanishes because of shadowing and the Bragg scatter terms likewise go to zero, not only because of shadowing but also because their "tilt-factors" vanish. There is no coherent component, of course, since $R_g \gg 1$, cf. (2.15).

However, off the Snell angle, although the facet term vanishes rapidly (as $\theta_{OT} \rightarrow \pi/2$), cf. (2.15), the Bragg terms remain ($\theta_{OT} \leq 85^\circ$), where shadowing becomes strong, and $\overline{S^2} \rightarrow 0$ as $\theta_{OT} \rightarrow \pi/2$, since $(\alpha_{ox}, \alpha_{oy}) \neq 0$. The quantity $\hat{W}(0,0|0)$ is proportional to ℓ_S^2, ℓ_C^2 , cf. (3.6b).

2.4 "Low-Frequency" Acoustic Scatter Cross Sections

Here we apply the results of Sections 8.2, 8.4, especially Eq. (8.9), where $\overline{R}_0^2 \doteq R_0^2 \doteq 1$ and $\overline{S}^2 \doteq S^2 \sim 1$ (for $\theta_{OT} < 85^\circ$), so that $\Delta_{RS} \doteq 0$, (8.9a), for these cases of small Rayleigh numbers $R_{g,c,S} \ll 1$. We obtain the following incoherent and coherent cross sections, from (2.6), (2.10):

$$\begin{aligned} \hat{\sigma}_{inc}^{(0)}|_{R_{g,c,S} \ll 1} &\doteq \frac{k_o^4}{16\pi^2} \left\{ [b_o^4 \sigma_g^2 \hat{w}_g (2\alpha_o k_o |_{x,y} | 0) \right. \\ &\quad \left. + N_{Gc}^{(0)} (2\alpha_o |_{x,y})_{inc} w_c (2\alpha_o k_o |_{x,y} | 0)]_G + N_{GS-inc}^{(0)} \sigma_S^2 \hat{w}_S (2\alpha_o k_o |_{x,y} | 0) \right\} \end{aligned} \quad (2.24)$$

where $\sigma_g^2 \equiv \langle c_g^2 \rangle$, and (2.14) gives the respective tilt-factors, $N^{(0)}$, cf. (7.32)-(7.33) for details. When gravity waves are present, the contributions of the "capillary" component and the soliton-ripples can usually be neglected, so that (2.24) reduces to

$$\hat{\sigma}_{inc}^{(0)}|_{R_g \ll 1} \doteq \frac{k_o^4 b_o^4}{16\pi^2} \sigma_g^2 \hat{w}_g (2k_o \alpha_o |_{x,y} | 0). \quad (2.24a)$$

Other combinations of the various terms of (2.24) are possible, according to the presence or absence of the soliton ripples or the gravity-capillary wave surface.

Here all components of the composite surface appear as Bragg (or resonance) scatter terms, as expected. However, at extreme grazing angles $\overline{S} \rightarrow 0$, so that (2.24), (2.24a) vanish because of shadowing. At somewhat larger grazing angles ($\phi = 10^\circ$, say) the gravity-wave component can be ignorable vis-à-vis the soliton-ripple contribution, because of the factor $b_o^4 (= (\cos \theta_{OT} + \cos \theta_{OR})^4)$, cf. Eq. (3.2c) ff., which in turn is considerably larger than the "capillary" contribution. The latter can be important, however, if the local wind conditions are

such that there are no ripples. As long as $\theta_{OT} (< 0(85^\circ))$ we may expect (2.24) to be nonvanishing, with $\bar{s} \sim 1$.

For the coherent scatter cross section we apply (8.7) to (2.10b) to obtain

$$\hat{\sigma}_{\text{coh}}^{(0)} \Big|_{\text{"low freq"}} \approx \frac{(R_{OT} + R_{OR})^2}{R_{OT}^2} \frac{\bar{s}^{-2} \bar{R}_O^{-2} A_1}{4\pi^2} \left\{ \alpha_{OZ}^2 e^{-\frac{3k_O^2}{4} \left[\frac{(2\alpha_{Ox})^2}{A} + \frac{(2\alpha_{Oy})^2}{B} \right]} \right\}$$

$$R_g \ll 1.$$

(2.25)

Here again we are sufficiently in the far-field to set $b_{TR} = 0$, cf. (2.20). From (6.11a), (6.12a), (6.17), we note that $A_1 \alpha_{OZ}^2 \sim (\cos \theta_{OT} + \cos \theta_{OR})^2 / \cos^2 \theta_{OT}$ generally. Since $A, B \ll 1$, cf. Sec. 6.3, Eq. (6.17), the exponential term in (2.25) ensures that $\hat{\sigma}_{\text{coh}}^{(0)}$ is very small, unless $(\alpha_{Ox} = \alpha_{Oy} \neq 0)$.

Accordingly, in special cases we have:

A. Backscatter

From (2.18) we have $\theta_{OR} = \theta_{OT}$; $\phi_{OT} = \pi/2$ again, so that $\alpha_{Ox} = 0$, $\alpha_{Oy} = \sin \theta_{OT}$, and $R_{OR} = R_{OT}$, etc., with (6.18). Equation (2.24) reduces directly to

$$\hat{\sigma}_{\text{incoh}}^{(0)} \Big|_{R_{OT} \text{ "low-freq"}} \approx \bar{s}^{-2} \bar{R}_O^{-2} \frac{k_O^4}{16\pi^2} \left\{ [16 \sigma_g^2 \cos^4 \theta_{OT} \hat{w}_g(0, 2k_O \sin \theta_{OT} | 0) \right. \\ \left. + N_{Gc}^{(0)}(\theta_{OT}) \text{inc } w_c(0, 2k_O \sin \theta_{OT} | 0)]_G \right. \\ \left. + N_{GS}^{(0)}(\theta_{OT}) \text{inc } \sigma_S^2 w_S(0, 2k_O \sin \theta_{OT} | 0) \right\}.$$

(2.26)

where now the tilt-factors are given by (2.14a,b) and (7.32)-(7.33).

For the coherent component of backscatter, we see that, similarly,

(2.25) reduces to

$$\sigma_{\text{coh}}^{(0)} \Big|_{\substack{R_{OT} \\ \text{"low-freq"}}} \doteq \frac{1}{\pi^2} \bar{R}_0^{-2} \bar{S}^2 A_1(\theta_{OT}) \cos^2 \theta_{OT} e^{-3k_0^2 \sin^2 \theta_{OT}/B(\theta_{OT})},$$

$$R_g \ll 1,$$

(2.27)

which reduces still further with the help of (6.11) in (6.18), to

$$\sigma_{\text{coh}}^{(0)} \doteq \bar{S}^2 \bar{R}_0^{-2} \frac{1}{\pi A} (a_T^2 \cos^2 \theta_{OT} + b_T^2 \sin^2 \theta_{OT})^{-\frac{1}{2}} \cos \theta_{OT}$$

$$\cdot e^{-3k_0^2 \tan^2 \theta_{OT}/2A(a_T^2 \cos^2 \theta_{OT} + b_T^2 \sin^2 \theta_{OT})}. \quad (2.27a)$$

This in turn reveals the explicit dependence on θ_{OT} . In particular, $A = 2A_T/R_{OT}^2 \ll 1$, so that $\sigma_{\text{coh}}^{(0)}$ here is always small, unless $\theta_{OT} = 0$ (vertical incidence), cf. Fig. 2.2a. Then (2.27), (2.27a) become*

$$\sigma_{\text{coh}}^{(0)} \Big|_{\substack{\text{vert} \\ \theta_{OT}=0}} \doteq \frac{1}{\pi^2} A_1(\theta_{OT} = 0) = \frac{1}{\pi A a_T}, \quad R_g \ll 1, \quad (2.28)$$

since $\bar{S} = 1$ and $\bar{R}_0 \doteq 1$: there is no shadowing at vertical incidence and $|R_0| \doteq 1$ for these water/air interfaces. Of course, for large Rayleigh numbers ($R_g \gg 1$), $\sigma_{\text{coh}}^{(0)} \rightarrow 0$ according to (2.15) as expected: when the surface is rough, coherence is destroyed.

*For a_T, b_T , see Eqs. (6.7), (6.11a), (6.12a); $0 < a_T \leq 1$; $0 \leq b_T \leq 1$.

B. Bistatic Scatter in the Snell Direction

From (2.19) we have here $\theta_{OR} = \theta_{OT}$; $\theta_{OT} = \pi/2$ ($= \phi_{OR} - \pi/2$), with $\alpha_{ox} = \alpha_{oy} = 0$; $\alpha_{oz} = \cos \theta_{OT}$, $L_0 > 0$. Thus, with the help of (6.19) we see that (2.24) for the incoherent scatter cross section reduces directly to

$$\delta_{\text{incoh}}^{(0)} \Big|_{\text{Snell}} \Big|_{\text{"low-freq"}} = \frac{\overline{s}^2 \overline{R}_0^2 k_0^4 \cos^4 \theta_{OT}}{\pi^2} \left[\{ \sigma_g^2 \hat{w}_g(0,0|0) + w_-(0,0|0) \} \right]_G + \sigma_S^2 \hat{w}_S(0,0|0) \Big]$$

(2.29)

with the help of (2.14a,b). This is the "low-frequency" ($R_g \ll 1$) analogue of (2.24) above, showing again the (first-order) Bragg scatter contributions of both wave surface components, e.g., the gravity-capillary surface (G) and the soliton-ripples (S), which ride upon it. Here from (2.14), $N_{GC}^{(0)} = N_{GS}^{(0)} = 16 \alpha_{oy}^4 = 16 \cos^4 \theta_{OT}$. The normalized spectra, \hat{w} , are seen to be proportional to the (mean-square) correlation scales of the respective surfaces. Because of the small Rayleigh numbers for the large-scale component (g), the tilt effects are negligible here. As grazing incidence is approached ($\theta_{OT} \rightarrow \pi/2$), $\delta_{\text{incoh}}^{(0)}$ vanishes both because of the $\cos^4 \theta_{OT}$ factor and from the fact that $\overline{s}^2 \rightarrow 0$, ultimately.

For the coherent scatter cross section in the Snell direction, (2.25) now reduces to

$$\delta_{\text{coh}}^{(0)} \Big|_{\text{Snell}} \Big|_{\text{"low-freq"}} = \left(\frac{R_{OT} + R_{OR}}{R_{OT}} \right)^2 \frac{\overline{s}^2 A_1}{4\pi^2} \cos^2 \theta_{OT} \\ = \left[\frac{R_{OR}^2 (R_{OT} + R_{OR})^2}{R_{OT}^2 + R_{OR}^2} \right] \frac{\overline{s}^2 \cos \theta_{OT}}{4\pi^2 A_T \sqrt{a_T^2 \cos^2 \theta_{OT} + b_T^2 \sin^2 \theta_T}}$$

(2.30)

($\overline{R}_0^2 \doteq 1$), $R_g \ll 1$, where we have used (6.19) again. Equation (2.30) also vanishes as $\theta_{OT} \rightarrow \pi/2$, as expected. In the special case where $R_{OR} = R_{OT}$, (2.30) simplifies further to

$$\delta_{\text{coh}}^{(0)} \Big|_{\text{Snell "low-freq"}} \doteq \overline{s}^2 \frac{R_{OT}^2}{2\pi^2 A_T} \cos \theta_{OT} (a_T^2 \cos^2 \theta_{OT} + b_T^2 \sin^2 \theta_{OT})^{-1/2} \quad (2.31)$$

$R_g \ll 1.$

In the special case where $\theta_{OT} = 0$ we get the backscatter result (2.28).

2.5 Analytic Comparisons with Recent Results

Analytic comparisons with earlier work now provide us with various checks on the accuracy and assumptions of the present analysis. In addition, they indicate a variety of differences, which stem mainly from our different choice of physical model, as well as a number of technical differences in the analysis and some definitions. These will become apparent as we continue:

A. Tolstoy and Clay [9]

We consider first incoherent backscatter. From Eq. (6.75) of [9], wherein $\langle \zeta^2 \rangle = \sigma_{G(x=y)}^2$, $\gamma_{\text{back}} = k_0 \cos \theta_{OT}$, $\kappa^2/2\gamma^2 = (\alpha_{ox}^2 + \alpha_{oy}^2)/2 \cos^2 \theta_{OT}$, in our notation, with $\phi_{OT} = \pi/2$, here, so that $\alpha_{ox} = 0$, $\alpha_{oy} = \sin \theta_{OT}$, we see at once that

$$\begin{aligned} \text{(back): } \delta_{T+C, \text{inc}}^{(0)} \Big|_{R_g \gg 1} &\equiv \text{Eq. (6.75)} \Big|_{T+C} = \frac{R_0^2 e^{-\frac{\tan^2 \theta_{OT}}{2\sigma_{G(y=x)}^2}}}{8\pi\sigma_{Gy}\sigma_{Gx} \cos^4 \theta_{OT}} \\ &= \frac{R_0^2}{4\pi} \left(\frac{\sec^4 \theta_{OT} e^{-\frac{\tan^2 \theta_{OT}}{s^2}}}{s^2} \right), \quad s^2 = 2\sigma_{G(x=y)}^2, \end{aligned} \quad (2.32)$$

which is just the first term of our more general result for truly two-

component surfaces, (2.21) above, for the now isotropic (gravity) wave surface at "high-frequencies."

Moreover, since our

$$\frac{\alpha_{0x}^2 + \alpha_{0y}^2 + \alpha_{0z}^2}{\alpha_{0z}/2} = 2f(\theta)_{T+C}, \quad \text{Eqs. (6.23), (6.25), [9],} \quad (2.33)$$

we readily see that the Tolstoy and Clay result (6.74) [9] for general bistatic (incoherent) scattering in the "high-frequency" régime becomes

$$\begin{aligned} \text{(bistatic): } \delta_{T+C, \text{inc}}^{(0)} | R_g \gg 1 &\equiv \text{Eq. (6.74)} = \\ &= \left(\frac{(\alpha_{0x}^2 + \alpha_{0y}^2 + \alpha_{0z}^2)^2}{\alpha_{0z}/2} \right) \frac{R_0^2}{4\pi b_0^2} \left(\frac{e^{-\frac{\tan^2 \theta_{OT}}{s^2}}}{s^2} \right), \quad (2.34) \\ s^2 &= 2\sigma_{g(x=y)}^2, \end{aligned}$$

which is, again, precisely the first term of our result (2.21). In the earlier work the effects of shadowing are neglected, e.g., $\bar{s}^2 = \frac{2}{s^2} \approx 1$.

Similarly, for the "low-frequency" cases ($R_g \ll 1$) we have in our terminology, $r'_0 |_{T+C} \approx R/\sqrt{2}$, cf. (6.56), [9], so that (with R_0^2 reinserted in (2.24)) we get

$$\begin{aligned} \text{(bistatic): } \delta_{T+C, \text{inc}}^{(0)} | R_g \ll 1 &\equiv \text{Eq. (6.58), [9]} = \frac{\overline{R_0^2 k_0^2 b_0^4}}{16\pi^2} W_c(k|0), \\ e^{-Rg} &\approx 1, \end{aligned} \quad (2.35)$$

This is once more just the first term of our more general result (2.24). (Here we have replaced $2f(\theta)_{T+C}$ by $b_0 = \cos \theta_{OT} = \cos \theta_{OR}$,

with $\gamma = b_0/2$, since in these low-frequency cases we do not integrate by parts (e.g., (7.27d), etc. vs. p. 198, [9]), employing essentially the Eckart approximations $\hat{n}_g \cdot 2\alpha_0/n_z \doteq -2\alpha_{0z}$, [32].)

The coherent scatter cross sections (with $f_{T+C} = b_0/2$ again, $A_{T+C} = A_1$) at all frequencies, e.g., Eq. (6.61) of Tolstoy and Clay [9] vs. (2.15) above likewise agree, except in the directional exponential: our result is

$$e^{-\frac{3k_0^2 R^2}{2} (\alpha_{0x}^2 + \alpha_{0y}^2)} \quad \text{vs.} \quad e^{-2k_0^2 R^2 (\alpha_{0x}^2 + \alpha_{0y}^2)} \Big|_{T+C} \quad (2.36)$$

The discrepancy arises because no approximations are made in the evaluation of our beam pattern integrals, cf. $I_1(2\alpha_0)$, (6.38), (6.39), whereas approximations are made in the former (T+C) evaluation.

In general, Tolstoy and Clay [9] also employ the familiar Tangent Plane (Kirchoff) approximation in arriving at their results, as do we here. Since they assume a single-scale wave surface, they, of course, do not obtain the capillary and nonvanishing (as $\theta_{0T} \rightarrow \pi/2$) (ripple-) components with decreasing grazing angle ($\phi = \pi/2 - \theta_{0T}$), cf. the second and third terms of (2.13) above.

B. McDaniel and Gorman [3], [4]

Using a two-scale surface model, McDaniel and Gorman [3], [4] omit the specular-point contribution (viz., the first term of (2.21)) and concentrate on the small-scale capillary wave component, which is dominant at high-frequencies and small grazing angles in their model (but not in ours). Their evaluation of the backscatter cross section for this capillary term embodies a Kirchoff approximation for the large-scale gravity wave surface component, and a perturbation technique [requiring small rms heights ($\sigma_c^2 \ll 1$) and slopes ($\sigma_{cx,y}^2 \ll 1$)] for the small-scale component. Moreover, they replace the "tilt-factor" $N_{Gc}^{(0)}$ in (2.21) by an average over a local grazing angle (as suggested by Bachmann [29]), which contains an estimate of the shadowing effects. Their treatment postulates the capillary waves to be a separate wave structure from the gravity wave component, on which the former con-

sequently ride [so that if this were the case the appropriate "tilt-factor" would have the form of $N_{G(S=c)}^{(0)}$, (2.14a), now, rather than $N_{Gc}^{(0)}$, (2.14b)]. Our physical model [cf. Sec. 2.1] treats the so-called "capillary" waves as part of the continuous gravity-capillary wave surface régime, where the former evolves naturally into the latter via the (nonlinear) mechanism of the soliton-ripples generated locally by the near-surface wind.

Noting [cf. Sec. 7.3 and (2.2a,b)] that our tilt-factor $N_{GS}^{(0)}$ is derived from

$$\langle (\hat{n} \cdot 2\alpha_0)^4 / n^2 \rangle_{G=g+c} \doteq 16 \langle (\hat{n}_G \cdot \alpha_{0\text{-back}})^4 \rangle_G \doteq 16 \langle (\hat{n}_g \cdot \underline{k})^4 \rangle_S \quad (2.37)$$

in the McDaniel-Gorman notation (cf. (25), [4] and from (16), [4]), and that their wave number surface spectral density $W(2\underline{k}_\perp)_{\text{McD+G}} = (2\pi)^{-1} W_c(\underline{k}|0)_{\text{Mid}}$, cf. (7.51), we find at once that, formally,

$$\begin{aligned} [3^{\text{rd}} \text{ term of (2.21)} \equiv \hat{\sigma}_{S\text{-inc}}^{(0)}] &\doteq \frac{k_0^4}{\pi^2} \langle (\hat{n}_G \cdot \underline{k}/k_0)^4 \rangle_S 2\pi W_S(2\underline{k}_\perp)_{\text{McD+G}} \\ &= \frac{2}{\pi} \langle (\hat{n}_G \cdot \underline{k})^4 \rangle_S W_S(2\underline{k}_\perp)_{\text{McD+G}}. \end{aligned} \quad (2.38)$$

Here our actual ripple-surface (S) replaces the "capillary" component, which in their model rides on the gravity-wave structure. [McDaniel and Gorman, of course, use $W_c(2\underline{k}_\perp)_{\text{McD+G}}$ in place of $W_S(2\underline{k}_\perp)_{\text{McD+G}}$, where $\sigma_c^2 \ll \sigma_S^2$, cf. Secs. 3.1, 3.2, and omit the soliton-ripples.]

Thus, our small-scale results (in (2.21)) reduce essentially (but not exactly) to that of McDaniel and Gorman [3], [4] if we were to replace our ripple-surface by a similarly generated, now independent, capillary wave surface ($S \rightarrow c$), and drop the "capillary" component in (2.21), so that only the specular-point scatter term and the ($S \rightarrow c$) small-scale terms remain. [Since high frequencies and small grazing angles are primarily considered in their work, the specular-point scatter contributions may be dropped as negligible vis-à-vis the other components, cf. (3.1) ff.] The various analytic differences between the two treatments arise from the following:

- (i). Our approach uses the Tangent Plane (Kirchoff) method on the total surface, including the soliton ripples. This leads to a "tilt-term" of the form (2.37) above, which, however, reduces here to the simple result

$$\left\langle \frac{(\hat{n}_G \cdot 2\alpha_0)^4}{n_z^4} \right\rangle$$

in all such cases, since $n_z^{-1} = O(1)$, cf. (2.2b), (2.14a), etc.

- (ii). Reference [4] also outlines a similar approach, employing the Kirchoff method on the total surface, vide Appendix A, [4]. Moreover, a tilt-factor of the form $N_{GC}^{(0)}$, (2.14b), is correctly obtained (however, with a factor k_0^2 omitted in Eq. (A14), [4], because of a corresponding omission in going from Eq. (A10) to (A12) in the analysis [4]). This tilt factor, of course, is incapable of ensuring a non-vanishing result (as $\theta_{OT} \rightarrow \pi/2$), as we have already remarked above, (2.14b) et seq., and also the discussion in Sec. 2.1. There is now no separate ripple-term, however, in the analysis [4], Appendix A. What was the separate "capillary" wave surface has now been absorbed properly into the gravity-capillary wave continuum. This approach does not require small slopes, or small heights, unlike the perturbation techniques [4], [33].
- (iii). We perform the "tilt"-averaging directly on $(\hat{n}_G \cdot 2\alpha_0)^4$, etc. (as does Kur'yanov [21], [33]), without the ad hoc introduction of a local grazing angle, θ_g , which, moreover, does not account for the general anisotropy of the wave surface slopes.
- (iv). In the present treatment the shadowing and reflection coefficients are handled by the (approximate) methods of Sec. 7.4C, based on Bass and Fuks [1] as indicated. (Unless we are dealing with angles larger than 85° (say 88°), the shadowing effects are all small and $\bar{s}^2 = \bar{s}^2 \approx 1$).

The really critical difference between our approach and that of McDaniel and Gorman [3], [4] lies in the choice of physical model, since there are no major differences resulting from the various analytic methods employed. We choose a soliton-ripple mechanism, in addition to the gravity-capillary wave surface, as explained in Sec. 2.1. They employ only the latter, treating the "capillary" component as a separate component riding on the gravity-wave structure, rather than as a continuous, high-frequency part of this wave surface as a whole. They explain observed discrepancies between experimental and theoretical cross sections in terms of a near-surface bubble mechanism. This is certainly a possible mechanism, but not necessarily the only one, particularly when (sufficient) bubbles are not present [6]. (See Secs. 1 and 4.1 ff.)

C. Kur'yanov [21], [33]

Kur'yanov employs a two-scale wave surface model, implicitly in the form (2.13) (where we omit the "capillary" term). He uses the perturbation technique, which requires small (rms) wave heights and slopes. For the contribution of the small-scale surface, whatever the physical mechanism may be, he obtains a tilt-factor of the form (in our notation)

$$\begin{aligned}
 16 \langle (\hat{n}_G \cdot \underline{\alpha}_{0\text{-back}})^4 / n_z^2 \rangle_G &\doteq 16 \langle (\hat{n}_G \cdot \underline{\alpha}_{0\text{-back}})^4 / n_z^2 \rangle_{G\text{-Mid}} \\
 &\doteq 16 \langle (\hat{n}_G \cdot \underline{\alpha}_{0\text{-back}})^4 / n_z^4 \rangle_G
 \end{aligned}
 \tag{2.39}$$

cf. Eq. (33.22) of [1], again since $\hat{n}_G = \hat{i}_x \zeta_{Gx} + \hat{i}_y \zeta_{Gy} - \hat{i}_z$, cf. (2.2b) here. This, in turn with the fact that Kur'yanov's and our (normalized) wave number spectra are related by $4\pi^2 \hat{w}(\underline{k}_\perp | 0)_K = \hat{w}(\underline{k}_\perp | 0)_{\text{Mid}}$, reduces our result (the third term of (2.21) here) directly to the form (2.38) above, with $w(2\underline{k}_\perp)_{\text{McD+G}}$ replaced by $2\pi\sigma_S^2 \hat{w}_S(\underline{k}_\perp | 0)_K$, or to Eqs. (33.16), (33.22) of [1]. Thus, Kur'yanov's result and ours (2.21) are essentially equivalent analytically, although different methods (e.g., Kirchoff vs. perturbation) are used to achieve them. Of course, physically, Kur'yanov says nothing about the specific soliton-ripple

mechanism itself, nor does he consider the gravity-capillary wave surface directly, and split it into two separate physical components, in the calculation of the small-scale Bragg scatter component.

D. Barrick and Bahar [5], [22], [23], [25], [30], [31]

A little later than Tolstoy and Clay [9], and by a different approach, Barrick [5] obtained the high-frequency or "optimal-limit" contribution, namely the so-called "specular-point" scattering component of the total scattering cross section $\sigma_{\text{incoh}}^{(0)}$. This is the first term of (2.13). Subsequently, by a more general approach, Bahar [23], [30], [31] has shown that for the conditions assumed here (cf. (2.20)), the two-component (gravity-capillary) portion of our ("three-component") result (2.13) can be alternatively derived, and similarly for the third, independent component postulated here. In these papers Bahar has considered the more general problem of electromagnetic (EM) scattering from random rough surfaces.

If we associate formally Bahar's (and Barrick's) results for horizontal polarization (HH) with our results for acoustic scattering, we see that the various components of (2.13) are essentially identical, in form, to the corresponding EM results, provided that we note that the definitions of the scattering cross sections in the EM case contain a factor 4π (sterradians), cf. (32) of [30] with (2.6), (2.10) here. Moreover, the relationship between Bahar's and our surface wave number spectra is $\pi^2 W(\mathbf{k}_\perp | 0)_B = W(\mathbf{k}_\perp | 0)_{\text{Mid}}$, cf. (43) of [30], with (7.39), (7.41) ff.

As a specific example, let us consider again the case of backscatter, cf. (2.21). Thus, for weak shadowing ($S^2 \doteq 1$ now) we have from (2.13), omitting the additional soliton-ripple term,

$$\begin{aligned} \sigma_{\text{incoh}}^{(0)} \Big|_{\text{Bahar-Barrick}}^{\text{back}} &= 4\pi \sigma_{\text{incoh}}^{(0)} \Big|_{\text{Mid}}^{\text{back}} \\ &\approx \frac{\pi^2}{R_0^2} \left\{ \frac{e^{-\frac{\tan^2 \theta_{OT}}{s^2}}}{s^2 \cos^4 \theta_{OT}} + \frac{\pi}{4} k_{OGc}^4 W_c^{(0)}(\mathbf{k}_\perp | 0)_{\text{Bahar}} \right\}, \quad (2.40) \end{aligned}$$

for isotropic gravity-capillary wave surfaces in which $s^2 = 2\delta_{G(x=y)}^2$, etc., cf. (2.32). With very small slopes the tilt factor in (2.40) reduces to $\cos^4 \theta_{OT}$, so that the second term becomes precisely the horizontal polarization component of Eqs. (47), (69) of [30], while the first term of (2.40) is just Barrick's result (136), [5], or Eq. (72) of [30], where $\phi_{OT} = \pi/2$, $\underline{k}_\perp = (0, 2k_0 \sin \theta_{OT})$.

With the alternative two-scale model in which the small-scale component actually rides upon the large-scale surface, the tilt factor has the form $N_{GS}^{(0)}$, (2.14a), which is non-vanishing as $\theta_{OT} \rightarrow \pi/2$. (The counterpart of this in Bahar's results appear in his shadowing terms $\langle S^{(PQ=HH)} \rangle$, cf. Section 4 of [23], and Eqs. (44c) et seq. therein.) Thus, in general our approach yields results equivalent to the more general (and less explicitly tractable) analysis of Bahar [23], [30], based on a "full-wave" theory development, where now Tangent Plane (i.e., Kirchoff) methods can be employed and the small-scale wave surface components have small rms heights (but not necessarily small slopes), as is the case of our model here. We remark, however, that in the case of ocean wave-surfaces, Bahar et al. [25] use a single (i.e., gravity-capillary) wave surface, which is then artificially split into two components for analytic convenience (cf. [23], [24], also). The small-scale component cannot then be considered as riding upon the large-scale component, cf. our discussion in Sec. 2.1 above.

Finally, we remark that except for our and Tolstoy and Clay's [9] analyses, and that of Clay and Medwin [11], which explicitly introduce (gaussian) beam patterns, e.g., specific apertures (cf. Sec. 6 ff.), the other treatments cited here assume uniform beam patterns over some solid angle, vanishing outside this angle. [This is implicit in the choice of reference area, A_{REF} [(2.7d) and Sec. 2.2C], in the definition of the scattering cross section, $\delta^{(0)}$, cf. (2.6), (2.10).] Reconciliation between these different choices of beam pattern is achieved through (2.11), i.e., by appropriate choice of A_{REF} in the definition of $\delta^{(0)}$.

3. Preliminary Numerical Results: High Frequencies and Small Grazing Angles

Since we are concerned in this study primarily with the possibility of obtaining reasonable agreement between theory and experiment without the intervention of scattering by bubbles, as explained above in Section 1, we shall consider only the high-frequency, small grazing angle régime, where the discrepancies between earlier theory and experiment are most pronounced [1]-[4]. Moreover, it is sufficient to consider one typical situation numerically in order to illustrate such discrepancies and potential agreements.

Accordingly, we shall treat the following specific example: (incoherent) backscatter, with $\theta_{OT} = 80^\circ$ ($\phi = 10^\circ$ grazing angle) with $\phi_{OT} = \pi/2$, $f_0 = 20$ kHz, central signal frequency; average near-surface wind velocity $v = 10$ m/sec (≈ 20 knots), cf. Fig. 2.1a. Equation (2.21) is the appropriate relation here for the (back-) scattering cross section $\sigma_{incoh}^{(0)}$. Furthermore, in this example we may ignore the negligible contribution of the specular-point (or facet) scattering term, to write (2.21) as

$$\sigma_{incoh}^{(0)} \Big|_{\substack{R_{OT} \\ R_g \ll 1 \\ \phi_{OT} = \pi/2}} \approx \bar{R}_0^2 \bar{S}^2 \left[\doteq 0 + \frac{k_0^4}{16\pi^2} N_{GC}^{(0)}(\theta_{OT})_{inc} W_c(0, 2k_0 \sin \theta_{OT} | 0) \right. \\ \left. + \frac{k_0^4}{16\pi^2} N_{GS}^{(0)}(\theta_{OT})_{inc} \sigma_s^2 \hat{W}_S(0, 2k_0 \sin \theta_{OT} | 0) \right], \quad (3.1)$$

where the tilt-factors $N_{GC}^{(0)}$, $N_{GS}^{(0)}$ are given by Eqs. (2.14a,b); (the unnormalized two-dimensional wave number spectra are $W_{c,S} = \sigma_{c,S} \hat{W}_{c,S}$, respectively). As noted above (Sec. 2.3) the (non-zero) initial term of (3.1) provides the first-order Bragg-scatter contribution of the high-frequency, or capillary portion of the underlying single wave surface, while the last term gives the (Bragg-) scatter associated with the essentially independent, omni-directional soliton ripples, or "hydraulic jumps" [cf. Sec. 2.1], which ride upon the gravity-capillary wave surface.

Our task here is to evaluate (3.1) and compare the numerical results

with surface models which do not include the soliton ripple mechanism (cf. Sec. 2.5).

3.1 Backscatter with Soliton Ripples: Numerical Examples

In order to compare with currently listed experimental data [4] we shall renormalize our wave number spectra via the relation $W(\underline{k}|0)_{\text{Mid}} = 2\pi W(\underline{k}|0)_{\text{MCD+G}}$, cf. (7.51b). In addition, for our specific numerical example we need the following:

A. Calculations: [$f_0 = 20$ kHz; $\theta_{0T} = 80^\circ$; $v = 10$ m/sec]

$$(1). \quad k_0 = \frac{2\pi}{\lambda_0} = 2\pi f_0 / c_0 = (2\pi) 20 \cdot 10^3 / (1.5) 10^3 = 83.78 \text{ rad m}^{-1};$$

$$\therefore \boxed{k_0^4 = (4.93) 10^7 (\text{rad m}^{-1})^4} ; \quad (3.2a)$$

$$(2). \quad \underline{\phi_{0T} = \pi/2; \theta = 80} : \therefore \alpha_{0x} = 0; \alpha_{0y} = \sin \theta_{0T} = 0.985, \text{ [cf. Eq. (2.21)]} \quad (3.2b)$$

$$\therefore \left\{ \begin{array}{l} \sin \theta_{0T} = 0.985; \sin^2 \theta_{0T} = 0.970; \sin^4 \theta_{0T} = 0.941 \\ \cos \theta_{0T} = 0.174; \cos^2 \theta_{0T} = 3.02 \cdot 10^{-2}; \cos^4 \theta_{0T} = 9.09 \cdot 10^{-4}; \end{array} \right\} \quad (3.2c)$$

(3). From Cox and Munk [35], esp Eq. (6.76) of [9], we have for the mean-square slopes:

$$\sigma_{g(x=y)}^2 = (3.0 + 5.12v) 10^{-3} = \boxed{5.42 \cdot 10^{-2}} ; \quad (3.2d)$$

(4). From (2.14a) and (7.56a) we get here specifically

$$\begin{aligned} N_{\text{GS-inc}}^{(0)} &= 16 \{ 3(5.42)^2 10^{-4} (0.941) \\ &\quad + 6(5.42 \cdot 10^{-2})(0.970)(3.02 \cdot 10^{-2}) + 9.09 \cdot 10^{-4} \} \\ &= 16 \{ 8.29 \cdot 10^{-3} + 9.53 \cdot 10^{-3} + 0.91 \cdot 10^{-3} \} \\ &= \boxed{16(1.87 \cdot 10^{-2})} . \end{aligned} \quad (3.2e)$$

In the same way we have from (2.14b)

$$\begin{aligned} N_{GC-inc}^{(0)} &= 16 \{ [(5.42 \cdot 10^{-2})(0.970) + 3.02 \cdot 10^{-2}] 3.02 \cdot 10^{-2} \} \\ &= \boxed{16(2.50 \cdot 10^{-3})} . \end{aligned} \quad (3.2f)$$

B. Wave Number Spectra

For the set of soliton ripples, or hydraulic jumps, which ride upon the rough gravity-capillary wave surface, we develop the following elementary second-moment model.

A reasonable approximation of the wave shape, or "hump," is given by the gaussian wave form, for a typical wavefront traveling in some direction ϕ , viz:

$$\xi(\underline{r}, t) = \hat{i}_r \zeta_S e^{-4r^2/L^2} \Delta 1(r - c_S t) , \quad (3.3)$$

where $\hat{i}_r = \hat{i}_x \cos \phi + \hat{i}_y \sin \phi$, $r = \sqrt{x^2 + y^2}$, and where $\Delta 1$ is a unit distance "window" which moves along with the soliton, at speed c_S . It is nonzero for $|r - c_S t| \leq 2L$, where $2L$ is the spread of the hump to, say, within e^{-4} ($\approx 2\%$) of its maximum value, cf. Fig. 16, [16], p. 465, etc.

We determine the second-moment functions for an (ensemble of) single typical humps from

$$M_S(\underline{\Delta r}, t) \equiv \langle \xi(\underline{r}_1, t_1) \cdot \xi(\underline{r}_1 + \underline{\Delta r}, t_1 + \Delta t) \rangle \quad (3.4a)$$

$$\begin{aligned} &= \frac{\zeta_S^2}{2L} \left\langle \int_{-\infty}^{\infty} e^{-4r_1^2/L^2} \cdot e^{-4(r_1 + \Delta r)^2/L^2} dr_1 \right\rangle_{\phi} \langle \Delta 1_1 \Delta 1_2 \rangle_{t_1} \\ &= \frac{\zeta_S^2}{2L} \rho_L(\tau) e^{-4\Delta r^2/L^2} \int_{-\infty}^{\infty} e^{-8(r_1^2 + r_1 \Delta r)/L^2} dr_1 \end{aligned} \quad (3.4b)$$

where

$$\rho_L(\tau) = 1 - |\tau|/T_L = 1 - \frac{c_S |\tau|}{2L} , \quad c_S |\tau| \leq 2L; = 0, \text{ otherwise.} \quad (3.4c)$$

Since we are interested here in the intensity, we set $\tau = 0$ in (3.4c), e.g., $\rho_L(0) = 1$. Moreover, since we have in reality a sum of such independent solitons traveling in all directions on the broken, large-scale surface, we evaluate (3.4b) and write finally in this isotropic case

$$M_S(\underline{\Delta r}, 0) = \sigma_S^2 e^{-\Delta r^2 / 2\ell_S^2} ; \quad \sigma_S^2 = \frac{\bar{N}}{4} \zeta_S^2 \sqrt{\pi} ; \quad \ell_S = L/2, \quad \Delta r^2 = \Delta x^2 + \Delta y^2, \quad (3.5)$$

where \bar{N} average number of solitons overlapping at any instant and positions. Not surprisingly, from a gaussian waveform we obtain a gaussian second-moment function. (Note the "d.c." component embodied in (3.5), since $\langle \zeta \rangle_L > 0$.)

From (7.36), (7.41) we obtain the corresponding two-dimensional wave number spectrum

$$W_S(\underline{k}|0) = \int_{-\infty}^{\infty} M_S(\underline{\Delta r}, 0) e^{i\underline{k} \cdot \underline{\Delta r}} d(\underline{\Delta r}) = 2\pi \ell_S^2 \sigma_S^2 e^{-[(2k_{ox}\ell_S)^2 + (2k_{oy}\ell_S)^2]/2} \quad (3.6a)$$

which reduces here, cf. (3.2), specifically to

$$W_S(0, 2k_o \sin \theta_{oT} | 0) = 2\pi \sigma_S^2 \ell_S^2 e^{-2(k_o \ell_S \sin \theta_{oT})^2} \quad (3.6b)$$

Our next step is to note from (7.51b) that

$$W_S(\underline{k}|0)_{Mid} = 2\pi W_S(\underline{k}|0)_{McD+G} = 2\pi \{ \sigma_S^2 \ell_S^2 e^{-2(k_o \ell_S \sin \theta_{oT})^2} \}, \quad (3.7)$$

so that, writing $N_{gS-inc}^{(0)} \equiv 16\hat{N}_{gS-inc}^{(0)}$, we convert the second (non-vanishing) term of (3.1) to the backscatter cross section attributable to the soliton ripples in the McD-G normalization:

$$\sigma_{S-inc}^{(0)} \Big|_{McD+G} = \frac{2}{\pi} k_o^4 \hat{N}_{gS-inc}^{(0)}(\theta_{oT}) \bar{S}^2 \bar{R}_0^2 \{ \sigma_S^2 \ell_S^2 e^{-2(k_o \ell_S \sin \theta_{oT})^2} \} \quad (3.8)$$

It is this result we next examine numerically for our specific example above.

C. A Numerical Example

Preliminary (though sparse) observations [14], [15], [17], [18] suggest the following ranges of values for $2L$, σ_S :

$$\boxed{L = 1.6-2.0 \text{ cm.}} : \therefore L = 2\ell_S = \sqrt{2} L_S \left\{ \begin{array}{l} \therefore \ell_S = 0.8-1.0 \text{ cm.} \\ \therefore L_S = 1.13-1.41 \text{ cm.} \end{array} \right. \quad (3.9a)$$

$$\boxed{\sigma_S = 0.2-1.0 \text{ cm.}} ; \therefore \sigma_S^2 = 4 \cdot 10^{-6} \text{ m}^2 - 10^{-4} \text{ m}^2; \quad (3.9b)$$

here L_S is the "correlation distance," where $\Delta r^2 = L_S^2$ is such that $M_S = e^{-1}$ of its maximum value.

For our example we select as representative values:

$$\boxed{L = 1.8 \text{ cm.}; \therefore \ell_S = 0.90 \text{ cm.}} ; \sigma_S = 0.2-1.0 \text{ cm.} \quad (3.10)$$

Moreover, at $\theta_{OT} = 80^\circ$, $\bar{s}^2 \doteq 1$, and for the water/air interface, $\bar{R}_0^2 \doteq 1$. Combining (3.2a,d,e) in (3.8) thus gives us, with (in meters)

$$\begin{aligned} \ell_S^2 e^{-2(k_o \ell_S \sin \theta_{OT})^2} &= (0.90 \cdot 10^{-2})^2 e^{-2\{(83.78)(0.90 \cdot 10^{-2})(0.985)\}^2} \\ &= (8.1 \cdot 10^{-5}) e^{-2(0.743)^2} = 8.1 \cdot 10^{-5} (e^{-1.104}) \\ &= (8.1 \cdot 10^{-5})(0.332) = 2.69 \cdot 10^{-5} \text{ m}^2, \end{aligned} \quad (3.11)$$

the following expressions for the soliton scatter cross section, since $2/\pi = 0.637$:

$$\hat{\sigma}_{S\text{-inc}}^{(0)} = \left\{ \begin{array}{l} (0.637) (4.93 \cdot 10^7) (1.87 \cdot 10^{-2}) (2.69 \cdot 10^{-5}) \cdot \sigma_S^2 \\ 2/\pi \quad k_o^4 \quad \hat{N}_{gS}^{(0)} \quad \hat{W}_S |_{McD+G} \end{array} \right. \quad (3.12a)$$

$$\therefore \boxed{\hat{\sigma}_{S\text{-inc}}^{(0)} |_{20 \text{ kHz}} = 1.58 \cdot 10^{-2} \sigma_S^2} . \quad (3.12b)$$

Using (3.9b) we may construct the following short Table:

Table 3.1: Eq. (3.12b); [$\lambda_S = 0.90$ cm; $v = 10$ m/sec; $f_0 = 20$ kHz]:

σ_S (cm)	σ_S^2 (m ²)	$\hat{\sigma}_S^{(0)}$	$\hat{\sigma}_S^{(0)}$ (db)	$\hat{\sigma}_S^{(0)}$ (db): with Kirchoff corrections=+2.5 db
0.2	$4 \cdot 10^{-6}$	$6.32 \cdot 10^{-5}$	-42.0	-39.5
0.3	$9 \cdot 10^{-6}$	$1.42 \cdot 10^{-4}$	-38.5	-36.0
0.4	$1.6 \cdot 10^{-5}$	$2.53 \cdot 10^{-4}$	-36.0	-33.5
0.5	$2.5 \cdot 10^{-5}$	$3.95 \cdot 10^{-4}$	-34.0	-31.5
0.6	$3.6 \cdot 10^{-5}$	$5.69 \cdot 10^{-4}$	-32.4	-29.9
0.8	$6.4 \cdot 10^{-5}$	$1.01 \cdot 10^{-3}$	-30.1	-27.5
1.0	$1.0 \cdot 10^{-4}$	$1.58 \cdot 10^{-3}$	-28.0	-25.5

[The Kirchoff correction used here is taken from Fig. 13 of [4]; see the discussion in Section V of [4].] This correction factor arises because of the failure of the "flatness" condition (i.e., large radius of curvature, $b_0 k_0 \rho > 1$) as grazing angles ($\theta_{OT} > 60^\circ$) are approached.]

Experimental results for the frequency ($f_0 = 20$ kHz), grazing angle ($\theta_{OT} = 80^\circ$), and wind speed ($v = 10$ m/sec = 20 knots) chosen here (cf. A above) are cited in Table 3.2 below:

Table 3.2: Experimental Results* [at $f_0 = 20$ kHz; $\theta_{OT} = 80^\circ$; $v = 10$ m/sec]

Source	$\hat{\sigma}_{\text{back-incoh}}^{(0)}$
1. Galubin [36]; also Fig. 1.26 of [2]	-30 db (19 knots)
2. Lilly and McConnell [37]	-29 db (21 knots)
3. Hoover and Kaprocki [38]	-27.5 db (20.5 knots)
4. Roderick [6], at $\theta_{OT} = 81^\circ$	-30(± 1)db(20 knots)

*See Fig. 4 of [4].

On the assumption that the data of Table 3.2 were obtained in an essentially bubble-free environment (there was no "ground-truth" to establish this fact one way or the other), we see on comparison with Table 3.1 that for values of $\sigma_S \geq 0.4$ an acceptable agreement (within a few db) between theory and experiment is obtained when the scattering mechanism is the soliton ripples. [As shown below in Section 3.2,

scattering from the capillary component of the single wave surface is $O(10+ \text{ db})$ smaller.]

It has also been observed that the scatter cross section (for comparatively small grazing angles ($\theta_{OT} > 60^\circ$)) increases with frequency (Fig. 1.26 of [2], and [3]). Let us consider the cases $f_0 = 10 \text{ kHz}$, 20 kHz and compare with Galybin's data (Fig. 1.26 of [2]). From (3.8) we write

$$\frac{\sigma_{S\text{-inc}}^{(0)}(\theta_{20 \text{ kHz}})}{\sigma_{S\text{-inc}}^{(0)}(\theta_{10 \text{ kHz}})} = 2^4 \cdot e^{-1.104+0.276} = 2^4 e^{-0.828} = 7.0 = 8.4 \text{ db.} \quad (3.13)$$

This compares acceptably with a $\sim 7.5 \text{ db}$ estimated difference from Fig. 1.26, [2], and with Roderick's recent results [6].

3.2 Backscatter from Capillary Waves

It remains to examine the effects of the capillary component, $\sigma_{C\text{-inc}}^{(0)}$, in the total backscatter cross section (3.1) at these high frequencies and small grazing angles. Here the physical mechanism is different: the capillary extension of the gravity wave surface is directional and dispersive, with dispersion governed by surface tension forces, unlike the soliton-ripple surface above, which rides upon the former. In what follows we consider very briefly several spectral models of the single wave surface ($g + c$). From these we estimate σ_c , the rms capillary wave height, and the back-scatter cross section $\sigma_{C\text{-inc}}^{(0)}$, in (3.1).

A. Phillips' Spectrum [39]

From Sec. 4.5 of [39] we have Phillips capillary wave number spectrum,

$$\bar{\Psi}(\underline{k})_c = \frac{B'}{\pi k^4}, \quad \hat{\alpha}_0 - \pi/2 < \hat{\alpha} < \pi/2 + \hat{\alpha}_0; \quad B' = 1.5 \cdot 10^{-2}; \quad (3.14)$$

cf. Eq. 4.5.9, [39]. Since $(2\pi)^2 \bar{\Psi}(\underline{k}) = W_a(\underline{k}|0)_{\text{Mid}} = 2\pi W_a(\underline{k}|0)_{\text{McD+G}}$, cf. (7.51), we see that $\sigma_S^{(0)}$ in (3.1) becomes

$$\sigma_{C\text{-inc}}^{(0)} = 4k_0^4 \hat{N}_{gc}(\theta_{OT}) \phi(\underline{k})_c = \frac{1}{4\pi} \hat{N}_{gc}^{(0)} B' / \sin^4 \theta_{OT} = 3.2 \cdot 10^{-6} = -54.9 \text{ db} \quad (3.15)$$

where we have used (3.2f), and $N_{g-inc}^{(0)} = 16\hat{N}_{gc}^{(0)}$, with (3.14), (3.2), etc. This back-scatter cross section is much smaller than our soliton-ripple results (Table 3.1) and the empirical data (Table 3.2). Furthermore, it is independent of frequency, nor does it take into account the dispersive character of the capillary waves, as used here. However, it agrees quite well with Bahar et al.'s results (-55 db) in Fig. 11b, [25], for the case of horizontal polarization (which is the EM analogue of our acoustical case here). [We must subtract 11 db ($= 4\pi$) from $\sigma^{(HH)}$ in Fig. 11b, because of Bahar's definition of $\sigma^{(HH)}$, cf. (2.40) above.]

B. Brown's Spectrum [40]; (Bahar et al., [25])

Since what primarily is important in the wave number spectra appearing in the scattering cross sections, cf. (3.1), is not specific spectral shape but rather the intensity ($\sigma_{c,S}^2$) and spectral spread ($k_0 \ell_{c,S}$), we shall use Brown's spectrum (Eqs. (23), (24) of [25]; [40]) to determine σ_c^2 from Eq. (26) of [25] and apply the result to (3.8), with $\sqrt{2}\ell_{S=c_1} = 1.27$ cm again, cf. (3.10), as a reasonable correlation distance (e^{-1}) for these capillary waves. Taking $k_d = 1.0$ rad cm $^{-1}$ as the wave number at which the (continuous) gravity-capillary wave surface splits into "high"- and "low"-frequency components ([25], discussion and Table 1 therein), we obtain

$$\sigma_c^2 \doteq \frac{B}{2k_d^2} = \frac{4.6 \cdot 10^{-3}}{2(10^{+2} \text{ rad m}^{-1})^2} = 2.3 \cdot 10^{-7} \text{ m}^2: \therefore \sigma_c = 4.8 \cdot 10^{-4} \text{ cm} \doteq \frac{1}{2} \text{ mm.} \quad (3.16)$$

Applying (3.16) with $\ell_c = 1.27$ cm, $f_0 = 20$ kHz, ($v = 10$ m/sec) in (3.8), with (3.2f) replacing $N_{gS}^{(0)}$ since the wave surface is a single surface [e.g., the capillary structure is part of the wave surface, not a separate entity riding on the gravity-wave component (cf. Sec. 2.1)], we get from (3.12a)

$$\sigma_{c-inc}^{(0)} = 2.10 \sigma_c^2 = 4.86 \cdot 10^{-7} = -63.1 \text{ db,} \quad (3.17)$$

which is clearly too small.

Alternatively, using Brown's spectrum, W_T , Eq. (23) of [25], directly in (3.1), with (3.2f) and the conversion relation $W_{Mid} = \pi^2 W_{B+B=Brown}$, cf. (7.51c), we get

$$\sigma_{c-inc}^{(0)} \doteq \frac{2B}{\pi} \hat{N}_{gc}^{(0)} = (0.637)(4.6 \cdot 10^{-3})(2.50 \cdot 10^{-3}) = 7.3 \cdot 10^{-6} = -51.4 \text{ db}, \quad (3.18)$$

which is -40.4 db in Bahar et al.'s [25] definition of scatter cross section, which in turn is $4\pi \times \sigma_{incoh}^{(0)}$ here, cf. (2.6). Comparing this with $\sigma^{(HH)}$, Fig. 11b, [25], we see that (3.18) is about 3.5 db larger than the cross section for horizontal polarization, $\sigma^{(HH)}$, the radar analogue of the acoustic scatter cross section. (The difference is attributable to the particular "tilt-factor" used here.)

In any case, these models give noticeably too small results (in this second instance independent of frequency), and all lack the spectral character appropriate to the particular dispersive nature of capillary waves, cf. Eqs. (7.52) et seq.

C. McDaniel's and Gorman's Results [3], [4]

In two recent papers, [3], [4], McDaniel and Gorman have obtained back scatter cross sections, which are -42 db (including the Kirchoff corrections) for our example above (A), cf. Fig. 4 of [4], and are noticeably below the empirical results, cf. Table 3.2. Their very extensive analysis takes into account the dispersive character of the small-scale, or capillary component, but does not include the suggested independent soliton-ripple mechanism. Moreover, they also show that diffraction effects (including multiple scatter) are quite negligible (Sec. VI, [4]), as we note below in Sec. 2.3 also. We refer the reader to these papers [3], [4] for details; (see also the discussions in Secs. 1, 4 here).

3.3 Backscatter from Diffraction Terms ($k \geq 1$)

Applying (8.17) to our definition (2.6) we see at once that the back- (and, in fact, omni-directional) scatter cross section for the diffuse diffraction component ($k = 1$) in our theory [41]-[43] becomes (cf. Sec. 8.6 ff.)

$$\delta_{\text{incoh}}^{(1)} = \frac{\overline{R_0^2} \overline{S^2}}{16\pi^2} \{ \langle \zeta_g^2 |J_g| \rangle + \langle \zeta_c^2 |J_c| \rangle + \langle \zeta_s^2 |J_s| \rangle \}, \quad (3.19)$$

$$|J_a| \equiv |\zeta_{xx}\zeta_{yy} - \zeta_{xy}^2|_a,$$

which is put to the same scale as the principal contribution $\delta_{\text{incoh}}^{(0)}$, (3.8), for comparison with the data of Table 3.2 and the example of 3.1C, by the relation $2\pi\delta_{\text{incoh}}^{(1)} = \delta_{\text{McD+G}}^{(1)}$, cf. (3.7).

Some simple numerical estimates of (3.19) may be obtained by replacing $\langle \zeta^2 |J| \rangle$ by $\langle \zeta^2 \rangle |J_c|$. We suggest that

$$\overline{\zeta_g^2} = \alpha(10^{-1} \text{ m}^2); \quad |J_g| = \alpha(10^{-6} \text{ m}^{-2}) \therefore \langle \zeta_g^2 |J_g| \rangle \sim \alpha(10^{-7}) = -70 \text{ db}; \quad (3.20a)$$

$$\overline{\zeta_c^2} = \alpha(10^{-5} \text{ m}^2); \quad |J_c| = \alpha(10^0 - 10^{-1}) \therefore \langle \zeta_c^2 |J_c| \rangle \sim \alpha(10^{-5} - 10^{-6}) \\ = \alpha(-50 \text{ to } -60 \text{ db}); \quad (3.20b)$$

$$\overline{\zeta_s^2} = \alpha(2 \cdot 10^{-5} \text{ m}^2); \quad |J_s| = \alpha(10^{-1}) \therefore \langle \zeta_s^2 |J_s| \rangle \sim \alpha(10^{-6}) = \alpha(-60 \text{ db}); \quad (3.20c)$$

where in (3.20b,c) the curvature is comparatively large. Since $(16\pi^2) = -21.2 \text{ db}$, we see that even if these scatter terms are 10 db, or even 20 db, too large, they are ignorable compared to the main capillary (and gravity) contributions $\delta_c^{(0)}$, $\delta_g^{(0)}$ unless there is a special alignment of the former which renders it essentially zero, e.g., at $\phi_{OT} = \pi/2$, and $\hat{\alpha}_0 = 0$, so that the mean direction of the gravity-capillary wave surface is directed at right angles to the beams in backscatter, cf. Fig. 2.1a. The main contributions of the soliton ripples, $\delta_s^{(0)}$, however, dominates the above in any case, and is essentially directional as well.

We may expect the multiple-scatter terms, $\delta^{(k \geq 2)}$, in the scattering cross section (2.8), to be even smaller than the diffuse scatter terms ($k = 1$) above. This corresponds to their negligible contributions as computed by perturbation theory (when the slopes of the capillary and

ripple waves may be regarded as small), cf. Sec. VI of [4]. Thus, when a truly two-component wave surface (in the sense of our present model) is illuminated, we may neglect the diffraction terms ($k \geq 1$) vis-à-vis the Bragg-scatter contributions, as noted in (3.1), for example.

4. Conclusions and Next Steps

As we have already noted in Section 1 above, our principal results are fundamentally theoretical, combined with selected numerical comparisons of our new model with earlier theory and experiment. We summarize below the general new features of this study (Sec. 4.1 ff.) and suggest needed further theoretical and experimental efforts (Sec. 4.2 ff.).

4.1 Principal Results

The new features of our work here are:

- (1). The identification of a potential mechanism for the second component of a composite wind-wave surface which may resolve the often observed discrepancy between theory and experiment at high frequencies and small grazing angles without our postulating a bubble mechanism [3], [4].

This alternative mechanism is the ensemble of soliton ripples, or hydraulic jumps, riding on the main gravity-capillary wave surface, by which the latter is itself generated through the nonlinear action of local near-surface winds, or "cats-paws" [cf. Sec. 2.1 and [14]-[18].] These ripples, broken up into solitons on the wind-driven, rough gravity wave surface, travel with constant speed and are nondispersive, unlike the gravity and capillary waves, cf. Secs. 2.1, 3.1 above, and are directional, according to the local near-surface wind. They disappear when the local wind (momentarily) stops, but are otherwise generated much of the time in usual seas.

Preliminary numerical estimates (Sec. 3.1) indicate quantitatively that this ripple mechanism can account for the previously observed discrepancies between theory and experiment at high frequencies and small grazing angles, when there are no bubbles.

- (2). The development of a truly two-component wave surface model, where the above ripple surface is essentially independent of the single gravity-capillary wave surface on which these soliton-ripples ride.

Analytically, the practical, approximate theory requires three scattering components: (i), large-scale gravity waves ("low"-frequency); (ii), the capillary continuation of these gravity waves ("high"-frequency); and (iii), the independent soliton or hydraulic "jump" ripples, generated by the local wind action.

The divisions of the wave surface into components (i) and (ii) is an insightful technical device [as Bahar et al. [25] have noted, for example], while (iii) is a separate phenomenon. The former yield specular-point scatter (i), which dominates at large grazing angles, and (first-order) Bragg scatter (here) (ii), while (iii) also generates a first-order Bragg scatter, which, however, we suggest is significantly $O(10+ \text{ db})$ larger than the capillary contribution (ii), cf. Sections (3.1), (3.2). Of course, in those intervals when there are no local interacting winds, the capillary component dominates, unless there are sufficient near-surface bubbles. For example, these latter can be comparable to the soliton ripples, producing $O(3 \text{ db})$ increase in the scattering level, which are probably not resolvable within the accuracy of previous experiments. See also [6].

- (3). Verification of the general analytical agreement between the various principal approximate results for the scattering cross sections obtained in the literature [cf. Sec. 2].

Thus, the Kirchoff-Perturbation approaches of [4], [21], [33], for example, and the author's "Kirchoff-Kirchoff" method (cf. Sec. 7.3) yield essentially the same form of Bragg scatter component, albeit with somewhat different "tilt-factors," (cf. (2.37), (2.39)).

In most instances these tilt-factors are approximately equal, because the rms slopes of the large-scale gravity-wave component are themselves quite small, e.g., $\sigma_{gx,y}^2 = O(2,3 \cdot 10^{-2})$. An exception, however, is the tilt-factor, $N_{gc}^{(0)}$, associated with the artificial split of the gravity-capillary wave surface into low- and

high-frequency components: the tilt-factor here vanishes with zero grazing angle, unlike the situations where there is truly a second, separate wave mechanism riding on the first surface, as presented here.

Numerical differences [cf. Sec. 3.2] between the earlier results stem principally from the choice of a wave spectrum model, which in turn depends quite critically on what is the underlying physical mechanism.

Corrections for the well-known limitations of the Kirchoff or Tangent-Plane method are small $O(1-3 \text{ db})$, cf. [4], Section VI, at small grazing angles, vis-à-vis the general level of scattering cross section determined through these earlier models, as they are also when our present wave surface model is employed.

- (4). The observation that the diffraction terms (diffuse scatter ($k = 1$), and multiple-scatter ($k \geq 2$), cf. (3.20), are generally well below [$O(15-20 \text{ db}$, cf. Sec. 3.3] the main contributions of the direct scatter components, e.g., the specular-point scatter components (important at large grazing angles) and the Bragg-scatter terms, which dominate at small grazing angles ($\theta_{OT} > 60^\circ$), and high-frequencies. This agrees with recent results [4] using different theoretical methods (i.e., perturbation techniques).
- (5). From the above it is therefore clear that the large discrepancies between theory and experiment at these critical regions of small grazing angles and high frequencies are to be explained by the proper choice of physical model: the problem is not fundamentally analytical.

We emphasize again that a bubble mechanism can explain the observed discrepancies between theory and experiment, provided, of course, bubbles are actually present in sufficient numbers. Moreover, if bubbles are so present, their effect should add only $O(3 \text{ db} = \text{factor } 2)$ to that already produced by the independent "ripple" surface (on the assumption both mechanisms are comparable scatterers). The presence of bubbles, however,

was unfortunately not quantitatively verified in most of the experimental data cited earlier for comparison with theory, cf. Table 3.2 and refs.

We also emphasize that our proposed soliton-ripple mechanism, although an observed phenomenon, has only been measured to a limited extent, particularly on gravity wave surfaces: our numerical estimates have been inferred from very limited data so far. Thus, while the reliability of the analytical procedures is not in question [cf. (3) above], it has not yet been established that the soliton-ripple mechanism fully explains the observed scattering levels in the absence of bubbles. Further experimental work is required [cf. Sec. 4.2 ff.], to obtain the needed dimensions (height and length) of this mechanism. [We remark that whenever independent measurements verify this mechanism quantitatively, we can then apply acoustic (back-) scattering techniques like those described in detail here to obtain the desired scale and size of these ripple effects in subsequent applications.]

Other new features of our analysis include: (1) explicit development of the rôle of gaussian and omni-directional beam patterns; (2) general second-moment and covariance functions, from which we shall subsequently determine wave surface spectra and related (i.e., doppler) effects; (3) general narrow-band signals and absorptive phenomena; (4) numerical estimates of diffraction contributions; and (5) an extensive discussion of the various approximations, and their conditions, which underly the analytical results.

Finally, we note that our general model here can be applied at once to such special cases which may occur physically as:

- (i). no soliton ripples, just the gravity-capillary wave surface (no local winds): one drops the "S-terms" in our results.
- (ii). soliton-ripples and bubbles: one may use the additional bubble contributions, for example, as treated in [3]. Their effects, of course, will depend strongly on the bubble density, whether or not they are ignorable to, comparable to, or dominate the soliton ripples.

4.2 Suggested Next Steps

The following is a necessarily incomplete list of suggested next steps in the ongoing treatment of surface scattering. It is convenient to separate the list into Experimental and Theoretical topics, although the two are closely related here. We have:

A. Some Experimental Topics

- (1). Measure directly the rms height and the mean duration of the soliton-ripples, under various near-surface conditions, [14]-[18], including no to full gravity-wave development;
- (2). Mean (back-) scatter intensities under (1), simultaneously, with particular attention to the possible presence of bubbles;
- (3). "Forward" and bistatic scatter generally, also under (1), (2) above;
- (4). Develop acoustic techniques, based on the associated theory here and below (8), for measuring the relevant parameters of the small-scale scatter components.

B. Theoretical Extensions

- (1). Apply results of (1)A above to the analysis developed here;
- (2). Calculate representative (backscatter) cross sections for all scattering angles ($0 \leq \theta_{OT} \leq \pi/2$), and selected surface ripple parameters;
- (3). Apply Bahar's general "full-wave" approach [44] in detail to relate the former to the approximate solution obtained here.
- (4). Determine the doppler spectrum of the composite wave surface in our general model and compare with experiment [6];
- (5). Examine the contributions of higher-order Bragg scatter;
- (6). Develop further, and apply to quantitative estimates, the contributions of the diffraction terms vis-à-vis higher-order approximations in the direct scatter theory;
- (7). Generalization of the results to anisotropic surfaces;
- (8). Examination of various corrections to the Kirchoff or Tangent Plane approaches.

Finally, we stress once more the need for carefully controlled experimentation, where "ground truth" regarding surface phenomena is fully obtained, and where the subtleties of the associated signal processing are both understood and applied [6].

Part II. Analytical Models

5. The Received Scattered Field

Here we present the analytical features of random wave-surface scattering when the incident radiation is acoustic propagation from a directional source. A directional receiver is employed, in the manner of Figure 2.2 above. While much of the present theory is well-known [1], [2], [8], [9], [21], [22], [33], we shall also include here a number of new features and results. Our treatment, however, is intentionally concise: we refer the reader to other references (see Section 1) for many of the details, in the interest of brevity and attention to the main problem at hand, viz., the determination of back- and forward-scatter intensities, along with their attendant assumptions and approximations.

5.1 The Received Scattered Field, I: Formulation

For the total scattered field $\alpha(\underline{R}, t)$ at a point $P(\underline{R}, t)$ in a linear, inhomogeneous, and possibly random medium, or on its boundaries, we can write generally [12], [43], [41], in operator form

$$\boxed{\{\alpha(\underline{R}, t) = \frac{\hat{1}}{\hat{1} - \hat{\eta}_{\infty}} \alpha_H(\underline{R}, t)\}} \quad ; \quad \hat{\eta}_{\infty} = \hat{M}_{\infty} \hat{Q}, \quad (5.1)$$

where $\alpha_H [= \hat{M}_{\infty}(-G_T)]$ is the homogeneous or unscattered field component and the brackets $\{ \}$ denote the ensemble of such (random) media. Here $-G_T$ is the source distribution (which includes the sensor array), and \hat{M}_{∞} is the integral operator whose kernel is the green's function $g(\underline{R}, t | \underline{R}', t')_{\infty}$ for an infinite, unbounded medium (except for source regions), which is also homogeneous (but not necessarily lossless). The operator, $\hat{\eta}_{\infty}$, is the field-renormalization operator, where \hat{Q} , cf. (5.1), embodies the scattering mechanisms appropriate to the physical situation. Here, for example, we have

$$\hat{Q} = \hat{Q}_S + \hat{Q}_V, \quad (5.2)$$

where \hat{Q}_S represents the scattering effects of the air-water boundary, or wave surface, while \hat{Q}_V describes any volume inhomogeneities. The specific

form of \hat{M}_∞ is, of course, determined by the (usually differential) propagation equation for the medium, without inhomogeneities.

Next, we shall make the following assumptions:

- I. The medium supports an (extended) Helmholtz equation of propagation, e.g.,

$$(\nabla^2 - \frac{1}{c_0^2} \frac{\partial^2}{\partial t^2}) \alpha = -G_T, \quad (5.3a)$$

with c_0 = speed of wavefront propagation in the medium.

- II. The medium (except for boundaries, here the surface) is therefore homogeneous

$$\therefore \hat{Q}_V = 0. \quad (5.3b)$$

- III. Only local surface scattering interactions are significant, so that Eq. (5.1) becomes on developing the Perturbation Theoretical Series (PTS) [42]

$$\therefore \alpha = \alpha_H + \sum_{n=1}^{\infty} \hat{\eta}_\infty^{(n)} \alpha_H \doteq \alpha_H + \hat{M}_\infty \hat{Q}_S \alpha_H; \quad (5.3c)$$

and

$$\alpha = \alpha_H + \alpha_I; \therefore \alpha_I = \hat{M}_\infty \hat{Q}_S \alpha_H. \quad (5.3d)$$

The approximation (5.3c), which neglects coupling of the scattered field to the scattering elements (embodied in \hat{Q}_S), e.g., terms $O([\hat{M}_\infty \hat{Q}]^{(2)})$ or higher are dropped, is a form of Born approximation. This appears to be eminently acceptable in practice, since scattering from wave to wave over more than neighboring wave structures is negligible provided, for $c = c_0 + c_1(z)$, that $\nabla c \neq 0$: only "nearest neighbor" wave surfaces will support multiple scatter (diffraction) effects. Consequently, we call (5.3c):

$\alpha \doteq \alpha_H + \hat{M}_\infty \hat{Q}_S \alpha_H$

(5.4)

the field for an "Exact" Wave Surface Theory,* under the conditions (5.3b) [and (5.3a) if we restrict ourselves to (Helmholtz) media] [We shall remove this restriction presently, cf. Sec. 5.3 ff.]

The received scattered field is

$$\boxed{X_I(t) = \hat{R}\alpha_I \doteq \hat{R}\hat{M}_\infty \hat{Q}_S \alpha_H,} \quad \text{with } \alpha_H = \hat{M}_\infty(-G_T), \quad (5.5)$$

where now \hat{R} is the operator for the receiving aperture**, viz.

$$\hat{R} = \int_{V_R} d\eta \int_{Br_1: \substack{\infty i+d(>0) \\ (-\infty i+d)}} A_R(\eta, s) ()_{r(\eta), s} e^{st} \frac{ds}{2\pi i}, \quad \text{Im } s = 2\pi i f, \quad (5.6)$$

where $(\eta, d\eta)$ are vectors and their coördinates, associated with the receiving aperture, in the volume V_R , and A_R is an aperture weighting function.

For the narrow-band signals and far-field (i.e., Fraunhofer) conditions [cf. (2.20)] postulated in our present work, \hat{R} , (5.6), reduces to the much simpler form

$$\hat{R} \Big|_{\substack{\text{f.f.} \\ \text{n.b.}}} \doteq Q_R(-\underline{v}_R - \underline{v}_{OR}; f_0) \int_{Br_1} e^{st} ()_{R, s} \frac{ds}{2\pi i}, \quad (5.7)$$

where

$$\underline{v}_R = \hat{i}_R f_0 / c_0; \quad \underline{v}_{OR} = \hat{i}_{OR} f_0 / c_0 = \text{"steering" wave number.} \quad (5.7a)$$

*We drop the bracket { } notation henceforth, remembering that α is a random process, since \hat{Q}_S is also; α_H , \hat{M}_∞ , of course, are deterministic.

**Here Br_1 is a Bromwich contour $(-\infty i+d, \infty i+d)$: all singularities of the integrand are at $\text{Re}(s) \leq 0$. For steady-state excitations $d = 0$ and the result is the well-known Fourier transform, with $s = 2\pi i f$, $f = (\text{real})$ frequency. For transient excitation, $d < 0$, and one has a Laplace transform.

Here f_0 is the central frequency of the original (narrow-band) signal, and $\hat{\underline{i}}_R, \hat{\underline{i}}_{OR}$ are (inward) unit vectors, with $\hat{\underline{i}}_{OR}$ along the main axis of the (complex) receiving beam, \underline{Q}_R , cf. Fig. 5.1. (We note also that the beam patterns are functions of frequency, generally, Sec. 6.1). For the omni-directional receiver used in the experiments [6], $\underline{Q}_R = \underline{Q}_R(f_0)$, a complex constant, [cf. Eq. (6.14) ff.].

5.2 The Unscattered Field

For the Helmholtz media (obeying (5.3a)) it is well-known that

$$\left. \begin{aligned} \hat{M}_\infty(\underline{R}, t | \underline{R}', t') &= - \int_{-\infty}^{\infty} dt' \int (\)_{\underline{R}', t'} d\underline{R}' g_\infty(\underline{R}, t | \underline{R}', t'); \\ \text{with } g_\infty &= \delta(t - t' - \rho/c_0) / 4\pi\rho, \quad \rho \equiv |\underline{R}' - \underline{R}| \end{aligned} \right\} \quad (5.8)$$

so that the homogeneous, i.e., unscattered field component α_H , (5.5), becomes at once the familiar result [41], [42]

$$\alpha_H(\underline{R}, t) = \int_{V_T} G_T(t - \rho/c_0, \underline{R}') \frac{d\underline{R}'}{4\pi\rho}, \quad G_T \in V_T, \quad (5.9)$$

where V_T is the source domain and \underline{R} lies outside V_T . In the far-field we get in straightforward fashion [34] for narrow-band signals:

$$\alpha_H(\underline{R}, t) \Big|_{\substack{\text{f.f.} \\ \text{n.b.}}} \doteq \frac{A_0}{4\pi R} \int_{Br_1} \underline{Q}_T'([\hat{\underline{i}}_T - \hat{\underline{i}}_{OT}] s_0 / 2\pi i, s_0 | S_{in}(s)) e^{s(t - \hat{\underline{i}}_T \cdot \underline{R} / c_0)} \frac{ds}{2\pi i} \quad (5.10)$$

$$(\hat{\underline{i}}_T = \underline{R} / |\underline{R}|; \therefore \hat{\underline{i}}_T \cdot \underline{R} = R) \quad (5.10a)$$

where now \underline{Q}_T' is the generalized beam pattern [12] (with $\underline{R}' \rightarrow \underline{\xi}$ ff.)

$$\underline{Q}_T' = \int_{V_T} A_T(\underline{\xi}, s_0) S_{in}(s | \underline{\xi}) e^{s_0(\hat{\underline{i}}_T - \hat{\underline{i}}_{OT}) \cdot \underline{\xi} / c_0} d\underline{\xi}, \quad (s_0 = 2\pi i f_0), \quad (5.11)$$

in which $\hat{\underline{i}}_{OT}$ is a "steering" (unit) vector, cf. (5.7a). Here

$$\hat{S}_{in}(s | \underline{\xi}) = A_0 S_{in}(s | \underline{\xi}) = A_0 \hat{\Xi}_t\{\underline{s}(t | \underline{\xi})\} \quad (5.12)$$

is the amplitude spectrum of the (here narrow-band) signal $S_{in}(t) = A_0 s(t)$; ($\int_{-\infty}^{\infty} e^{-st} dt$, $\text{Re}(s) > 0$). The quantity A_0 is the (peak) amplitude of $S_{in}(t)$, e.g. $\langle S_{in}^2 \rangle = \frac{A_0^2}{2} \langle s^2 \rangle$, $\langle s^2 \rangle = 1$, where $\langle \rangle \equiv$ time average (as $T \rightarrow \infty$), or over the finite interval ($t_0, t_0 + T < \infty$) if $S_{in}(t)$ is of finite duration.

Like A_R , (5.6), A_T is the aperture weighting associated with the transmitter, at each element $d\xi$ where the signal is applied. In the general case different signals may be applied at different locations (ξ) on the aperture: hence, $\hat{S}_{in} = A_0 S_{in}(s|\xi)$, cf. (5.12). However, we shall assume with little loss of generality that the same signal drives each element, so that $S_{in}(s|\xi) = S_{in}(s)$. Then (5.11) reduces to

$$Q_T = S_{in}(s) \int_{V_T} A_T(\xi, s_0) e^{s_0(\hat{i}_T - \hat{i}_{0T}) \cdot \xi / c_0} d\xi \quad (5.13a)$$

$$= S_{in}(s) Q_T(\underline{v}_T - \underline{v}_{0T}; f_0), \quad (\underline{v}_T = \hat{i}_T f_0 / c_0, \text{ etc.}) \quad (5.13b)$$

where now Q_T is the (complex) beam pattern of the transmitting aperture, in these far-field situations.* Applying (5.13) to (5.10) then allows us to write for the (as yet) unscattered field the not unexpected result

$$\alpha_H(\underline{R}, t) \Big|_{\substack{\text{f.f.} \\ \text{n.b.}}} = \frac{A_0 Q_T}{4\pi R} \int_{Br_1} S_{in}(s) e^{s(t-R/c_0)} \frac{ds}{2\pi i}, \quad (5.14)$$

subject to the uniform drive condition $S_{in}(s|\xi) = S_{in}(s)$, with Q_T given by (5.13b) as defined in (5.13a).

5.3 Absorption and Doppler

Although so far we have assumed that the medium of propagation is lossless, in reality there is some attenuation, mainly because of molecular absorption at the frequencies employed here (<40 kHz). In general,

*In the "near-field" or Fresnel regions the "beam pattern" becomes range-dependent, as a consequence of the quadratic terms in the expansion of $\rho = |\underline{R} - \underline{\xi}|$, ($\underline{R}' \rightarrow \underline{\xi}$). To avoid this, a useful far-field condition is $\pi L_{\max}^2 / \lambda_0 \ll R$, where L_{\max} is the largest dimension of the aperture and $\lambda_0 (= c_0 / f_0)$ is the wavelength of the (central) frequency of the postulated narrow-band signals.

absorption affects the beam patterns and waveforms. But with narrow-band excitations the general relations simplify greatly, reducing to a simple attenuation factor.

To see this we use the transform $Y_{0,\infty} = \mathfrak{F}_t\{g_\infty\}$ of the green's function solution to the basic propagation equation for relaxation absorption [42], viz.

$$[(1 + \tau_{ox} \frac{\partial}{\partial t}) \nabla^2 - \frac{1}{c_0^2} \frac{\partial^2}{\partial t^2}] g_\infty = -\delta_{tt'} \delta_{RR'} \quad (5.15)$$

so that Y_0 obeys

$$[(1 + \tau_{ox} s) \nabla^2 - s^2/c_0^2] Y'_{0,\infty} = \delta_{RR'} ; \quad Y_0(R, s | R', t')_\infty = Y'_0(R, s | R')_\infty e^{-st'} \quad (5.15a)$$

For this it is readily found ([41], I) that

$$Y_{0,\infty} = \frac{e^{-\frac{\rho s}{c_0}(1+\tau_{ox}s)^{-1/2}-st'}}{4\pi\rho \sqrt{1+\tau_{ox}s}} \quad , \quad \tau_{ox} = \alpha_x/c_0^2 \quad (5.16)$$

For typical oceans the relaxation time τ_{ox} of the medium is $\tau_{ox} \doteq \tau_{MgSO_4} = O(10^{-6} \text{ secs})$, so that for weak absorption, e.g., $(\tau_{ox}|s|)^2 \ll 1$, f_{\max} ($= |s|/2\pi$) is $O(40 \text{ kHz})$. For frequencies less than $O(40 \text{ kHz})$ the medium is essentially purely absorptive and nondispersive. In fact, we can re-write (5.16) as

$$Y_{0,\infty} = \frac{e^{-\frac{\rho s}{c_0} - st'}}{4\pi\rho} \left[\frac{e^{\{1-(1-\tau_{ox}s)^{-1/2}\}\rho s/c_0}}{\sqrt{1+\tau_{ox}s}} \right] \quad (5.17a)$$

$$\doteq (Y_{0,\infty})_{\text{Helmholtz}} \cdot \left[e^{(\tau_{ox}/2c_0)\rho s^2} \right] + (Y_{0,\infty})_{\text{Helm}} e^{-\omega_0^2 \rho \tau_{ox}/2c_0} \quad (5.17b)$$

since for narrow band signals $s \rightarrow 2\pi i f_0$, where $\mathfrak{F}_T\{g_\infty = \text{Eq. (5.8)}\}$ gives $(Y_{0,\infty})_{\text{Helm}}$, the first factor of (5.17a). For $f_0 = 20 \text{ kHz}$, $\sqrt{1+\tau_{ox}|s|} = 1.06 \doteq 1$, and for $f_0 = 40 \text{ kHz}$, $\sqrt{1+\tau_{ox}|s|} = 1.12 \doteq 1$, also: the s-dependent denominator is effectively unity. Accordingly, for narrow-band signals

and positions in the far-field of the source we simply scale the signal amplitude A_0 by the factor $\exp(-a\omega_0^2 R)$, viz.

$$\boxed{A_0 \rightarrow A_0 e^{-a\omega_0^2 R}}, \quad a \equiv \tau_{0X}/2c_0 = O(3.7 \cdot 10^{-10} \text{ sec}^2/\text{meter}). \quad (5.18)$$

Equation (5.18) shows the well-known result of attenuation exponentially dependent on distance and on the square of the frequency for media where relaxation absorption governs propagation, in the manner of Eq. (5.15) above.

The effects of doppler are, however, more complex than the ("low-frequency") attenuation. Doppler produces a frequency modulation of the original signal. The principal mechanisms for this in underwater studies are platform movement and the motion of the ocean wave-surface. As long as the doppler velocities are comparatively small [e.g., $v/c_0 \leq 0.10$, say], a practical theory is possible, cf. [34]. In our present study, cf. Fig. 2.2, both the transmitting and receiving platforms are effectively stationary in space, so that only the wave motion modulates the incident radiation in the course of scattering. The effect of this is to introduce a time-delay Δt_{dS} , in the time-variable quantities which appear in the expressions for the received, scattered field, as noted below in Eqs. 5.22. This time delay is a function of a time-variable position, dependent on the moving wave surface.

5.4 The Received Scattered Field, II: Canonical Forms and Geometry

Before we go on to consider explicit wave-surface models, which will dictate the specific nature of our attack on the problem [cf. Sec. 6 ff.], let us obtain a canonical series development for the received, surface-scattered field represented here by (5.5).

This is done by observing that the field renormalization operator, $\hat{\eta}_\infty (= \hat{M}_\infty \hat{Q}_S)$, cf. (5.1), can be expanded in some suitable hierarchy of (linear) operators of increasing complexity, as represented by the sum

$$\hat{\eta}_\infty = \sum_{\ell=0}^{\infty} a_\ell \hat{\eta}_\infty^{[\ell]} \quad (5.19)$$

since the scattering process is linear. The quantity a_ℓ is an expansion coefficient, whose specific form is determined jointly by the physical nature of the scattering surface and by the particular method with which a specific expansion is to be carried out.

For example, in the usual perturbation technique (Perturbation Method \equiv P.M.) here, the boundary, e.g., scattering surface Σ , is perturbed or expanded with respect to some appropriate reference surface S [4]. In recent treatments [33], [4] where a two-scale wave surface is postulated, the reference surface is chosen to be the large-scale, or gravity-wave component. The perturbation is then embodied in the expansion of \hat{M}_∞ in $\hat{\eta}_\infty$, where \hat{M}_∞ is defined on Σ and expanded on S , cf. Sec. I of [4], while \hat{Q}_S is likewise defined now* on S . Thus, (5.19) becomes

$$\hat{\eta}_\infty = \sum_{\ell=0}^{\infty} a_\ell \hat{M}_\infty^{[\ell]} \hat{Q}_S. \quad (5.19a)$$

The expansion coefficients, a_ℓ , become now $a_\ell = a^\ell = (k_0 \sigma_\zeta)^\ell$, with the condition $k_0 \sigma_\zeta \ll 1$, $\sigma_\zeta^2 \equiv \langle \zeta^2 \rangle$, which is required for practical convergence of series like (5.19). In addition, the radii of curvature of the small-scale surface component must be large compared to $|\zeta_c|$, the magnitude of the elevations of the small-scale surface component on S , so that the expansion (of \hat{M}_∞) is unique. This is equivalent to requiring that the slopes of ζ_c be small, also, a condition, however, not generally met here [cf. Remarks, Sec. 1].

Accordingly, we employ an alternate method of expansion, based on the structure of the (local) surface scatter operator \hat{Q}_S (on Σ), rather than on the expanded projection of the (non-local) integral operator \hat{M}_∞ on S . The expansion coefficients, a_ℓ , are now based on certain statistics of the numbers of different orders of (multiple) scattering interactions. This type of expansion turns out to be essentially independent of both local elevation and slope conditions, cf. above. Instead of (5.19a) we have

*In a one-scale wave surface, $S = S_0 = \langle \zeta \rangle = 0$: the reference surface is the equilibrium (\equiv mean) wave surface.

$$\hat{\eta}_{\infty} = \sum_{\ell=0}^{\infty} b_{\ell} \hat{M}_{\infty} \hat{Q}_S^{[\ell]}, \text{ or } \hat{Q}_S = \sum_{\ell=0}^{\infty} b_{\ell} \hat{Q}_S^{[\ell]} \quad (5.19b)$$

The kernels, or weightings, of these surface scatter operators $\hat{Q}_S^{[\ell]}$ are given by $\hat{Q}_S^{[\ell]}(\underline{r}', t')$, where $\underline{r}' \in \Sigma$, the (composite) wave surface and t' is a doppler-delayed epoch. As we shall see presently, cf. Sec. 7, the lower orders ($\ell=0,1$) generally represent direct scattering components here, while the higher orders ($\ell \geq 2$) embody the multiple-scatter, or diffraction contributions.

The integral operator \hat{M}_{∞} , cf. (5.8), applied to \hat{Q}_S , which is itself applied to α_H (5.14) on the actual wave surface, Σ , in the same way α_H was obtained, gives us in the far-field of the surface, the scattered field α_I . This becomes with the help of (5.7) in (5.5) the following general (complex) result:

$$\alpha_I(t) = \sum_{\ell=0}^{\infty} \chi^{(\ell)}(t), \quad (5.20)$$

where, canonically, we find that, along with (5.18) for absorption,

$$\chi^{(\ell)}(t) \Big|_{\substack{\text{f.f.} \\ \text{n.b.}}} = A_0 \int_{Br_1} S_{in}(\frac{s}{2\pi i}) F_S^{(\ell)}(s | \underline{z}(\underline{r}, t), \underline{R}_T, \underline{R}_R, \dots | f_0) e^{st} \frac{ds}{2\pi i}, \quad (5.21a)$$

and

$$F_S^{(\ell)} = \int_{S_0} Q_R(-\underline{v}_R - \underline{v}_{OR}; f_0) Q_T(\underline{v}_T - \underline{v}_{OT}; f_0) Q_S^{(\ell)}(\underline{r}', t') \cdot e^{-sT_0 - s(\hat{i}_T - \hat{i}_R) \cdot \underline{r}' / c_0} e^{-a\omega_0^2 (|\underline{R}_T + \underline{z}| + |\underline{R}_R + \underline{z}|)} \frac{dS_0}{(4\pi)^2 R_T R_R n_z} \quad (5.21b)$$

where (\underline{r}', t') are coördinates associated with the wave surface Σ . (Here $F_S^{(\ell)}$ is a degenerate form of what we call the Total Surface Spreading Function (TSSF) $F_S^{(\ell)}(s', s-s' | \underline{z})$, where we regard the moving wave surface as a time-variable filter. The slow (temporal) variations of the surface (elevation) \underline{z} vis-à-vis the acoustic signal permit

this "parametric" form of the TSSF where now ζ is explicitly time-variable, as are all factors which contain ζ and its various spatial derivatives. The geometry of the general (far-field) source-surface-receiver configuration is shown in Fig. 5.1.

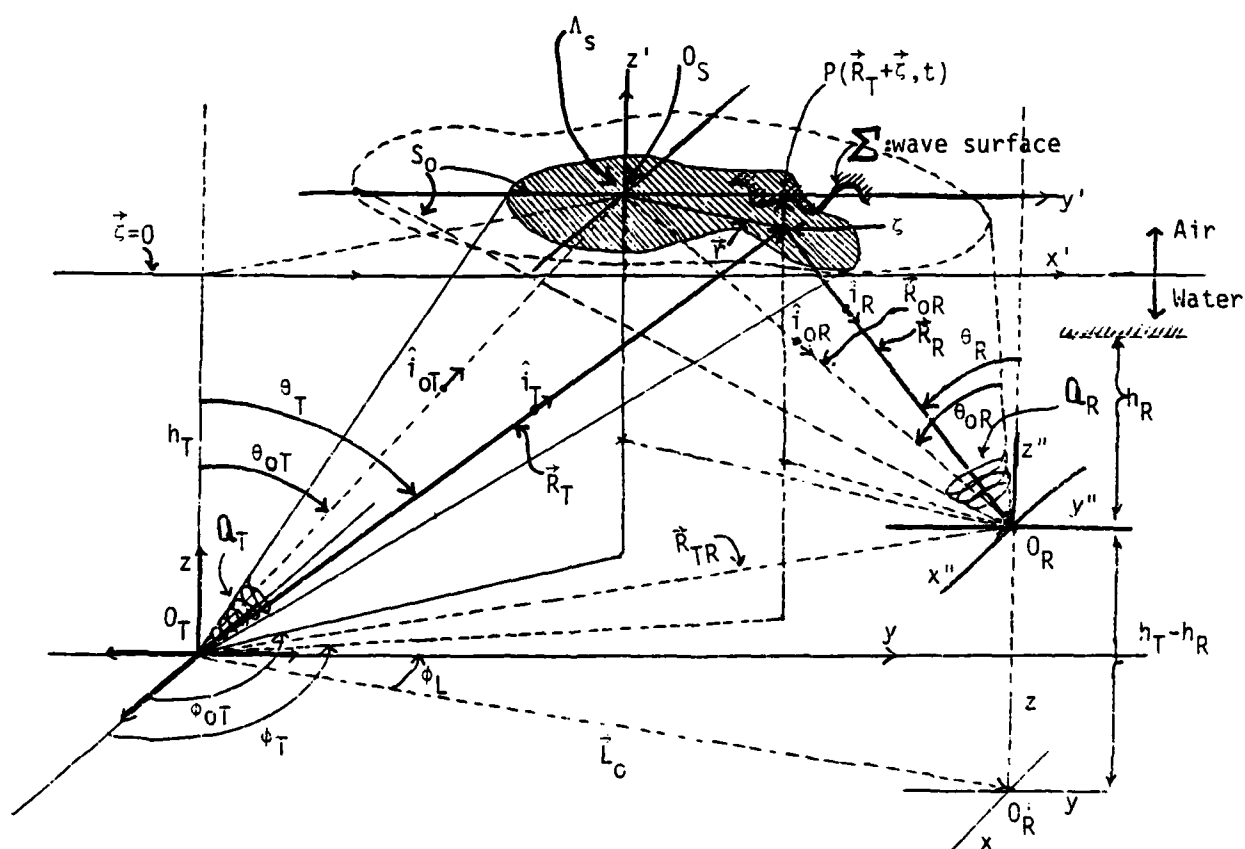


Figure 5.1: Geometry of the transmitter ($@ O_T$), wave-surface (Σ), receiver (at O_R), showing surface elevation ζ above $\zeta = 0$: S_0 , and the common region of illumination (shaded), on S_0 due to overlapping beam patterns Q_T, Q_R ; (here $\nabla c = 0$).

The various elements of (5.21) are described below. We have

$$\Lambda_S = \text{effective "illuminated" surface area, by joint beam projection in } S_0, \text{ cf. Sec. 6.3, Fig. 6.1 ff.} \quad (5.22)$$

$$dS_0 = d\underline{r} = dx'dy' = dxdy \text{ on } S_0: \underline{\zeta} = 0; \text{ with } d\Sigma = dS_0/n_z; \quad (5.22a)$$

$$\underline{r}' = \underline{r} + \underline{\zeta}, \text{ where } \underline{r}' \text{ is always on the wave surface, } \Sigma; \quad (5.22b)$$

$$\underline{r} = \hat{i}_x x + \hat{i}_y y; [(x', y')\text{-system is simply a translation of the } (x, y)\text{-system}] \quad (5.22c)$$

$$T_0 = (R_{OT} + R_{OR})/c_0: \text{ time-delay from } O_T \rightarrow O_S \rightarrow O_R; \quad (5.22d)$$

$$\hat{i}_{OT}, \hat{i}_{OR} \equiv \underline{R}_{OT,OR}/|\underline{R}_{OT,OR}|: \text{ unit vectors;} \quad (5.22e)$$

$$\hat{i}_T, \hat{i}_R \equiv \underline{R}_{T,R}/|\underline{R}_{T,R}|: \text{ unit vectors, to projection of scattering point on } \Sigma \text{ upon } S_0; \quad (5.22f)$$

$$R_T, R_R, R_{OT}, \dots = |\underline{R}_T|, |\underline{R}_R|, \text{ etc., distances;} \quad (5.22g)$$

$$t' = t - \Delta t_{dS} = \text{doppler-shifted epoch; } (\underline{r}', t') \text{ are on the wave surface } \Sigma; \quad (5.22h)$$

$$\Delta t_{dS} = \hat{i}_T \cdot \underline{r}'(\underline{r}, t) = \hat{i}_T \cdot \{\underline{r} + \underline{\zeta}(\underline{r}, t - R_R/c_0)\}: R_R = R_{OR} - \hat{i}_{OR} \cdot \underline{r}; \quad (5.22i)$$

$$\underline{\zeta}(\underline{r}, t) = (\text{vector) elevation of the wave surface, vs. } \underline{\zeta} = 0, \text{ the plane } S_0; \quad (5.22j)$$

$$a = \tau_0/2c_0 = \text{absorption coefficient (sec}^{-2}/\text{meter), cf. (5.18);}$$

$$n_z = (1 + \zeta_x^2 + \zeta_y^2)^{-1/2}; \quad \zeta_x, \zeta_y = \frac{\partial \zeta}{\partial x}, \frac{\partial \zeta}{\partial y}: \text{ surface slopes} \quad (5.23a)$$

$$\hat{n} = (\text{outward) normal to surface } \Sigma, = (\hat{i}_x \zeta_x + \hat{i}_y \zeta_y - \hat{i}_z) n_z; \quad (5.23b)$$

(inward normal = $-\hat{i}_z$)

$$\underline{v}_{OT}, \underline{v}_{OR} = \text{beam-steering wave numbers, cf. (5.13b), (5.7a);} \quad (5.23c)$$

$$\underline{R}_{TR} = \underline{\vec{r}}_O + \hat{i}_z(h_T - h_R), \text{ cf. Fig. 5.1; vector distance between } O_T \text{ and } O_R. \quad (5.23d)$$

From Fig. 5.1, it is readily shown that the unit vectors \hat{i}_T, \hat{i}_R become for these bistatic configurations

$$\hat{\mathbf{i}}_T|_{S_0} = \underline{R}_T/|\underline{R}_T| = \hat{\mathbf{i}}_x \cos\phi_T \sin\theta_T + \hat{\mathbf{i}}_y \sin\phi_T \sin\theta_T + \hat{\mathbf{i}}_z \cos\theta_T \quad (5.24a)$$

$$\hat{\mathbf{i}}_R|_{S_0} = \underline{R}_R/|\underline{R}_R| = -(\hat{\mathbf{i}}_x R_T \cos\phi_T \sin\theta_T + \hat{\mathbf{i}}_y (R_T \sin\phi_T \sin\theta_T - L_0) + \hat{\mathbf{i}}_z h_R)/R_R, \quad (5.24b)$$

where

$$R_R = (R_T^2 \sin^2\theta_T + L_0^2 - 2R_T L_0 \sin\phi_T \sin\theta_T + h_R^2)^{1/2}, \text{ and} \quad \left. \begin{array}{l} \\ \phi(o)_T = \phi(o)_R - \pi/2. \end{array} \right\} \quad (5.24c)$$

[For $\hat{\mathbf{i}}_{oT}, \hat{\mathbf{i}}_{oR}$ we simply replace R_T by R_{oT} , $\phi_T \rightarrow \phi_{oT}$, etc. in (5.24).] We also find it convenient to write

$$\begin{aligned} 2\alpha \equiv \hat{\mathbf{i}}_T - \hat{\mathbf{i}}_R &= \hat{\mathbf{i}}_x (1 + R_T/R_R) \cos\phi_T \sin\theta_T \\ &+ \hat{\mathbf{i}}_y \{(1 + R_T/R_R) \sin\phi_T \sin\theta_T - L_0/R_R\} \\ &+ \hat{\mathbf{i}}_z (\cos\theta_T + \cos\theta_R), \end{aligned} \quad (5.25)$$

cf. the exponent in (5.21b). [Again, for the reference vectors $\hat{\mathbf{i}}_{oT}, \hat{\mathbf{i}}_{oR}$, \underline{R}_{oT} , etc., we set $R_T \rightarrow R_{oT}$, $\phi_T \rightarrow \phi_{oT}$, etc. in (5.25), to get $2\alpha_o \equiv \hat{\mathbf{i}}_{oT} - \hat{\mathbf{i}}_{oR}$, cf. (5.27) et seq. below.]

A critically important simplification of our canonical results (5.20), (5.21) results from the ability to employ "narrow beams" (N.B.), e.g., beams narrow enough so that the mutually "illuminated" surface $\Sigma (= S_0)$ (i.e., the shaded region in Fig. 5.1, for example) is sufficiently small that the spatial geometry ($\sim R_T, R_R$, etc.) for source and receiver change little over the "illuminated" surface region ($\sim S_0$). Thus, we can replace \underline{R}_T by \underline{R}_{oT} , θ_T by θ_{oT} , etc., and most important, note that the angle-dependent quantities in $F_S^{(k)}$, (5.21b), can also be replaced by the (constant) reference quantities θ_{oT}, ϕ_{oT} , etc. This results in a "factoring" of the beam patterns, in that they now will depend only on their projections on the surface about O_S , and not on the coordinates of the wave surface away from O_S . [For details, see Section 6 ff.]

Accordingly, we have $\hat{i}_T \rightarrow \hat{i}_{OT}$, etc., so that the TSSF (5.21b) can now be expressed in the ultimately much more usable form (where the results of Sec. 6.2 are included):

$$F_S^{(\ell)} \Big|_{\substack{\text{n.b.} \\ \text{f.f.} \\ \text{N.B.}}} = \int_{S_0} \frac{dxdy}{(4\pi)^2 R_{OT} R_{OR} n_z} Q_R(-\hat{i}_R f_0/c_0 - \underline{v}_{OR}; f_0) Q_T(\hat{i}_T f_0/c_0 - \underline{v}_{OT}; f_0) \cdot Q_S^{(\ell)}(\underline{r}', t') e^{-a\omega^2 c_0 T_0 - (s/c_0)[(\underline{r}+\underline{z}) \cdot 2\underline{\alpha}_0 + T_0 c_0]} \quad (5.26)$$

where $\underline{z} = \underline{z}(\underline{r}, t')$ is a slowly-varying function of time, vis-à-vis the signal in $X^{(\ell)}(t)$, cf. (5.21a) and remarks ff. Eq. (5.21b).

Important special geometries of operation are:

I. Monostatic Operation: R @ T: ($L_0 = 0$; $\theta_{OR} \rightarrow \theta_{OT}$, $\phi_{OR} = \frac{\pi}{2} + \phi_{OT}$; $\hat{i}_{OR} = -\hat{i}_{OT}$;
 $R_R = R_T$; $(R_{OR} = R_{OT})$; $h_R = h_T$)

$$2\alpha_{ox} = 2 \cos\phi_{OT} \sin\theta_{OT}; \quad 2\alpha_{oy} = 2 \sin\phi_{OT} \sin\theta_{OT}; \quad 2\alpha_{oz} = 2 \cos\theta_{OT}, \quad (5.27)$$

with associated quantities of subsequent interest (cf. (7.28)):

$$\left. \begin{aligned} 2(\alpha_{ox}^2 + \alpha_{oy}^2 + \alpha_{oz}^2)/\alpha_{oz} &= 2/\cos\theta_{OT}; \\ (\hat{n}/n_z) \cdot 2\underline{\alpha}_0 &= 2(\zeta_x \cos\phi_{OT} \sin\theta_{OT} + \zeta_y \sin\phi_{OT} \sin\theta_{OT} - \cos\theta_{OT}); \\ \text{Specular: } \theta_{OT} = 0: \quad \therefore 2\alpha_{ox} = 2\alpha_{oy} = 0; \quad 2\alpha_{oz} &= 2. \end{aligned} \right\} \quad (5.28)$$

II. Bistatic Operation ($R \neq T$): ($L_0 \neq 0$; Eqs. (5.24), (5.25), $R_T \rightarrow R_{OT}$,
etc., generally) (5.29)

III. Bistatic Operation at Snell (or Specular) Angles: $L_0 \neq 0$

$$\left. \begin{aligned} L_0 = (R_{OT} + R_{OR}) \sin\theta_{OT} \text{ insures } (\hat{i}_{OR})_y &= (\hat{i}_{OT})_y \\ \phi_{OT} = \phi_{OR} - \pi/2 = \pi/2 \text{ insures } (\hat{i}_{OR})_x &= (\hat{i}_{OT})_x \\ \theta_{OR} = \theta_{OT} \text{ insures } (\hat{i}_{OR})_z &= -(\hat{i}_{OT})_z: \text{ Snell in plane} \end{aligned} \right\} \text{ coplanar } \quad (5.29a)$$

Then we have

$$\left. \begin{aligned} 2\alpha_{oz} &= 2 \cos\theta_{OT} \\ 2(\alpha_{ox}^2 + \alpha_{oy}^2 + \alpha_{oz}^2)/\alpha_{oz} &= 2 \cos\theta_{OT} \\ (\hat{n}/n_z) \cdot \underline{\alpha}_0 &= \zeta_y [(1 + R_{OT}/R_{OR})\sin\theta_{OT} - L_0/R_{OR}] - 2 \cos\theta_{OT} = -2 \cos\theta_{OT}, \end{aligned} \right\} (5.30)$$

this last from (5.29). [These results, cf. (5.28), (5.30), agree, as expected with Eqs. (6.25) et seq. of Tolstoy and Clay [9], who use a geometry with O_S , Fig. 5.1, as the primary reference system.]

5.5 Discussion and Critique

At this stage we have carried the analysis for the received scattered field, $X(t)$, to the point where the central physical problem is to determine the analytic structure of the surface-scatter kernels, $Q_S^{(\ell)}$, on the surface Σ . The approximations and assumptions governing (5.26) in (5.21a) so far, are:

- | | | |
|--|---|--|
| (i). <u>narrow-band signals</u> | } | these permit us to separate the signal components from the wave surface velocity $\dot{\zeta}$: the total surface spreading function $F_S^{(\ell)}(s', s-s')$ is $\sim \delta(s-s')$, to yield $F_S^{(\ell)}(s, t ..)$ in (5.21a), (5.26) |
| (ii). <u>Snell doppler</u> | | |
| (iii). <u>far-field conditions</u> | | $\pi L_{\max} \ell_{\max} / \lambda_0 \ll R_{OT}, R_{OR}$, where $\ell_{\max} = \max$ (rms) correlation distance of the (illuminated) wave surface; L_{\max} = maximum dimension of the transmitter (receiver) aperture. This permits us to define beam patterns, which are independent of range. |
| (iv). <u>small surface displacements</u> | | vis-à-vis R_{OT}, R_{OR} : (part of (iii), really) |
| (v). <u>"narrow beams," (N.B.)</u> | | $\Delta S_0 \ll R_{OT}^2, R_{OR}^2$; beam patterns are independent of angle variations and can be referred to a single point (O_S) on the "illuminated" wave surface. [If the "narrow-beam" condition is |

- not satisfied, (5.21b) is to be used in place of (5.26).]
- (vi). $\nabla c = 0$: $c(z) = c_0$, a constant: no velocity gradients in the volume;
 - (vii). $\hat{Q}_V = 0$: no volume inhomogeneities, random or deterministic, cf. Eq. (5.3b);
 - (viii). Only local surface scatter interactions: the scattered field does not couple to the scattering elements, cf. (5.3c,d) et seq.
 - (ix). $\hat{M}_\Sigma \rightarrow \hat{M}_\infty$: the scattering surface is sufficiently removed not to affect the pressure distribution over the aperture of the driving signal source, cf. (5.1). (This condition is always obeyed in practice unless the boundary is very close to the aperture and the source level is very high [41, I]).
 - (x). A non-dispersive, lossy medium is assumed, so that the Helmholtz equation (5.3a) for the propagating field is obeyed, with only a frequency and range-dependent attenuation factor applied to the emitted signal amplitude, A_0 , cf. (5.18), in conjunction with (i) above. For practical oceans this requires $f_0 \leq 0(40 \text{ kHz})$.
 - (xi). Slowly moving surfaces vis-à-vis c_0 and the time-scale of the injected signal. This permits us to treat the time-variability of $\zeta(\underline{r}, t')$ parametrically in (5.21) and subsequently.

So far, no boundary conditions, and therefore, boundary approximations, have been explicitly invoked. These, for the moment, are implicit in the surface-scatter kernels, $Q_S^{(\ell)}$, including such important factors as reflection coefficients and shadowing functions. We shall consider the $Q_S^{(\ell)}$ specifically in Section 7. Of the approximations and assumptions used to obtain the basic (total) surface spreading function $F_S^{(\ell)}$, (5.26), the most critical are (i), (iii), (v), (x). The others are normally well-satisfied physically. An important exception could be (vii), $\hat{Q}_V = 0$: this

implies that bubbles, and particularly bubble layers near the surface are negligible in their effects on the surface scatter process. Certainly, in some cases, notably when there is a great deal of wave-breaking activity, bubbles become important. But in many others they appear to be "invisible." (This point is discussed concisely in Section 1 earlier.) In our present treatment we shall exclude bubbles, accordingly.

Finally, our present formulation so far contains several generalizations over earlier treatments. These are:

- (1). time-variable wave-surfaces, ζ , with doppler delays, cf. (5.22i);
- (2). general (narrow-band) signals;
- (3). steered (complex) beams;
- (4). a canonical scattering structure (kernel) which can be developed to include a variety of approximation procedures, including diffraction effects, for different classes of wave surface.

This latter is considered explicitly in Section 7 ff. The specific time-variability of the surface elevation, ζ , is critically important. It quite naturally provides the expected "tilting" effect in our subsequent two-scale theory, whereby the small-scale surface is "modulated" by the large-scale or gravity-wave component, without recourse to the ad hoc mechanisms used in previous analyses [Sec. II of [4] and Sec. III of [29], for example.]

6. Beam Patterns and Apertures

The aperture structure [cf. A_T , A_R , (5.11), (5.6) above] and the associated beam patterns play a critical rôle in the practical application of the theory. We must, therefore, examine their effects in specific detail. Accordingly, for our beam patterns in (5.26) we shall begin by observing that, in our postulated far-field "narrow-beam" (N.B.) operation [(iii), (v), (5.31)], we can write*

$$\nu_T - \nu_{OT} \doteq (\underline{r} \cdot \hat{\underline{a}}_{OT}) f_0 / c_0 R_{OT} ; \quad -\nu_R - \nu'_{OR} = (\underline{r} - \underline{r}_0) \cdot \hat{\underline{a}}_{OR} f_0 / c_0 R'_{OR} \quad (6.1)$$

*These results are achieved by noting that $\hat{\underline{i}}_T = (\underline{R}_{OT} + \underline{r}) / |\underline{R}_{OT} + \underline{r}| \doteq \hat{\underline{i}}_{OT} + \underline{r} \cdot (\hat{\underline{i}} - \hat{\underline{i}}_{OT} \hat{\underline{i}}_{OT}) / R_{OT}$, etc., in the far-field.

where \underline{r}_0 is the vector distance (on S_0) of the point of intersection of R'_{OR} from O_S (for R_{OT}). When the main axes of the T- and R-beams coincide at O_S , then $\underline{r}_0 = 0$ (and $R'_{OR} = R_{OR}$), and the beams are said to "overlap at maximum gain." (It is assumed that the beam-maxima lie along $\hat{\underline{i}}_{OT}$, $\hat{\underline{i}}_{OR}$.) Here $\hat{\underline{a}}_{OT}$, $\hat{\underline{a}}_{OR}$ are dyadics (= second-rank tensors), specifically

$$\hat{\underline{a}}_{OT} \equiv \hat{\underline{I}} - \hat{\underline{i}}_{OT}\hat{\underline{i}}_{OT}; \quad \hat{\underline{a}}_{OR} \equiv \hat{\underline{I}} - \hat{\underline{i}}_{OR}\hat{\underline{i}}_{OR}, \quad (6.1a)$$

in which $\hat{\underline{I}}$ is the unit dyadic [δ_{ij}], ($i, j = 1, 2, 3$). The $\hat{\underline{a}}_{OT}$, $\hat{\underline{a}}_{OR}$ are also called the Fresnel dyadics for $\hat{\underline{i}}_{OT}$, $\hat{\underline{i}}_{OR}$, respectively. The conditions for (6.1) are

$$|\underline{r}|_{\max}/R_{OT} \ll 1; \quad |\underline{\Delta r} = \underline{r} - \underline{r}_0|/R_{OR} \ll 1. \quad (6.2)$$

To obtain the elements of $\hat{\underline{a}}_{OT}$, $\hat{\underline{a}}_{OR}$, we use (5.24) with $\phi_T \rightarrow \phi_{OT}$, $\phi_R \rightarrow \phi_{OR}$, $R_T \rightarrow R_{OT}$, etc. therein. We call (6.2) the "narrow-beam" (N.B.) conditions, as we shall see in Sec. 6.3 ff.

6.1 Beam Patterns and Projections

We select as a convenient and reasonable beam pattern structure the so-called (general) gaussian beam pattern (see (6.5) below):

$$Q(\underline{v}) \equiv g e^{-\frac{1}{2}\underline{v} \cdot (2\pi)^2 \hat{\underline{A}} \cdot \underline{v} + i\phi_T}, \quad (6.3)$$

where g = beam gain (> 0) and $\hat{\underline{A}}$ is the associated aperture dyadic

$$\hat{\underline{A}} = A \begin{bmatrix} 1 & a_{xy} & a_{xz} \\ a_{xy} & a^2 & a_{yz} \\ a_{xz} & a_{yz} & b^2 \end{bmatrix} \equiv A\hat{\underline{a}}, \quad |\det \hat{\underline{a}}| \neq 0; \quad A > 0, \quad (6.4)$$

and where ϕ_T is a constant phase here, for the moment. Since $\underline{v} = \underline{O}(L)$, A is $O(L^2)$ and is thus a measure of the physical area of an equivalent planar aperture; (the actual aperture may, of course, be three-dimensional). The "beam" $Q(\underline{v})$ described by (6.3) is not necessarily N.B.

When the beam patterns fall on the reference surface S_0 of the wave surface Σ , cf. Fig. 5.1, the wave number arguments of (6.3) become

those given in (6.1) for these now far-field situations and N.B. conditions. Accordingly, we have

$$\left. \begin{aligned} Q_T(\underline{r}_T - \underline{r}_{OT}; f_0) &\doteq g_T(f_0) e^{-\frac{1}{2}k_0^2 [A_T/R_{OT}^2] (\underline{r}_T \cdot \hat{A}_{OT} \cdot \underline{r}_T) + i\phi_T(f_0)} ; \\ \hat{A}_{OT} &\equiv \hat{a}_{OT} \cdot \hat{a}_T \cdot \hat{a}_{OT} \\ k_0 &= \omega_0/c_0 \\ |\underline{r}|_{\max}/R_{OT} &\ll 1 \end{aligned} \right\} (6.5)$$

and

$$\left. \begin{aligned} Q_R(-\underline{r}_R - \underline{r}_{OR}'; f_0) &\doteq g_R(f_0) e^{-\frac{1}{2}k_0^2 [A_R/R_{OR'}^2] (\underline{r} - \underline{r}_0) \cdot \hat{A}_{OR'} \cdot (\underline{r} - \underline{r}_0) + i\phi_R(f_0)} \\ \hat{A}_{OR'} &= \hat{a}_{OR'} \cdot \hat{a}_R \cdot \hat{a}_{OR'} \\ |\underline{r} - \underline{r}_0|_{\max}/R_{OR'} &\ll 1 \end{aligned} \right\} (6.6)$$

where $\hat{a}_T A_T \equiv \hat{A}_T$, $\hat{a}_R A_R \equiv \hat{A}_R$ have the generic form (6.4).

We shall confine our attention here to elliptical or circular (conical) beams. Then, all the off-diagonal elements of \hat{a} in (6.4) vanish, and $a \neq b$ for elliptical cones and $a = b$ for cones with circular cross-sections.* Thus, we write

*In fact, \hat{a} in (6.4) represents an ellipsoid in the volume, any plane section of which is an ellipsoid. Setting the off-diagonal elements of \hat{a} equal to zero (and adjusting $a \rightarrow a'$, $b \rightarrow b'$ accordingly) is equivalent to a diagonalizing or principal-axis transformation. Our specification of \hat{a} by (6.7) simultaneously, in each sperture coordinate system (O_T , O_R) usually requires that (O_T , O_{S_T} , O_{S_R} , O_R) form a plane perpendicular to the (x,y)-plane, cf. Fig. (5.1), e.g., $\phi_{OT}=0, \pi/2$ ($\phi_R=\pi/2, \pi$, cf. (5.24a)). More generally, we can always choose the orientation of the coördinate system for the beam at O_T to insure the vanishing of the off-diagonal terms in \hat{a}_T , but we cannot, then, simultaneously require this for the off-diagonal terms of \hat{a}_R , when the condition of the perpendicular plane is not satisfied: the projection of the (elliptical) receiving beam on S_0 will be a "tilted" ellipse in the O_{S_R} coördinate system. An exception is the case where one or both apertures are point sources, cf. (6.14) ff.

$$\hat{\underline{a}} = \begin{bmatrix} 1 & 0 & 0 \\ 0 & a^2 & 0 \\ 0 & 0 & b^2 \end{bmatrix}. \quad (6.7)$$

Moreover, for analytic convenience here and without any fundamental reduction in overall generality, we shall henceforth require the receiving beam (unless it is omni-directional, cf. (6.14)) to be so oriented that $0_{S_T}, 0_{S_R} (= 0_S \text{ if } \underline{r}_0 = 0)$, along with 0_T and 0_R form a plane perpendicular to the basic xy-reference plane of 0_T , cf. Fig. 5.1 (with $\phi_{0T} = 0$ or $\pi/2$). (This is also consistent with the experimental configuration of the associated experiments [6].) Thus, (6.7) applies for both Q_T, Q_R , (6.5), (6.6), simultaneously,* where now $a \rightarrow a_T, a_R; b \rightarrow b_T, b_R$, for the appropriate (diagonal) elements of $\hat{\underline{a}}_{T,R}$. We call such beams "perpendicular coplanar" ($\equiv \perp$ coplanar) beams.

With omni-directional beams, which are produced by (single) point-sources, we have for the source weighting, $A_T = g_T(f_0)\delta(\underline{\xi} - \underline{\xi}_0)$ at a point $\underline{\xi}_0$, so that the resulting beam pattern is

$$Q_T \Big|_{\text{omni}} = \int_{V_T} g_T \delta(\underline{\xi} - \underline{\xi}_0) e^{2\pi i \underline{v} \cdot \underline{\xi}} d\underline{\xi} = g_T e^{2\pi i \underline{v} \cdot \underline{\xi}_0}. \quad (6.8)$$

Consequently, with \underline{v} given by $(\hat{\underline{i}}_T - \hat{\underline{i}}_{0T})f_0/c_0, (\hat{\underline{i}}_R - \hat{\underline{i}}_{0R})f_0/c_0$ [cf. (5.26) with $\underline{r}_0 = 0$], we obtain at once the following beam patterns

$$\begin{aligned} Q_T \Big|_{\text{omni}} &= g_T(f_0) e^{ik_0(\hat{\underline{i}}_T(r) - \hat{\underline{i}}_{0T}) \cdot \underline{\xi}_0}; \\ Q_R \Big|_{\text{omni}} &= g_R(f_0) e^{ik_0(\hat{\underline{i}}_R(r) - \hat{\underline{i}}_{0R}) \cdot (\underline{L} + \hat{\underline{i}}_z[h_T - h_R])}; \end{aligned} \quad (6.9)$$

$$k_0 = 2\pi/\lambda_0 = 2\pi f_0/c_0.$$

Unlike the gaussian beams above, these omni-directional beams are "broad-beams" (B.B.) since (6.2) does not generally apply: $\hat{\underline{i}}_T(r) - \hat{\underline{i}}_{0T}$, etc., cannot usually be approximated as in (6.1); (however, see (6.14) ff. in the case of random surfaces).

*See footnote on page 64.

Since \underline{r} has no z-component, we can set the z-components of $\hat{\underline{a}}_{OT}$, $\hat{\underline{a}}_{OR}$, equal to zero without changing the projected ellipses $\underline{r} \cdot \hat{\underline{a}}_{OT} \cdot \underline{r}$, $(\underline{r} - \underline{r}_0) \cdot \hat{\underline{a}}_{OR} \cdot (\underline{r} - \underline{r}_0)$ on S_0 . For additional simplification we choose the coordinate system (0_S) so that the y-axes of 0_T , 0_S coincide, i.e., $\phi_{OT} = \pi/2$ ($\therefore \phi_{OR} = \pi$). Using (5.24) we readily find for (6.1a) that now ($\phi_{OT} = \pi/2$):

$$\hat{\underline{a}}_{OT} = \begin{bmatrix} 1 & 0 & 0 \\ 0 & \cos^2 \theta_{OT} & \sin^2 \theta_{OT} \cos \theta_{OT} \\ 0 & \sin^2 \theta_{OT} \cos \theta_{OT} & \sin^2 \theta_{OT} \end{bmatrix}; \quad (6.10)$$

$$\hat{\underline{a}}_{OR} \Big|_{\underline{r}_0=0} = \begin{bmatrix} 1 & 0 & 0 \\ 0 & 1 - \left(\frac{R_{OT} \sin \theta_{OT} - L_0}{R_{OR}} \right)^2 & \frac{(R_{OT} \sin \theta_{OT} - L_0) h_R}{R_{OR}^2} \\ 0 & \frac{R_{OT} \sin \theta_{OT} - L_0}{R_{OR}^2} h_R & 1 - \left(\frac{h_R}{R_{OR}} \right)^2 \end{bmatrix},$$

with

$$R_{OR} = \{(R_{OT} \sin \theta_{OT} - L_0)^2 + h_R^2\}^{1/2} \quad (6.10a)$$

here.*

Consequently, we see that, for (6.7),

$$\hat{\underline{A}}_{OT} = \left[\begin{array}{cc|c} 1 & 0 & 0 \\ 0 & a_T^2 \cos^4 \theta_{OT} + b_T^2 \cos^2 \theta_{OT} \sin^2 \theta_{OT} & x \\ 0 & x & x \end{array} \right] = \left[\begin{array}{cc|c} 1 & 0 & 0 \\ 0 & a_T^2(\theta_{OT}) & x \\ \hline & & x \end{array} \right] \quad (6.11)$$

and so that

*We note that $\det \hat{\underline{a}}_{OT} = 0$, but $\det \hat{\underline{a}}_{OR} \neq 0$ (unless $R @ T$, cf. mono-static operation); also $\hat{\underline{i}}_{OT} \cdot \hat{\underline{a}}_{OT} = 0$, etc.; cf. (6.1a): $\hat{\underline{i}}_{OT}$ minimizes the scalar $\hat{\underline{i}}_{OT} \cdot \hat{\underline{a}}_{OT} \cdot \hat{\underline{i}}_{OT}$ ($=0$), etc.

$$a_T^2(\theta_{oT}) \equiv (a_T^2 \cos^2 \theta_{oT} + b_T^2 \sin^2 \theta_{oT}) \cos^2 \theta_{oT}, \quad (\geq 0). \quad (6.11a)$$

Similarly, we get ($r_o = 0$):

$$\hat{A}_{oR} = \begin{bmatrix} 1 & 0 \\ 0 & a_R^2 \left[1 - \left(\frac{R_{oT} \sin \theta_{oT} - L_o}{R_{oR}} \right)^2 \right]^2 + b_R^2 \left(\frac{h_R}{R_{oR}} \right)^2 \left(\frac{R_{oT} \sin \theta_{oT} - L_o}{R_{oR}} \right)^2 \end{bmatrix} \quad (6.12)$$

$$= \begin{bmatrix} 1 & 0 \\ 0 & a_R^2(\theta_{oT}; L_o, h_R) \end{bmatrix}$$

where now

$$a_R^2(\theta_{oT}; L_o, h_R) \equiv a_R^2 \left[1 - \left(\frac{R_{oT} \sin \theta_{oT} - L_o}{R_{oR}} \right)^2 \right]^2 + b_R^2 \left(\frac{h_R}{R_{oR}} \right)^2 \left(\frac{R_{oT} \sin \theta_{oT} - L_o}{R_{oR}} \right)^2 \quad (\geq 0). \quad (6.12a)$$

From (6.11), (6.12) we see at once that the T and R beam patterns form (a continuum of) elliptical projections on the mean surface S_o ($= \langle z \rangle = 0$), e.g.,

$$\begin{cases} \underline{r} \cdot \hat{A}_{oT} \cdot \underline{r} \big|_{S_o} = x^2 + a_T^2(\theta_{oT}) y^2 = \text{constant} (\geq 0); & (6.13a) \\ \underline{r} \cdot \hat{A}_{oR} \cdot \underline{r} \big|_{S_o} = x^2 + a_R^2(\theta_{oT}; L_o, h_R) y^2 = \text{constant} (\geq 0); \quad \underline{r}_o = 0. & (6.13b) \end{cases}$$

6.2 Remarks

A variety of features of these beam patterns is to be noted:

- (1). The gaussian beam patterns [(6.3), (6.5), (6.6)], which have no "side lobes," can be well approximated in practice by the beam patterns produced by parametric transmitters (and receivers), which likewise have ignorable side lobes.
- (2). The use of these side-lobeless patterns provides significant analytic and computational simplification, particularly in the evaluation of scatter intensities, cf. Sec. 8 ff. These

"lobeless" patterns also enable us to distinguish, and avoid confusion with, the diffraction-grating patterns produced by scattering from any swell components in the wave surface (a point noted earlier by Tolstoy and Clay, p. 197, [9]).

- (3). A far-field condition is also required here, cf. (6.1), to enable us to replace the various angle-dependent quantities (e.g., $\underline{\alpha}$) with "central" values ($\underline{\alpha}_0$) defined at 0_S (and $0_{S'}$), and thus greatly simplify the subsequent evaluations. Otherwise, the exact expressions for $\hat{\underline{i}}_T$, $\hat{\underline{i}}_R$, etc. must be used,* as in the case of the omni-directional beams (6.9) with bi-static operation* ($R \neq T$).

With mono-static operation ($R \equiv T$), however, $\underline{\underline{L}}_0 \hat{\underline{i}}_Z (h_T - h_R) = \underline{\underline{\epsilon}}_0 = 0$ (by choosing 0_T at $\underline{\underline{\epsilon}}_0 = 0$) and then $Q_T|_{\text{omni}} = g_T$; $Q_R|_{\text{omni}} = g_R$.

Also, if either transmitter or receiver employs a "narrow-beam" (N.B.) while the other is "broad-beam" (B.B.) like $Q_R|_{\text{omni}}$ in (6.9), for example, the narrow-beam is always controlling in the product $Q_T \cdot Q_R|_{\text{omni}}$. Then $\underline{\underline{v}} = -\underline{\underline{v}}_R - \underline{\underline{v}}_{OR} \doteq$ Eq. (6.1), ($\underline{r}_0=0$) specifically in (6.9), e.g., $\hat{\underline{i}}_R(\underline{r}) - \hat{\underline{i}}_{OR} \doteq (\underline{r} \cdot \hat{\underline{a}}_{OR}) f_0 / c_0 R_{OR}$, so that now*

$$Q_R|_{\text{omni}} \doteq g_R(f_0) e^{ik_0(\underline{r} \cdot \hat{\underline{a}}_{OR} \cdot \underline{R}_{TR})/R_{OR}} \quad (6.14)$$

$$\underline{R}_{TR} = \text{Eq. (5.23d)}, \quad R_{OR} = \text{Eq. (6.10a)},$$

when, say, Q_T is described by (6.5). Moreover, it is no longer necessary that 0_T , 0_S , 0_R form a plane perpendicular to the xy-plane, since the projections of an omnidirectional beam on a plane are always circles.

*Actually, if the maximum correlation distance of the (here random) wave surface is small compared to the minimum distances to the transmitter and receiver, the "illuminated" portion of the surface is split up into essentially independent régimes, each of which is in the far-field, so that Eq. (6.14) for omnidirectional beams can be employed.

In effect, the far-field condition here requires that the $\sqrt{\text{area}_I}$ of joint "illumination" by the transmitter (and "viewing," by the receiving beam), over which the resultant beam pattern magnitude is significant, be small compared to the distances R_{OT} , R_{OR} . Quantitatively, this may be expressed by

$$\sqrt{\text{area}_I} = \sqrt{\pi} r_b (\equiv \sqrt{ad\pi}) \ll R_{OT}, R_{OR}, \quad (6.15)$$

where a , d are respectively the major and minor semi-axes of the elliptical projection on S_0 , at some level, $-N_b$ db, down from the maximum joint beam gain $g_T g_R$, cf. (6.17), and III, Sec. 6.5 ff.

- (4). A reasonable generalization of (6.5), (6.6) is to replace the constant phase terms ϕ_T , ϕ_R by the linear terms (in \underline{v}):

$$\phi_T \equiv 2\pi \underline{v} \cdot \underline{L}_T(f_0); \quad \phi_R \equiv 2\pi \underline{v} \cdot \underline{L}_R(f_0), \quad (6.16)$$

where now \underline{v} is given by (6.1) in these N.B. cases, and $\underline{L}_{T,R}$ has the dimension [L].

- (5). We note the dependence of the beam patterns on frequency ($\sim k_0$): this is a direct consequence of the definition of beam pattern as the spatial fourier transform of the (physical) aperture weightings $A_T(\underline{x}_i)$, $A_R(\underline{y}_j)$, cf. (5.6), (5.12), (5.13). [Tolstoy and Clay, however ([9], Sec. 6.3 et seq.), do not explicitly include this frequency dependence, which leads to a somewhat different interpretation of scattering intensity.] Moreover, as (6.3), (6.5), (6.6) show, the beam patterns behave as expected vis-à-vis aperture size and frequency. Then, as A_T , A_R cf. (6.5), (6.6), are made larger, the beam patterns become sharper or "narrower." Similarly, as the signal frequency ($\sim f_0$) is increased, so also do the beam patterns contract: as wavelength (λ_0) is decreased, the (fixed) physical aperture becomes (acoustically) larger. In addition, the beam gains $[g_T(f_0), g_R(f_0)]$, and phase parameters (ϕ_T, ϕ_R) , are also frequency-dependent.

6.3 The "Narrow-Beam" Case

In order to simplify the evaluation of the Total Surface Spreading Functions (TSSF's), (5.26), as noted above we must use beams (or at least one beam, here Q_T) which are sufficiently "narrow" that their effective projections on the sea surface (specifically on S_0), are invariant of angle variations over that projected area, cf. remark (3) above, Sec. 6.2. These projections, of course, depend on the surface distance \underline{r} , cf. Fig. 5.1.

Here we shall give the conditions relating aperture size ($\sim A_T, A_R$), frequency ($\sim k_0$), and distance (R_{OT}, R_{OR}) which permit this replacement of angle-quantities by these single values established at O_S on S_0 . This is what we mean by "factoring of the beam patterns." Accordingly, we begin with the elliptical, \perp -coplanar beams of Sec. 6.1, where $\underline{r}_0 = 0$ so that O_{ST}, O_{SR} coincide. From (6.5) and (6.6), with (6.11), (6.12), we can write for the combined gaussian beam patterns

$$Q_{RT} \Big|_{\text{gauss}} \equiv Q_{RT} = g_R g_T e^{-\frac{1}{2} k_0^2 (A x^2 + B y^2) + i k_0 (C x + D y)}, \quad (6.17)$$

where (6.16) is used, and where

$$A \equiv \frac{A_T}{R_{OT}^2} + \frac{A_R}{R_{OR}^2}; \quad B \equiv a_T^2(\theta_{OT}) \frac{A_T}{R_{OT}^2} + a_R^2(\theta_{OT} | L_{\sigma} h_R) \frac{A_R}{R_{OR}^2} (\leq A), \quad (6.17a)$$

$$C = (\hat{a}_{OT} \cdot \underline{\ell}_T)_x / R_{OT} + (\hat{a}_{OR} \cdot \underline{\ell}_R)_x / R_{OR}; \quad (6.17b)$$

$$D = (\hat{a}_{OT} \cdot \underline{\ell}_T)_y / R_{OT} + (\hat{a}_{OR} \cdot \underline{\ell}_R)_y / R_{OR}$$

with a_T^2, a_R^2 given by (6.11a), (6.12a).

We distinguish two principal geometries:

A. Backscatter Geometry: $R \approx T$ (identical beams)

$$A = 2A_T / R_{OT}^2; \quad B = 2a_T^2(\theta_{OT}) A_T / R_{OT}^2; \quad \therefore B = a_T^2(\theta_{OT}) A. \quad (6.18)$$

In addition, with circular (conical) beams $b_T = a_T$ and thus $a_T^2(\theta_{OT}) = a_T^2 \cos^2 \theta_{OT}$, cf. (6.11a).

B. Forward Scatter Geometry: Specular Direction (identical beams)

In this case (5.29) applies and again $a_R^2(\theta_{OT} | \dots) = a_T^2(\theta_{OT})$, (6.11a), with

$$A = A_T(1/R_{OT}^2 + 1/R_{OR}^2); \quad B = a_T^2(\theta_{OT})A_T(1/R_{OT}^2 + 1/R_{OR}^2) = a_T^2(\theta_{OT})A \quad (6.19)$$

for these identical beams. Here, however, $R_{OR} \neq R_{OT}$ usually.

For the somewhat more specialized beam choices of the Roderick experiments [6], where the receiving beam is omni-directional, cf. (6.9) and (6.14), we have (6.17) for the combined beams, where now $\underline{l}_R = \hat{a}_{OR} \cdot \underline{R}_{TR}/R_{OR}$, $\underline{l}_T \neq 0$. Thus, the parameters (6.17a,b) of the combined beams are now

$$\left. \begin{aligned} A &= A_T/R_{OT}^2; \quad B = a_T^2(\theta_{OT})A_T/R_{OT}^2; \\ C &= (\hat{a}_{OT} \cdot \underline{l}_T)_X/R_{OT} + (L/R_{OR})\sin\phi_L; \\ D &= (\hat{a}_{OT} \cdot \underline{l}_T)_Y/R_{OT} + \left\{ 1 - \left(\frac{R_{OT}\sin\theta_{OT} - L_0}{R_{OR}} \right)^2 \right\} \cos\phi_L \end{aligned} \right\} \quad (6.20)$$

For the \perp -coplanar condition, $\phi_L = 0$, consistent with $\phi_{OT} = \pi/2$, cf. Fig. 5.1. However, since the receiving beam is omnidirectional, (6.14), this condition can be relaxed, and ϕ_L does not necessarily vanish. For the back- and forward-scatter geometries of (6.18), (6.19), we find that (6.20) reduces to:

C. Backscatter Geometry (Gauss x Omni): $\phi_L = 0$

$$\left. \begin{aligned} A &= A_T/R_{OT}^2; \quad B = a_T^2(\theta_{OT})A; \quad C = \underline{l}_{TX}/R_{OT}; \\ D &= \underline{l}_{Ty}\cos^2\theta_{OT}/R_{OT} + \cos^2\theta_{OT}. \end{aligned} \right\} \quad (6.21)$$

D. Forward Scatter Geometries (Gauss x Omni), in the Specular Direction

Here we have $\phi_L = 0$, $\phi_{OT} = \pi/2$, $\phi_{OR} = \pi$, and A, B, C, D are readily found to reduce to (6.21), provided we invoke (5.29), as required for the specular direction. Off the specular direction, of course, C and D differ from (6.21).

Our next step is to relate an effective beam width, $\Delta\beta$, to: (i) the beam parameters (A_T , k_0 , ...); (ii) the "narrow-beam" conditions (6.2) above. This is done by choosing some distance (r_{b-max}) on S_0 where the maximum projection of the beam falls to b^{-1} of its maximum value (g_T), (6.3), in the manner of Fig. 6.1.

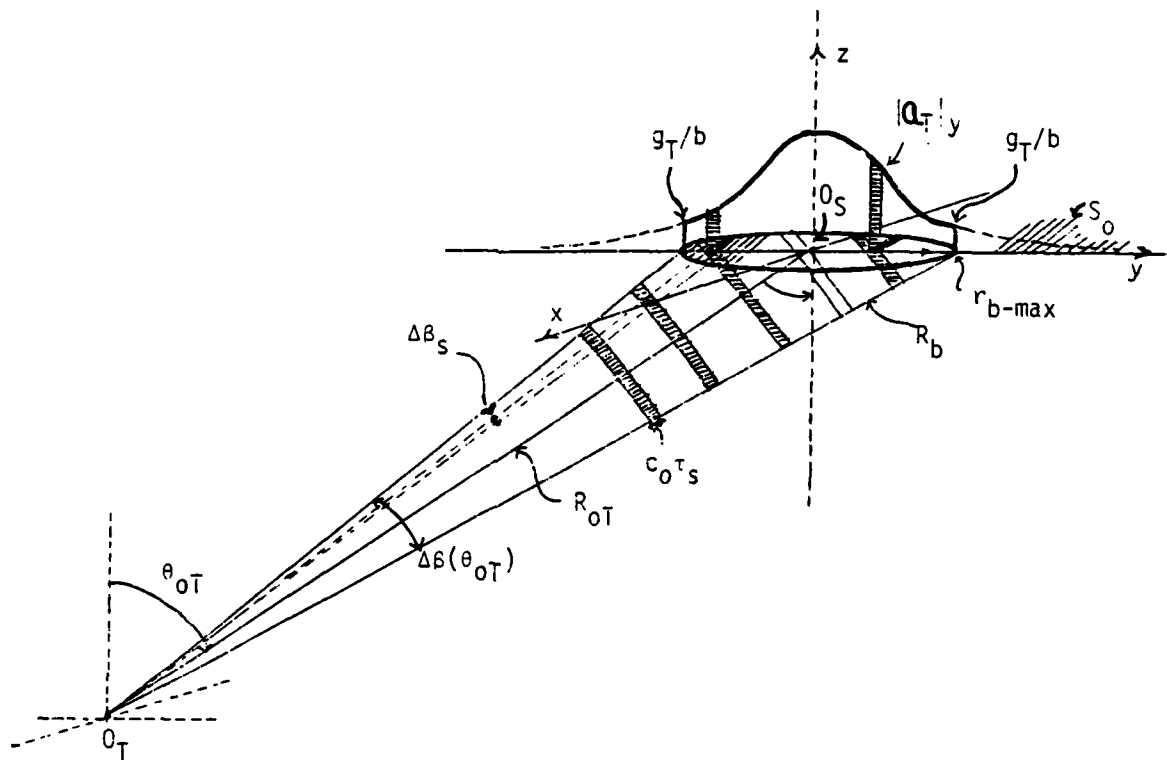


Figure 6.1. Geometry of effective beam width, $\Delta\beta_T$, in the far field, $r_{b-max}/R_{OT} \ll 1$, showing illumination by "short" pulses.

For the gaussian beam (6.5) we get (in the far-field)

$$|Q_T(\underline{r}_b, \underline{r}_{OT}; f_0)| = g_T \exp \left\{ -\frac{1}{2} k_0^2 A_T (x_b^2 + a_T^2 (\theta_{OT})^2 y_b^2) / R_{OT}^2 \right\} = g_T / b. \quad (6.22)$$

Taking the largest projection on S_0 , viz. y_b , ($a_T < 1$) and solving (6.22) for y_b / R_{OT} , $x_b = 0$, we get directly

$$\hat{y}_b \equiv r_{b-\max} / R_{OT} = (2 \log b / A_T a_T^2 (\theta_{OT}) k_0^2)^{1/2} \ll 1, \quad (6.23)$$

where we recall the far-field condition (6.2). From the far-field geometry of Fig. 6.1 it is easily seen that the effective beam width is now (in the far-field)

$$\Delta \beta_{T,b} \doteq 2 \hat{y}_b \cos \theta_{OT}, \quad (6.24)$$

subject to the condition

$$\hat{y}_b \equiv r_{b-\max} / R_{OT} = \sqrt{2 \log b / A_T} / k_0 a_T (\theta_{OT}) \doteq \frac{\Delta \beta_{T,b}}{2 \cos \theta_{OT}} \ll 1, \quad b > 1. \quad (6.24a)$$

Here (6.11a) gives $a_T(\theta_{OT}) = a_T \cos \theta_{OT} (\cos^2 \theta_{OT} + b_T / a_T)^2 \sin^2 \theta_{OT})^{1/2}$
(= $a_T \cos \theta_{OT}$ for circular beams, $a_T = b_T$).

E. Example

These data are obtained from experiment [6]. We have

$$\left. \begin{aligned} \Delta \beta_{T,b} &= 5^\circ @ -10 \text{ db } (:b = 10) = 8.73 \cdot 10^{-2} \text{ rad.} \\ \theta_{OT} &= 83^\circ = \text{minimum grazing angle used.} \end{aligned} \right\} \therefore \underline{\hat{y}_b = 0.358}. \quad (6.25a)$$

which is not very small. We should have $\hat{y}_b \leq O(10^{-2})$ comfortably.

Since $h_T / \cos \theta_{OT} = R_{OT}$, we easily find that for $h_T = 28.7$ m, $R_{OT} = 235$ m, and $\therefore r_b \doteq 84.3$ m, from (6.24a). (This is approximate, since \hat{y}_b , (6.25a), does not obey (6.24a) very well.) The effective bandwidth of 5° at -10 db (from g_T) is measured at 20 kHz. This permits us to estimate the equivalent aperture cross section A_T , under the assumption of fully circular beams [$a_T = b_T (= 1)$]. Since

$$A_T \doteq \frac{1}{2}(a_T k_0 \Delta \beta_{T,b})^2 \log_e b \quad (6.25b)$$

from (6.24a), we find that at $f_0 = 20$ kHz, or $\lambda_0 = (3/40)$ m, $\therefore \underline{A_T = 6.16 \text{ m}^2}$, ($b = 10$), cf. Fig. 6.1.

Now $\hat{y}_b \sim 0.36$, cf. (6.25a), does not very well satisfy the far-field requirements. To overcome this critical defect (which otherwise greatly increases the practical complexity of our results, vide Sec. 6.2, and above), we can achieve the desired effectively narrow beams by using suitably "short" signal pulses, so that only a comparatively small portion of the projected beam area on S_0 is illuminated at any given instant, cf. Fig. 6.1. If τ_s is the pulse duration, then

$$r_{b-\max} \rightarrow \Delta r_{b-\max} \doteq 2\tau_s c_0 / \cos \theta_{OT}; \therefore \Delta r_{b-\max} / R_{OT} \ll 1, \quad (6.26a)$$

as required, where $2\tau_s c_0$ is the pulse distance in the medium. The new effective beam width is

$$\Delta \beta_s = \Delta r_{b-\max} \cos \theta_{OT} / R_{OT} \doteq 2\tau_s c_0 / R_{OT}. \quad (6.26b)$$

Thus, for $\tau_s = 10^{-3}$ sec, $\Delta r_{b-\max} \doteq 24.6$ m, and $\therefore \Delta r_{b-\max} / R_{OT} = 0.10$, which is better. Still better are pulses with $\tau_s = 4 \cdot 10^{-4}$ secs, say, as then the far-field condition becomes $\Delta r_{b-\max} / R_{OT} = 0.04 \ll 1$, acceptably.

However, there is a limit to how short a signal duration can be tolerated before our postulated "narrow-band" condition [(5.31), (i)] breaks down and we must then account for the fact that our apertures are frequency-variable, i.e., they act like (linear) filters, cf. (5.6). We discuss this point in Sec. 6.4 following.

6.4 Beam Convolutions

To appreciate the filtering action of the aperture in its response to signals of finite bandwidth, let us consider (5.9) and (5.10) once more, now with driving signals of arbitrary temporal structure. We consider for the moment the unscattered field α_H . Instead of (5.10) in the frequency domain (now with $s_0 \rightarrow s$), we can write in the time domain the temporal convolution

$$\alpha_H \sim \int_{-\infty}^{\infty} d\tau \int_{V_T} A_T(\underline{x}, t-\tau+t^*(\underline{x})) S_{in}(\tau, \underline{x}) d\underline{x}; \quad t^* \equiv \underline{i}_T \cdot \underline{x} / c_0 - R_{OT} / c_0. \quad (6.27a)$$

Alternatively, this may be expressed, for $S_{in}(\tau, \underline{x}) = S_{in}(\tau)$: uniform drive, as

$$\alpha_H \sim \int_{Br_1} e^{s(t-R_{OT}/c_0)} S_{in}(\frac{s}{2\pi i}) Q_T(s \cdot (\underline{i}_T - \underline{i}_{OT}) / c_0, s) \frac{ds}{2\pi i}, \quad (6.27b)$$

where $S_{in}(\frac{s}{2\pi i})$ is the (amplitude) spectrum of the applied signal, cf. (5.12), (5.13). Equations (6.27a) and (6.27b) may be described, functionally, as

$$\left. \begin{aligned} (6.27a): \quad \alpha_H &\sim \text{aperture weighting} \otimes \text{driving signal waveform;} \\ (6.27b): \quad \alpha_H &\sim \text{F.T. (beam pattern} \times \text{driving signal's spectrum) df,} \end{aligned} \right\} (6.27c)$$

where \otimes denotes (here temporal) convolution, and F.T., the fourier transform.

For narrow-band signals (about $s_0 = 2\pi f_0$) we have $S_{in}(\frac{s'+s_0}{2\pi i}) \doteq S_{in}(\frac{s'}{2\pi i})$, where $S_{in} \neq 0$, $|s'| \leq \Delta f \ll f_0$. Then the general relation (6.27b) becomes

$$\alpha_H \sim e^{s_0(t-R_{OT}/c_0)} \int_{Br_1} S_{in}(\frac{s'}{2\pi i}) Q_T([\underline{i}_T - \underline{i}_{OT}](s'+s_0)/c_0; s_0) e^{s'(t-R_{OT}/c_0)} \frac{ds'}{2\pi i}. \quad (6.28)$$

Provided S_{in} is spectrally (considerably) narrower* than Q_T , Q_T may here be considered essentially constant (in s') vis-à-vis S_{in} , and so (6.28) reduces to

$$\alpha_H \sim Q_T([\underline{i}_T - \underline{i}_{OT}]s_0/c_0; s_0) \int_{Br_1} S_{in}(s/2\pi i) e^{s(t-R_{OT}/c_0)} \frac{ds}{2\pi i}, \quad (6.29)$$

which is just the form of (5.14) earlier, as expected. This is the "narrow-band" postulate of our analysis, generally.

*We may set $k_0 \rightarrow k'$, ($k' < (<) k_0$), in (6.5) and specifically compare Q_T with S_{in} to establish a workable quantification of the term "narrow" here.

Accordingly, as long as the pulsed signals of Sec. 6.3, cf. (6.26a), are not too "short," i.e., as long as $\tau_s \leq \Delta f^{-1}$ of \underline{Q}_T , we can "factor" the beam pattern and signal spectrally according to (6.29). The "scanning" of the beam projection on S_0 in Fig. 6.1 is then automatically accounted for by (5.26) in (5.21a) through the spectral structure of these narrow-band "short" signals embodied in $S_{in}(s/2\pi i)$.

6.5 Beam Integrals for Scatter Intensities

When the narrow-band condition for the signals is obeyed, the beam pattern \underline{Q} and the signal spectrum, S_{in} , "factor," as in (6.29), (5.21a), (5.26). When in addition we have gaussian and/or omni-directional beam patterns of the type (6.5), (6.6), and particularly here, (6.17), in the far-field, it is possible to evaluate a variety of integrals over S_0 , which arise in the evaluation of the coherent and incoherent scatter intensities (cf. Section 8 ff.). We summarize these results here.

The integrals in question involve the beam pattern products $\underline{Q}_T \underline{Q}_R \equiv \underline{Q}_{TR}$. With the help of (6.1) in (6.16), we see that (as long as one of the beams is "narrow" in the sense of (6.2), now with $\underline{r}_0 = 0$)

$$\phi_T \doteq k_{0T} \underline{r} \cdot \underline{\hat{a}}_{OT} \cdot \underline{l}_{OT}/R_{OT}; \quad \phi_R \doteq k_{0R} \underline{r} \cdot \underline{\hat{a}}_{OR} \cdot \underline{l}_R/R_{OR}, \quad (6.30)$$

so that from (6.5), (6.6), we may write directly

$$\underline{Q}_T \underline{Q}_R \equiv \underline{Q}_{TR} = g_T g_R e^{-\frac{1}{2} k_{0T}^2 \underline{\hat{B}}_{TR} \cdot \underline{r} + i k_{0T} \underline{r} \cdot \underline{b}_{TR}}, \quad (6.31)$$

where from (6.11), (6.12)

$$\underline{\hat{B}}_{TR} = \frac{A_T}{R_{OT}^2} \underline{\hat{A}}_{OT} + \frac{A_R}{R_{OR}^2} \underline{\hat{A}}_{OR} = \begin{bmatrix} \frac{A_T}{R_{OT}^2} + \frac{A_R}{R_{OR}^2} & 0 \\ 0 & a_T^2(\theta_{OT}) \frac{A_T}{R_{OT}^2} + a_R^2(\theta_{OT}, \theta_{OR}, L) \frac{A_R}{R_{OR}^2} \end{bmatrix}, \quad (6.32a)$$

$$\equiv \begin{bmatrix} A & 0 \\ 0 & B \end{bmatrix}. \quad (6.32b)$$

Also, we have

$$\underline{b}_{TR} = \hat{a}_{OT} \cdot \underline{l}_T / R_{OT} + \hat{a}_{OR} \cdot \underline{l}_R / R_{OR} = \begin{bmatrix} b_{Tx} = C \\ b_{Ty} = D \\ 0 \end{bmatrix} = \begin{bmatrix} \text{Eq. (6.17b)} \\ \text{or} \\ \text{Eq. (6.20)} \\ 0 \end{bmatrix}$$

$$= \begin{bmatrix} \underline{l}_{Tx}/R_{OT} + \underline{l}_{Rx}/R_{OR} \\ \frac{\underline{l}_{Ty} \cos^2 \theta_{OT} + \underline{l}_{Tz} \sin \theta_{OT} \cos \theta_{OT}}{R_{OT}} + 1 - \frac{(R_{OT} \sin \theta_{OT} - L)^2}{R_{OR}^2} \underline{l}_{Ry}/R_{OR} + \frac{(R_{OT} \sin \theta_{OT} - L) \underline{l}_R \cdot \underline{l}_{Rz}}{R_{OR}^3} \\ 0 \end{bmatrix} \quad (6.33)$$

from (6.10), where we set the z-component of \underline{b}_{TR} to zero, since generally \underline{r} lies only in the (x,y)-plane.

The integrals in question are

$$\left\{ \begin{aligned} I_2(\underline{\alpha}_0, \hat{\underline{D}}) &\equiv \int_{-\infty}^{\infty} \underline{a}_{RT}(\underline{r}_1) d\underline{r}_1 \int_{-\infty}^{\infty} d(\underline{\Delta r}) \underline{a}_{RT}(\underline{r}_1 + \underline{\Delta r})^* e^{ik_0 2\underline{\alpha}_0 \cdot \underline{\Delta r} - \frac{k_0^2}{2} \underline{\Delta r} \cdot \hat{\underline{D}}_M \cdot \underline{\Delta r}} \\ &\quad \underline{\Delta r} \equiv \underline{r}_2 - \underline{r}_1 \end{aligned} \right\} \quad (6.34)$$

$$\left\{ \begin{aligned} I_1(\underline{\alpha}_0) &\equiv I_2(\hat{\underline{D}}_M = 0); \end{aligned} \right. \quad (6.35)$$

$$\text{and } \left\{ \begin{aligned} I_3(\underline{\Delta r}) &\equiv \int_{-\infty}^{\infty} \underline{a}_{RT}(\underline{r}_1) \underline{a}_{RT}(\underline{r}_1 + \underline{\Delta r})^* d\underline{r}_1. \end{aligned} \right. \quad (6.36)$$

(Note that since $\underline{r}_1, \underline{\Delta r}$ have no z-components, we can set $(\underline{\alpha}_0)_z = 0$ throughout in what follows.)

Since \underline{a}_{RT} , (6.31), are (symmetric) quadratic forms exponentially, at most, over infinite intervals, we can use the well-known result, Eq. (7.26) of [45] (in vector, dyadic notation):

$$I(\underline{\xi}) = \int_{[\underline{u}]} e^{i\underline{\xi} \cdot \underline{u} - \frac{1}{2} \underline{u} \cdot \hat{\underline{A}} \cdot \underline{u}} d\underline{u} = \frac{(2\pi)^{n/2}}{[\det \hat{\underline{A}}]^{1/2}} e^{-\frac{1}{2} \underline{\xi} \cdot \hat{\underline{A}}^{-1} \cdot \underline{\xi}}, \quad (6.37)$$

where $\hat{\underline{A}}^{-1}$ = dyadic form of the inverse square matrix $\hat{\underline{A}}^{-1}$, e.g., $\underline{\xi} \cdot \underline{u} \rightarrow \underline{\xi} \underline{u}$; $\underline{u} \cdot \hat{\underline{A}} \cdot \underline{u} = \underline{u} \hat{\underline{A}} \underline{u}$, where the elements of the matrix \underline{A} are the various (xx, xy, ...) components of the dyadic $\hat{\underline{A}}$. Thus, $\det \hat{\underline{A}} \equiv \det \underline{A}$, etc. Applying (6.37) successively to (6.34) with (6.31) yields after considerable matrix manipulation (on replacing dyadics by matrices, as convenient)*:

$$I_2 = \frac{(g_T g_R)^2 2\pi^2}{k_0^4 \sqrt{\det \underline{\hat{G}}}} e^{-\frac{1}{2} (2\underline{\alpha}_0 - \underline{b}_{TR}) (\hat{\underline{E}}^{-1} + \frac{1}{16} \underline{\hat{H}} \underline{\hat{G}}^{-1} \underline{\hat{H}}) (2\underline{\alpha}_0 - \underline{b}_{TR})} \quad (6.38)$$

where

$$\hat{\underline{E}} \equiv \hat{\underline{B}}_{TR} + \hat{\underline{D}}_M = \begin{bmatrix} A + d_{11} & d_{12} \\ d_{12} & B + d_{22} \end{bmatrix} = \underline{\hat{E}}; \quad \hat{\underline{D}}_M = \begin{bmatrix} d_{11} & d_{12} \\ d_{12} & d_{22} \end{bmatrix} = \underline{\hat{D}}_M \quad (6.38a)$$

$$\det \hat{\underline{E}} = AB + (Bd_{11} + Ad_{22}) + (d_{11}d_{22} - d_{12}^2) > 0; \quad (6.38b)$$

$$\hat{\underline{E}}^{-1} = \begin{bmatrix} B + d_{22} & -d_{12} \\ -d_{12} & A + d_{11} \end{bmatrix} (\det \hat{\underline{E}})^{-1};$$

$$\underline{\hat{G}} \equiv \hat{\underline{B}}_{TR} - \frac{1}{2} \hat{\underline{B}}_{TR} \hat{\underline{E}}^{-1} \hat{\underline{B}}_{TR} = \underline{\hat{G}}; \quad (6.38c)$$

$$\underline{\hat{H}} \equiv \hat{\underline{B}}_{TR} \hat{\underline{E}}^{-1} + \hat{\underline{E}}^{-1} \hat{\underline{B}}_{TR} = \underline{\hat{H}}, \quad (6.38d)$$

and only the (x and y) components of $2\underline{\alpha}_0 - \underline{b}_{TR}$ are used here.

Equation (6.38) is an exact result. Note that the exponent of (6.38)

*Although $\hat{\underline{B}}_{TR}$ in (6.31) is diagonal, $\hat{\underline{D}}_M$ in (6.34) is not--hence the utility of the matrix technique here.

is independent of frequency.* This occurs here because of the explicit frequency dependence of the beam patterns in our formulation [(6.3)-(6.6), and (6.31)], which is required, realistically.

For I_1 , (6.35), we find that since $\hat{\underline{D}}_M = \underline{0}$, $\hat{\underline{E}} = \hat{\underline{B}}_{TR}$, and $\underline{G} = \frac{1}{2} \hat{\underline{B}}_{TR}$, $\underline{H} = 2\underline{I}$, so that $\underline{G}^{-1} = 2\hat{\underline{B}}_{TR}^{-1} = 2\hat{\underline{E}}^{-1}$, and since $\det(\frac{1}{2} \hat{\underline{B}}_{TR}^2) = (1/2)^2 \det^2 \hat{\underline{B}}_{TR}$, we get directly from (6.38)

$$\begin{aligned} I_1(\underline{\alpha}_0) &= \int_{-\infty}^{\infty} \underline{Q}_{RT}(\underline{r}_1) d\underline{r}_1 \int_{-\infty}^{\infty} d(\underline{\Delta r}) \underline{Q}_{RT}(\underline{r}_1 + \underline{\Delta r})^* e^{ik_0 2\underline{\alpha}_0 \cdot \underline{\Delta r}} \\ &= (g_T g_R)^2 \frac{2\pi^2}{k_0^4 AB} e^{-\frac{3}{4}(2\underline{\alpha}_0 - \underline{b}_{TR}) \hat{\underline{B}}_{TR}^{-1} (2\underline{\alpha}_0 - \underline{b}_{TR})} = I_1(\underline{\alpha}_0 - \underline{b}_{TR}) \end{aligned} \quad (6.39)$$

since $\det \hat{\underline{B}}_{TR} = AB$, cf. (6.32b). Equation (6.39) is also exact.

For I_3 , (6.36), we get from (6.31)

$$I_3(\underline{\Delta r}) = \frac{(g_T g_R)^2 \pi}{k_0^2 \sqrt{AB}} e^{-\frac{1}{4} k_0^2 [(\Delta x)^2 A + (\Delta y)^2 B] - ik_0 \underline{b}_{TR} \cdot \underline{\Delta r}} \quad (6.40)$$

We note the explicit rôle of the phase terms ($-\underline{b}_{TR}$ (6.33)) [cf. (6.5), (6.6); (6.16), (6.17)] in the above results (6.38)-(6.40). Again, only the x- and y-components of $2\underline{\alpha}_0 - \underline{b}_{TR}$, \underline{b}_{TR} (6.33), are used here. Finally, because \underline{B}_{TR} is diagonal, there are no "xy"-components in the exponents of (6.39), (6.40).

A. Approximations

Let us consider the second (square) matrix in the exponent of (6.38), I_2 :

$$\tilde{\underline{H}} \underline{G}^{-1} \underline{H} = (\tilde{\underline{E}}^{-1} \tilde{\underline{B}}_{TR} + \tilde{\underline{E}} \hat{\underline{B}}_{TR} \hat{\underline{E}}^{-1}) (\hat{\underline{B}}_{TR} - \frac{1}{2} \tilde{\underline{B}}_{TR} \hat{\underline{E}}^{-1} \hat{\underline{B}}_{TR}) (\hat{\underline{B}}_{TR} + \tilde{\underline{E}}^{-1} \tilde{\underline{B}}_{TR} \hat{\underline{E}}) \hat{\underline{E}}^{-1}. \quad (6.41)$$

*This agrees with Tolstoy and Clay [9], cf. Eq. (6.74) et seq. therein. However, we note here the k_0^{-4} factor in (6.38), rather than the k_0^{-2} factor of Eq. (6.74), [9]. The formulation of Tolstoy and Clay [9] does not include an explicit frequency dependence ($\sim k_0$). (The insensitivity of the exponent to frequency stems generically from its dimensionless character.)

If

$$d_{11}, d_{22} \gg A, B, \text{ cf. (6.38a)} \quad \therefore \hat{\underline{E}} \gg \hat{\underline{B}}_{\text{TR}}; \quad \text{and} \quad \boxed{\hat{\underline{E}} \doteq \hat{\underline{D}}_{\text{M}}} \quad (6.42a)$$

If

$$\left. \begin{aligned} \hat{\underline{E}}^{-1} \gg \hat{\underline{B}}_{\text{TR}}, \quad (\det \hat{\underline{D}}_{\text{M}} = d_{11}d_{22} - d_{12}^2 > 0) \\ \therefore \hat{\underline{H}}\hat{\underline{G}}\hat{\underline{H}}^{-1} = O(\hat{\underline{B}}_{\text{TR}}\hat{\underline{E}}^{-1}) \ll \hat{\underline{E}}^{-1}. \end{aligned} \right\} \quad \therefore \boxed{\underline{I} \gg \hat{\underline{B}}_{\text{TR}}^2}; \quad (6.42b)$$

And we have

$$\therefore \det \underline{\underline{G}}\underline{\underline{E}} \doteq \det \underline{\underline{E}}\hat{\underline{B}}_{\text{TR}} = \det \hat{\underline{E}} \det \hat{\underline{B}}_{\text{TR}} \doteq AB \det \hat{\underline{D}}_{\text{M}} = AB(d_{11}d_{22} - d_{12}^2). \quad (6.42c)$$

Consequently, (6.38) now reduces to

$$\boxed{I_2(\alpha_0 - \underline{b}_{\text{TR}} | \theta_{\text{OT}}) \doteq \frac{(g_{\text{T}}g_{\text{R}})^2 2\pi^2}{k_0^4 \sqrt{AB(d_{11}d_{22} - d_{12}^2)}} e^{-\frac{1}{2}(2\alpha_0 - \underline{b}_{\text{TR}})\hat{\underline{D}}_{\text{M}}^{-1}(2\alpha_0 - \underline{b}_{\text{TR}})}} \quad (6.43)$$

$$\det \hat{\underline{D}}_{\text{M}} = d_{11}d_{22} - d_{12}^2 (> 0),$$

which has "xy"-components in the exponent, since $\hat{\underline{D}}_{\text{M}}$ is not usually diagonal, cf. (6.39), (6.40) above. The inequalities above are reasonable provided the grazing angle $\phi_{\text{OT}} (= \pi/2 - \theta_{\text{OT}})$ is not too small, i.e., θ_{OT} is not too close to $\pi/2$. We must, of course, test (6.42a)-(6.42c) for actual geometries, as used in the experiments of Roderick [6].

A.1. Change of Dimensions

Finally, we note that if k_0^2 is absorbed into A, B, and k_0 into C, D, of (6.17), (6.17a), i.e., $A, B = O(L^{-2})$, $C, D = O(L^{-1})$ dimensionally, then I_1 , (6.39), and I_2 , (6.43), replace the k_0^4 factor by k_0^2 , while I_3 , (6.40), has no k_0^2 in the denominator. Furthermore, in (6.39) we must then also insert a factor k_0^2 in the exponent. In this form the dependence of the effective aperture size on frequency is disguised.

B. Explicit Forms: \underline{b}_{TR} , $2\alpha_0 - \underline{b}_{TR}$

The explicit general forms for \underline{b}_{TR} are given here by (6.33), for N.B. patterns, in the usual far-field state. For the more general quantity $2\alpha_0 - \underline{b}_{TR}$ we combine (6.33) and (5.25), to obtain

$$\begin{aligned}
 2\alpha_0 - \underline{b}_{TR} = & \hat{i}_x \{ (1 + R_{OT}/R_{OR}) \cos \phi_{OT} \sin \theta_{OT} - (\ell_{Tx}/R_{OT} + \ell_{Rx}/R_{OR}) \} \\
 & + \hat{i}_y \left\{ (1 + R_{OT}/R_{OR}) \sin \phi_{OT} \sin \theta_{OT} - L_O/R_{OR} - \left(\frac{\ell_{Ty} \cos^2 \theta_{OT} + \ell_{Tz} \sin \theta_{OT} \cos \theta_{OT}}{R_{OT}} \right) \right. \\
 & \left. + \left[1 - \frac{(R_{OT} \sin \theta_{OT} - L_O)^2}{R_{OR}^2} \right] \ell_{Ry}/R_{OR} + \frac{(R_{OT} \sin \theta_{OT} - L_O) h_R \ell_{Rz}}{R_{OR}^3} \right\}. \quad (6.44)
 \end{aligned}$$

Equation (6.44) can be simplified somewhat, depending on the geometry of the (N.B.) arrays employed. For a vertical array we have

$$(i). \text{ Vertical array: } \underline{\ell}_V = \hat{i}_z \ell_z; \quad (6.45a)$$

$$(ii). \text{ Horizontal array: } \underline{\ell}_H = \hat{i}_x \ell_x + \hat{i}_y \ell_y; \quad (6.45b)$$

and for a combined horizontal-vertical configuration (to form a beam of effectively cylindrical shape), we can superpose (i) and (ii) to get

$$(iii). \text{ Cylindrical Beam: } \underline{\ell} = \underline{\ell}_V + \underline{\ell}_H = \hat{i}_x \ell_x + \hat{i}_y \ell_y + \hat{i}_z \ell_z \quad (6.45c)$$

$$= \hat{i}_x \ell_x + \hat{i}_z \ell_z, (\ell_y = 0: \quad (6.45d)$$

horizontal array axis on x).

Accordingly, we can set $\ell_y = 0$ in (6.44) for "cylindrical" beams.

In addition, we note that the maximum effective dimensions of the array are small compared to the fundamental distances R_{OT} , R_{OR} , cf. Fig. 5.1, as required by the far-field or Fraunhofer condition imposed throughout the present analysis. This means that $\ell_{x,y,z}/R_{OT}, R_{OR} \ll 1$, so that for transmitting beams directed in the yz-plane (e.g., $\phi_{OT} = \pi/2$), we see that (6.44) can be further simplified to

$$2\hat{a}_0 - \underline{b}_{TR} \doteq \hat{i}_x (-\ell_{Tx}/R_{OT} - \ell_{Rx}/R_{OR}) + \hat{i}_y \left\{ (1 + R_{OT}/R_{OR}) \sin \theta_{OT} - \frac{L_O}{R_{OR}} \right\},$$

$$(\ell_{Ty} = 0). \quad (6.46)$$

Also, from (6.33) we have here \underline{b}_{TR} given by (6.33), with $\ell_{Ty} = 0$. Whether or not we can set $\underline{b}_{TR} \doteq 0$ in such expressions as (6.40), or even (6.39) and (6.43), will depend on the components of $\hat{\underline{B}}_{TR}$ and $\hat{\underline{D}}_M$, of course.

In the present experimental situation [6], where the receiving beam is omnidirectional, (6.20) applies for \underline{b}_{TR} , e.g.,

$$\left. \begin{aligned} \underline{b}_{TR} &= \hat{i}_x C + \hat{i}_y D; \quad \text{with } (\hat{a}_{OT} \cdot \underline{\ell}_T)_x = \ell_{Tx}; \\ (\hat{a}_{OT} \cdot \underline{\ell}_T)_y &= \ell_{Ty} \cos^2 \theta_{OT} + \ell_{Tz} \sin \theta_{OT} \cos \theta_{OT}, \end{aligned} \right\} \quad (6.47)$$

which can be further reduced on setting $\ell_{Ty} = 0$, cf. (6.45d).

C. Projected Beam Area on the Reference Wave Surface ($\langle \zeta \rangle = 0$)

From (6.17) et seq. it is clear that the composite beam pattern projected on the reference surface S_0 : $\langle \zeta \rangle = 0$ is a series of concentric ellipses, with the most intense beam levels occurring at $x = y = 0$, i.e., at O_S , cf. Fig. 5.1. Thus, if b^{-1} is the level of the beam pattern ($b > 1$) from the maximum, then the corresponding ellipse is described by

$$Ax^2 + By^2 = 2 \log b, \quad \text{from } b^{-1} = e^{-\frac{1}{2}(Ax^2 + By^2)}, \quad (6.48)$$

(where we have absorbed k_0^2 into A, B , so that $A, B = O(L^{-2})$ are inverse areas). Rewriting (6.48) as

$$\frac{x^2}{\left(\sqrt{\frac{2 \log b}{A}}\right)^2} + \frac{y^2}{\left(\sqrt{\frac{2 \log b}{B}}\right)^2} = 1, \quad \text{or} \quad \frac{x^2}{a_x^2} + \frac{y^2}{a_y^2} = 1, \quad (6.49)$$

we recall that the area of this ellipse (on $\langle \zeta \rangle = 0$) is

$$A_b = \pi a_x a_y, \quad (6.50)$$

so that we have directly from (6.49) in (6.50) here

$$A_b = \frac{2\pi \log b}{\sqrt{AB(\theta)}} \quad (6.51)$$

As we shall see presently (Sec. 8), the factor $2\pi/\sqrt{AB}$ shows up in the calculation of scattering intensities. From (6.51), accordingly, let us choose $b = e$, or $\log b = 1$, i.e., we select the e^{-1} level of pattern relative to its maximum:

$$A_1 = \frac{2\pi}{\sqrt{AB(\theta)}} \quad (6.52)$$

Thus, A_1 is the projected joint beam area on S_0 at the e^{-1} level. This particular analytic result, of course, stems from our original choice of gaussian beam pattern, cf. (6.5), (6.6), (6.17).

D. The Reference Surface Area, A_{REF}

The reference surface areas, A_{REF} , which are employed in the definition of the scattering cross sections (2.6), (2.19a,b), are arbitrary and may be chosen conveniently to simplify the result. In conventional practice (cf. [1]-[21], except [9]) the area A_{REF} on the reference plane S_0 : $\langle z \rangle = 0$ jointly "illuminated" by the projected beam patterns, Q_{RT} , is determined under the assumption that Q_{RT} , as projected, is uniform over the reference area and zero outside it. The associated area, A_{REF} , is such that $A_{REF} \gg \ell_g^2 (> \ell_{c,S}^2)$, where $\ell_g, \ell_{c,S}$ are respectively the correlation distances of the large- and small-scale wave surface components, cf. Sec. 3. Thus, since from (6.3), (6.17), and Sec. 6.3 above, we have specifically*

$$Q_{RT}|_{\text{on } S_0} = g_T g_R e^{-\frac{1}{2}(Ax^2 + By^2) + ik_0(Cx + Dy)}, \quad (6.53)$$

so that the beam-pattern integral $I_3(0)$, which appears in (8.1), (8.8), etc. for the calculation of $M_{\chi-\langle \chi \rangle}^{(0)}(0)$, cf. (2.6a), becomes

*With (6.17a,b) for A, ..., D, where we have absorbed the k_0^2 -factor into the A, B, which in turn now have the dimensions $[L^{-2}]$.

$$I_3(0) \Big|_{\text{uniform}} \equiv \int_{-\infty}^{\infty} |a_{RT}|^2 dr_1 = (g_T g_R)^2 A_{\text{REF}}: \text{uniform beams} \quad (6.54a)$$

$$= \frac{1}{2} (g_T g_R)^2 A_1: \text{gauss beams, (6.36)} \quad (6.54b)$$

Here $A_1 = 2\pi/\sqrt{AB(\theta)}$, (6.52), namely, the projected area on S_0 of the gaussian beam patterns, (2.11), (6.17), etc.

Similarly, we find that the associated integral [in (8.1)] becomes (with the help of (6.37))

$$I_2(2k_{0\alpha_0-xy}) \equiv \iint a_{RT}(r_1) a_{RT}(r_1 + \Delta r) e^{2ik_{0\alpha_0} \cdot \Delta r - \frac{1}{2} \Delta r \cdot D_M \cdot \Delta r} d(\Delta r)$$

$$= (g_T g_R)^2 A_{\text{REF}} \left(\frac{2\pi}{b_{0\sigma_{gy}}^2 \sigma_{gy}} \exp \left\{ -\frac{1}{2b_0^2} \left[\frac{(2\alpha_{ox})^2}{\sigma_{gx}^2} + \frac{(2\alpha_{oy})^2}{\sigma_{gy}^2} \right] \right\} \right)$$

(uniform beams) (6.55a)

$$= \frac{1}{2} A_1 (g_T g_R)^2 \frac{2\pi}{b_{0\sigma_{gy}}^2 \sigma_{gy}} \exp \left\{ -\frac{1}{2b_0^2} \left[\frac{(2\alpha_{ox})^2}{\sigma_{gx}^2} + \frac{(2\alpha_{oy})^2}{\sigma_{gy}^2} \right] \right\}$$

(gaussian beams). (6.55b)

Accordingly, our choice of reference area is

$$\boxed{A_{\text{REF}} = A_1/2} \quad (6.56)$$

here. As we see in Secs. 2.3-2.5, this brings our results into agreement with corresponding portions of earlier results, viz., various separate and joint determinations of the large-scale and small-scale scattering cross sections.

6.6 Summary Remarks

In Section 6 we have developed the rôle of the beam pattern in considerable analytic detail. Particular attention has been given to the gaussian pattern (6.3), because it approximates well the patterns produced by parametric transducers. Included also is the omni-directional

pattern, (6.8), (6.9), which is used in the receiver in the accompanying experiments [6]. The product beam patterns, Q_{TR} , are always "narrow-beam", from a combined choice of geometry [cf. Fig. 5.1] and injected signal waveform [cf. Sec. 6.3].

We note the following in summary:

- (1). Projections:
 - (i). $r_0 = 0$: axes of the beams coincide at O_S , cf. Fig. 5.1.
 - (ii). Elliptical beams, which are elliptical on $S(\langle z \rangle = 0)$. Here O_T, O_S, O_R form a plane perpendicular to the plane of S , e.g., $\phi_{OT} = 0, \pi/2$, and $\phi_{OR} = \pi/2, \pi$.
 - (iii). Since the receiving beam is omnidirectional in the experiments, we can relax the planar constraint of (ii) above, cf. footnote ff. Eq. (6.6).
 - (iv). The projected (composite) beam area on the reference surface $S_0(\langle z \rangle = 0)$ at the e^{-1} level vis-à-vis the maximum (at $x=y=0$) is $A_1 = 2\pi/\sqrt{AB}$, cf. (6.52).
- (2). Narrow-Beams (N.B.): this requires far-field geometries and possibly gated (modulated) carriers [Sec. 6.3].
- (3). Explicit dependence of beam patterns on frequency [Sec. 6.2].
- (4). Explicit results for N.B. cases in the forward and backscatter régimes [Sec. 6.3].
- (5). Concept of "effective bandwidth" [Sec. 6.3].
- (6). The rôle of the Fourier transform of the beam pattern with the driving signal spectrum [Sec. 6.4], or when beam and signal waveform are factorable, cf. (6.29). (The gated signal should not be so short, i.e., its spectrum so broad, that (spectral) factorization is not possible. "Beam-scanning" of the (wave) surface is automatically accounted for here.)
- (7). Various beam integrals needed in the evaluation of scatter intensities are carried out [Sec. 6.5], which include the effects of the phase terms in the complex beam patterns, cf. (6.3).

In general, the above results are independent of propagation and geometry provided

- (i). the medium is not dispersive, e.g., $f_0 < o(40 \text{ kHz})$, only absorptive at worst;
- (ii). $\nabla c \doteq 0$: negligible velocity gradients. [However, the effects of $\nabla c \neq 0$ can be accounted for by suitable reconfiguration into an equivalent geometry--to be considered in a later study.]
- (iii). far-field conditions are valid, so that one can speak properly of beam patterns, i.e., Fresnel corrections are negligible.

With the results of Section 6 we are now able to obtain explicit expressions for the desired scatter intensities [Sec. 8], once the appropriate local scattering model is implemented [Sec. 7 ff.]. See also Section 5.5 for a summary of the basic structural conditions.

7. Surface Models: General Scatter Intensity

From (5.26) in (5.20), (5.21) we can now write the received waveforms $X(t)$ whose intensities we wish to determine for the back- and forward-scatter cross sections which are the principal aim of the present study. Specifically, we have (the complex) waveform

$$X(t) = \sum_{k=0}^{\infty} X^{(k)}(t) = \sum_{k=0}^{\infty} A_0 \int_{Br_1} S_{in}(s/2\pi i) F_S^{(k)}(s|\zeta(r,t), \dots | f_0) e^{st} \frac{ds}{2\pi i}, \quad (7.1)$$

where the Total Surface Spreading Function (TSSF) $F_S^{(k)}$ is now

$$F_S^{(k)} = \int_{S_0} A_{RTQ}^{(k)}(\underline{r}', t') e^{-a\omega_0^2 c_0 T_0 - \frac{s}{c_0}[(\underline{r} + \underline{\zeta}) \cdot 2\underline{\alpha}_0 + c_0 T_0]} \frac{dx dy}{(4\pi)^2 R_{OT} R_{OR} n_z} \quad (7.2)$$

subject to the various approximations and assumptions noted in Secs. 5.5, 6.6 above. The beam pattern product A_{RT} is given explicitly by (6.17), (6.31) here, cf. Remarks in Sec. 6.2 also, and $t' = t - \Delta t_{dS}$, $\underline{r}' = \underline{r} + \underline{\zeta}$, cf. (5.22a,b).

AD-A145 672

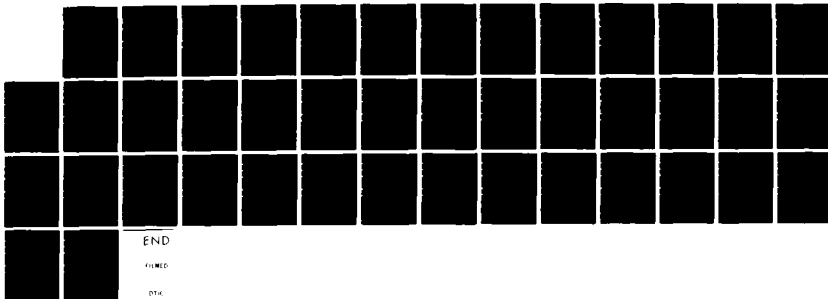
ACOUSTIC SCATTERING CROSS SECTIONS FOR TRULY COMPOSITE
WIND-WAVE SURFACES. (U) MIDDLETON (DAVID) NEW YORK
D MIDDLETON 20 AUG 84 NUSC-TD-7205 N00140-83-M-NA11

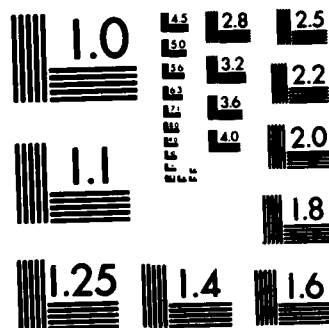
2/2

UNCLASSIFIED

F/G 20/1

NL





MICROCOPY RESOLUTION TEST CHART
NATIONAL BUREAU OF STANDARDS-1963-A

7.1 Wave Surface Models

As before, cf. Sections 2.1, 3.1, we shall employ a two-component wave surface model, consisting of the single gravity-capillary wave surface as one component (G), on which rides the soliton-ripple contribution (S), as sketched in Fig. 2.1 above. For later analytical convenience (cf. Sec. 8.6) we shall in addition split the former surface into a sum of large-scale "gravity" (G) and small-scale "capillary" (S) contributions, so that the surface elevation at (\underline{r}, t) on the reference surface, (S_0) is, in detail,

$$\underline{\zeta}(\underline{r}, t) = \hat{\underline{i}}_z [\zeta_g(\underline{r}, t) + \zeta_c(\underline{r}, t)] + \hat{\underline{n}}_G(\underline{r}, t) \zeta_S(\underline{r}, t) ; \text{ with } \zeta_g = \hat{\underline{i}}_z \zeta_g, \zeta_S = \hat{\underline{n}}_G \zeta_S \quad (7.3)$$

where $\hat{\underline{n}}_G$ is the normal to the G (= g + c) surface, viz.

$$\hat{\underline{n}}_G = \{ (\hat{\underline{i}}_x \zeta_x + \hat{\underline{i}}_y \zeta_y - \hat{\underline{i}}_z) n_z \}_G = \left(\frac{\hat{\underline{i}}_x \zeta_x + \hat{\underline{i}}_y \zeta_y - \hat{\underline{i}}_z}{\sqrt{1 + \zeta_x^2 + \zeta_y^2}} \right)_G, \quad \zeta_x \equiv \frac{\partial \zeta}{\partial x}, \text{ etc.} \quad (7.4a)$$

However, for the present we use the two-component composite surface

$$\underline{\zeta}(\underline{r}, t) = \hat{\underline{i}}_z \zeta_G(\underline{r}, t) + \hat{\underline{n}}_G(\underline{r}, t) \zeta_S(\underline{r}, t), \quad (7.4b)$$

reserving to Sec. 8.6 ff. the further dichotomy of ζ_G into a "gravity" (g) and a "capillary" (c) component.

In our alternative approach, as noted in Sec. 5.4 above, we obtain the following specific results for surface operator kernels $Q_S^{(k)}$ ([41], II):

$$(k=0): \quad Q_S^{(0)} = \left. \Gamma^{(0)} \right|_{\Sigma} \equiv \gamma_0^{(0)} \langle v^{(0)} \rangle_R \Big|_{\Sigma} \doteq R_0 S \hat{\underline{n}} \cdot (\hat{\underline{i}}_T - \hat{\underline{i}}_R) \frac{s}{c_0} \Big|_{\Sigma} \quad (7.5)$$

and

$$(k \geq 1): \quad Q_S^{(k)} = \gamma_{og}^{(k)} \Delta v_G^{(k)} + \gamma_{oS}^{(k)} \Delta v_S^{(k)} = (\hat{\underline{i}}_z \cdot \underline{\zeta}_G) \Delta v_G^{(k)} R_0 S \Big|_g + (\hat{\underline{i}}_z \cdot \underline{\zeta}_S) \Delta v_S^{(k)} R_0 S \Big|_c \quad (7.6)$$

Here R_0 is a plane-wave reflection coefficient (for the water-air interface) and S is a shadowing function ($0 \leq S \leq 1$), whose statistical properties we shall comment upon presently, cf. Sec. 7.7, § ff. The subscripts g, c indicate the (moving) surface upon which the quantities in question are to be evaluated. Our specific result (7.5) is based on the Tangent Plane (T.P.), or Kirchhoff approximation, cf. Chapter 7, Sections 19, 20, [1], in particular, the discussions in Sec. 19.2. (See also, Bahar [23].) In (7.6) the $\Delta v^{(k)}$ are the fluctuations in the densities of the respective k -coupled scattering elements on Σ_g and Σ_c . [A full treatment of the cases $k \gg 1$ is described in Middleton [41, II, III].

Applying (7.5) to (7.2) then gives us directly for the TSSF

$$(k=0): F_S^{(0)} = \frac{e^{-\alpha \omega_0^2 c_0 T_0}}{(4\pi)^2 R_{0T} R_{0R}} \int_{S_0} \frac{S}{c_0} \left[R_0 S \frac{\hat{n} \cdot (\hat{i}_{0T} - \hat{i}_{0R})}{n_z} \right]_{G+S} \cdot Q_{RT} e^{-(s/c_0)[(\underline{r} + \underline{\xi}) \cdot 2\underline{\alpha}_0 + c_0 T_0]} dx dy, \quad (7.7)$$

where all the conditions and approximations of Sec. 5.5 above are in force. The result (7.7), with (7.1), is a generalization of Tolstoy and Clay ([9], Eq. (6.19), before integration by parts therein, cf. (7.27) ff. also), with the inclusion of one or more of the following:

- (i). doppler, in $\underline{\xi}(\underline{r}, t')$;
- (ii). general apertures;
- (iii). general narrow band signals;
- (iv). shadowing;
- (v). absorption.

(7.7a)

Similarly, we find from (7.6) in (7.2) that the TSSF for the diffraction terms ($k \geq 1$) is

$$(k \geq 1): F_S^{(k \geq 1)} = \frac{e^{-\alpha \omega_0^2 c_0 T_0}}{(4\pi)^2 R_{0T} R_{0R}} \int_{S_0} Q_{RT} \left\{ (R_0 S (\hat{i}_z \cdot \underline{\xi}_G) \Delta v_G^{(k)} / n_G) + (R_0 S (\frac{\hat{i}_z \cdot \underline{\xi}_S}{n_z}) \Delta v_S^{(k)}) \right\}_{G+S} \cdot e^{-(s/c_0)[(\underline{r} + \underline{\xi}) \cdot 2\underline{\alpha}_0 + c_0 T_0]} dx dy, \quad (7.8)$$

where, as above, $\underline{\xi}$ is given by (7.3).

7.2 The Second-Moment Functions of the Received Scattered Field, $X(t)$

The second-moment function of the received scattered field is the sum of the ($k \geq 0$) second-moment functions, viz.

$$M_X(\tau) = \sum_{k=0}^{\infty} M_X^{(k)}(\tau) = \sum_{k=0}^{\infty} \frac{1}{2} \operatorname{Re} \overline{\langle X^{(k)}(t_1) X^{(k)}(t_2) \rangle_{\phi}}, \quad \tau = t_2 - t_1, \quad (7.9)$$

since all $k (\geq 0)$ components of X , cf. (7.1), are statistically independent and postulated here to be stationary, as well. [The averages $\langle \rangle_{\phi}$ are over the epochs of the injected signal.]

Since $S_{in}(s/2\pi i) \rightarrow S_{in}(s/2\pi i | \phi)$ here in (7.1), and since

$$\langle S_{in}(s_1/2\pi i | \phi) S_{in}(s_2/2\pi i | \phi)^* \rangle_{\phi} = |S_{in}(s_1/2\pi i)|^2 \delta\left(\frac{s_2^* + s_1}{2\pi i}\right), \quad (7.10)$$

with the signal independent of the scatter, we readily find on applying (7.1), with (7.7), (7.8), to (7.9), that the various second-moment functions of the received scattered field are now specifically:

A. Total "Classical" Component $k = 0$:

$$(k=0): M_X^{(0)}(\tau) = \operatorname{Re} \{ G^{(1)} K_0^2(\tau)_{in} e^{-i\omega_0 \tau} M_{RT}^{(0)}(\tau | f_0, \underline{\alpha}_0 | \underline{\zeta}) \}, \quad (7.11)$$

where

$$G^{(1)} \equiv \frac{e^{-2a\omega_0^2 c_0 T_0}}{(4\pi)^4 R_0^2 T_0 R_0^2} \text{ ("geometric," or spreading factor);} \quad (7.11a)$$

$$K_0(\tau)_{in} \equiv \int_{-\infty}^{\infty} w_{in}(f') e^{-i\omega' \tau} df'; \quad w_{in}(f') \equiv \frac{A_0^2}{2} |S_{in}(f')|^2; \quad (f' = f - f_0) \\ \text{for narrow band signals;} \quad (7.11b)$$

and, for the present,

$$M_{RT}^{(0)}(\tau | f_0, \underline{\alpha}_0 | \underline{\zeta}) \equiv \int_{-\infty}^{\infty} A_{RT}(\underline{r}_1 | f_0) d\underline{r}_1 \int_{-\infty}^{\infty} A_{RT}(\underline{r}_1 + \underline{\Delta r} | f_0)^* e^{ik_0 \underline{\alpha}_0 \cdot \underline{\Delta r}} \\ \cdot \left\langle R_{01} R_{02} S_1 S_2 \right\rangle_{G+S} \left\langle \left(\frac{\hat{n}_1 \cdot 2\underline{\alpha}_0}{n_{z1}} \right) \left(\frac{\hat{n}_2 \cdot 2\underline{\alpha}_0}{n_{z2}} \right) \right\rangle_{G+S} e^{2ik_0 \underline{\alpha}_0 \cdot (\underline{\zeta}_2 - \underline{\zeta}_1)} \Bigg|_{\zeta_1, \dots, \zeta_{x1}, \dots} d(\underline{\Delta r}) \quad (7.11c)$$

where $\underline{r} = \underline{r}_2 - \underline{r}_1$, $\tau = t_2 - t_1$, and here the composite wave surface ζ , (7.3), is represented explicitly by

$$\zeta_1 = \zeta(\underline{r}_1, t_1 - R_{R_1}/c_0); \quad \zeta_2 = \zeta(\underline{r}_1 + \underline{\Delta r}, t_1 + \tau - R_{R_2}/c_0); \quad R_R/c_0 = (R_{OR} - \hat{i}_{OR} \cdot \underline{r})/c_0, \quad (7.12)$$

this last from (5.22i), including doppler, where also we note again the time-dependence of ζ . In (7.11c) we have made the further assumption that the shadowing and reflection coefficients are essentially independent of the surface elevation here. As the exhaustive analysis of Bass and Fuks shows ([1], Sections 22, 23), this is reasonable: the shadowing function depends only on the statistics of the slopes of the surface, in the case of the intensity calculations here, cf. [1], 5, p. 297. This is also approximately true for mean amplitudes, $\langle X \rangle$, as long as the shadowing is not too heavy, [1], 5, p. 297 again.

B. The Coherent Component ($k = 0$):

Our result (7.11) includes the *coherent component*, $\langle X \rangle$, if any, of the received scattered field. [We exclude throughout any direct (coherent) propagation, cf. Fig. 5.1. This is very easily added, if needed.] The second-moment function for $\langle X \rangle$ is readily obtained on setting $\tau \rightarrow \tau + t_0$ in (7.11), etc., and letting $t_0 \rightarrow \infty$. The result is

$$(k=0): \quad M_{\langle X \rangle}^{(0)}(\tau) = \text{Re} \{ G^{(1)} k_0^2 K_0(\tau) \text{in} e^{-i\omega_0 \tau} M_{RT}^{(0)}(\infty | f_0, \underline{\alpha}_0 | \zeta) \}, \quad (7.13)$$

with now

$$M_{RT}^{(0)}(\infty | \dots) = \left| \left\langle \left(\frac{\hat{n} \cdot \underline{\alpha}_0}{n_z} \right)_{G+S} e^{2k_0 i \underline{\alpha}_0 \cdot \underline{\zeta}} \right\rangle \right|^2 A_{RT}(\underline{\alpha}_0), \quad (7.13a)$$

and

$$A_{RT}(\underline{\alpha}_0) \equiv \int_{-\infty}^{\infty} Q_{RT}(\underline{r}_1 | f_0) \langle (R_{01} S_1)_{\Sigma} \rangle d\underline{r}_1 \int_{-\infty}^{\infty} Q_{RT}(\underline{r}_1 + \underline{\Delta r} | f_0)^* \langle (R_{02} S_2)_{\Sigma=G+S} \rangle \cdot e^{2ik_0 \underline{\alpha}_0 \cdot \underline{\Delta r}} d(\underline{\Delta r}). \quad (7.13b)$$

Equation (7.13a) follows from (7.11c) (as $t_0 \rightarrow \infty$) because we have made the usual reasonable assumption that the random wave surface (as an ensemble) is stationary and homogeneous (i.e., independent of (r_1, t_1)), at least over periods comparable to the signal duration.

From (7.12) and (7.13) it follows that the total second-moment function consists of the sum of an incoherent and an (independent) coherent part:

$$(k=0): M_X^{(0)}(\tau) = M_{X-\langle X \rangle}^{(0)}(\tau) + M_{\langle X \rangle}^{(0)}(\tau), \quad (7.14)$$

where now, specifically,

$$(k=0): M_{X-\langle X \rangle}^{(0)}(\tau) = \text{Re} \{ G^{(1)} k_0^2 K_0(\tau) \text{in} e^{-i\omega_0 \tau} [M_{RT}^{(0)}(\tau | \dots) - M_{RT}^{(0)}(\infty | \dots)] \}. \quad (7.14a)$$

Eq (7.11c) Eq. (7.13a)

C. Higher-Order (Diffraction) Terms ($k \geq 1$):

In a similar way we obtain the second-moment functions for the diffraction components ($k \geq 1$), with the help of (7.8) in (7.1) and (7.9). We have directly

$$(k \geq 1): M_X^{(k)}(\tau) = M_{X-\langle X \rangle}^{(k)}(\tau) = \text{Re} \left\{ \frac{e^{-2a\omega_0^2 c_0 T_0}}{(4\pi)^4 R_{OT}^2 R_{OR}^2} K_0(\tau) \text{in} e^{-i\omega_0 \tau} M_{RT}^{(k)}(\tau | f_0, \alpha_0 | \zeta) \right\}, \quad (7.15)$$

where specifically

$$M_{RT}^{(k)}(\tau | \dots) = \int_{-\infty}^{\infty} \int Q_{RT}(r_1 | f_0) Q_{RT}(r_1 + \Delta r | f_0)^* e^{ik_0 2\alpha_0 \cdot \Delta r} \cdot \left\langle \left[R_{OS} \frac{(\hat{i}_z \cdot \xi_G)^{\Delta v_G(k)}}{n_z} \right]_G + \left[R_{OS} \frac{(\hat{i}_z \cdot \xi_S)^{\Delta v_S(k)}}{n_z} \right] \right\rangle_{G+S} \cdot \left(\left[R_{OS} \frac{(\hat{i}_z \cdot \xi_G)^{\Delta v_G(k)}}{n_z} \right]_G + \left[R_{OS} \frac{(\hat{i}_z \cdot \xi_S)^{\Delta v_S(k)}}{n_z} \right] \right)_{G+S} \cdot e^{ik_0 2\alpha_0 \cdot (\xi_2 - \xi_1)} \Delta r_1 d(\Delta r), \quad (7.16)$$

and the averages are carried out over all random variables: ζ_G , ζ_S , ζ_{Gx} , etc., R_0 , etc. [The averages over the reflection and shadowing coefficients (R_0, S) are independent here of the other averages, as noted earlier, cf. (7.12) et seq., above.] Since these diffraction components can contain no coherent components--these are observed only in the "classical" ($k=0$) case, cf. (7.14)--we have written $M_X^{(k)}(\tau) = M_{X-\langle X \rangle}^{(k)}(\tau)$, $k \geq 1$, in (7.15). Generally, these diffraction terms ($k \geq 1$) are comparatively small, vis-à-vis the classical components ($k=0$), except possibly for certain transmitter-receiver geometries and directional wave spectra where the classical components may vanish. [See the remarks in Sec. 3.]

7.3 Explicit Surface Scatter Statistics: Two-Scale Models

Before we evaluate $M_{RT}^{(k \geq 0)}$ in the above expressions for the second moment functions, let us introduce an approximation for $(\hat{n}/n_z)_{G+S}$, cf. (7.7), (7.11c), (7.13a).

Let $\hat{\Sigma}_G$ be the surface expansion operator of a truly two-scale surface, where the second-scale surface here is $\hat{n}_G \zeta_S$, cf. Fig. 2.1, which rides on the single gravity-capillary wave surface, $\hat{z} \zeta_G$, cf. (7.46). Thus, we can write

$$\hat{\Sigma}_G = \{ \hat{1} + \zeta_S \hat{n}_G \cdot \nabla_r + \frac{\zeta_S^2}{2} (\hat{n}_G \cdot \nabla_r)^2 + \dots \} \quad (7.17)$$

provided $\langle |\hat{n}_G \cdot \nabla_r|^2 \zeta_S^2 \rangle < 1$, so that the series is (stochastically) convergent (at all \underline{r}, t). Physically, this means that $\langle |\hat{n}_G \cdot \nabla|^2 \rangle < \infty$ and $\langle \zeta_S^2 \rangle < 1$, (m.s.), which is not difficult to achieve here. Accordingly, applying (7.17) to $\hat{n}/n_z|_{G+S}$ gives

$$(\hat{n}/n_z)_{G+S} = \hat{\Sigma}_G (\hat{n}/n_z)_G = (\hat{n}/n_z)_G + \zeta_S \hat{n}_G \cdot \nabla (\hat{n}/n_z)_G + \dots \doteq (\hat{n}/n_z)_G, \quad (7.18)$$

since

$$\hat{n}_G \cdot \nabla_r \left(\frac{\hat{n}}{n_z} \right)_G = \left\{ \frac{\hat{i}_x (\zeta_x \zeta_{xx} + \zeta_y \zeta_{xy}) + \hat{i}_y (\zeta_x \zeta_{xy} + \zeta_y \zeta_{yy})}{\sqrt{1 + \zeta_x^2 + \zeta_y^2}} \right\}_G = O \left(\frac{\sqrt{\frac{2}{\sigma_x^2} + \frac{2}{\sigma_y^2}}}{1 + \sigma_x^2 + \sigma_y^2} \right)_G, \quad (7.18a)$$

so that

$$\langle [\zeta_S \hat{n}_G \cdot \nabla \left(\frac{\hat{n}}{n_z} \right)_G]^2 \rangle^{\frac{1}{2}} = O(\sigma_S \sigma_{Gx} \sigma_{Gxx}) = O(10^{-4} \cdot 10^0 \cdot 10^{0,1}) = O(10^{-4}, 10^{-3}) \ll 1.$$

A. The Coherent Component (k=0)

Next, let us consider (7.13a) and note that the Rayleigh number, $[k_0 \sigma_S (\cos \theta_{OT} + \cos \theta_{OR})]^2$ is usually small compared to unity for the soliton-waves. Thus, using (7.18) and (7.3) or (7.4b) we can write

$$M_{RT}^{(0)}(\infty | \dots) \doteq \left| \left\langle \left(\frac{\hat{n} \cdot 2\alpha_0}{n_z} \right)_G e^{2ik_0 \alpha_{0z} \zeta_G} (1 + 2ik_0 \alpha_0 \cdot \hat{n}_G \zeta_S - \frac{k_0^2}{2} (2\alpha_0 \cdot \hat{n}_G)^2 \zeta_S^2 + \dots) \right\rangle^2 \right| A_{RT}. \quad (7.19)$$

First, we note that for ζ_G a gaussian random process, ζ_G and its (first) derivatives are statistically independent, so that $\exp(2ik_0 \alpha_{0z} \zeta_G)$ and $(\hat{n} \cdot 2\alpha_0)/n_z)_G$ are likewise independent. Second, to a good approximation we may treat the gravity and soliton-ripple waves as statistically independent.* Using (7.20) and the fact that $(\hat{n} \cdot 2\alpha_0)/n_z)_G = 2\alpha_{0x} \zeta_{Gx} + 2\alpha_{0y} \zeta_{Gy} - 2\alpha_{0z}$, we see that (7.19) reduces directly to

$$M_{RT}^{(0)}(\infty | \dots) = |F_1(2\alpha_0 k_0)_G (-2\alpha_{0z} + \frac{k_0^2}{2} \sigma_S^2 \hat{N}_{GS}^{(0)} + \dots)|^2 A_{RT}, \quad \sigma_S^2 = \overline{\zeta_S^2} \quad (7.20)$$

since $\overline{\zeta_x} = \overline{\zeta_y} = 0$, etc., where

$$F_1(2\alpha_0 k_0)_G = \langle e^{2ik_0 \alpha_{0z} \zeta_G} \rangle = \text{characteristic function of } (-\zeta_G); \quad (7.21)$$

and, with the help of (7.4), we see at once that

$$\hat{N}_{G\text{-coh}}^{(0)} \equiv \left\langle \left(\frac{\hat{n} \cdot 2\alpha_0}{n_z} \right) (\hat{n}_G \cdot 2\alpha_0)^2 \right\rangle_G = \left\langle \frac{(2\alpha_{0x} \zeta_x + 2\alpha_{0y} \zeta_y - 2\alpha_{0z})^3}{1 + \zeta_x^2 + \zeta_y^2} \right\rangle_G. \quad (7.22)$$

This latter may be considerably simplified if we remember that ζ_{Gx} , ζ_{Gy} obey a symmetrical pdf (since ζ_G is likewise symmetrically distributed. Then (7.22) reduces to

*Of course, this is not strictly true, as the configuration of the large-scale waves influences the local wind action which produces the ripple structures which ride upon them, [16].

$$\hat{N}_{G\text{-coh}}^{(0)} = -8\alpha_{oz} \left\langle (6\zeta_{Gx}^2 \alpha_{ox}^2 + 6\zeta_{Gy}^2 \alpha_{oy}^2 + \alpha_{oz}^2) / (1 + \zeta_{Gx}^2 + \zeta_{Gy}^2) \right\rangle_G \equiv -2\alpha_{oz} N_{G\text{-coh}}^{(0)}, \quad (7.22a)$$

so that (7.21) becomes

$$M_{RT}^{(0)}(\infty|\dots) \doteq |2\alpha_{oz} F_{1G} [1 + \frac{k_{oS}^2}{2} N_{G\text{-coh}}^{(0)} + \dots]|^2 A_{RT}(\alpha_o) \quad (7.23a)$$

$$\doteq (2\alpha_{oz})^2 A_{RT} |F_{1G}|^2 e^{k_{oS}^2 N_{G\text{-coh}}^{(0)}}, \quad (k_{oS}^2 \ll 1), \quad (7.23b)$$

generally, the latter when $k_{oS}^2 N_{G\text{-coh}}^{(0)} \ll 1$, as it usually is. This [Eq. (7.23)] is a new result, for general beam patterns where (7.13b) gives A_{RT} , where specifically now

$$N_{G\text{-coh}}^{(0)} \equiv 4 \left\langle \frac{6\zeta_x^2 \alpha_{ox}^2 + 6\zeta_y^2 \alpha_{oy}^2 + \alpha_{oz}^2}{1 + \zeta_x^2 + \zeta_y^2} \right\rangle_G. \quad (7.24)$$

is the coherent "tilt-factor." This result is to be compared with (6.43), p. 205 and (6.41a) of [9]. Here we have the additional effects of the tilted ripple surface (ζ_s), which somewhat further decrease coherence. But since $k_{oS}^2 N_{G\text{-coh}}^{(0)}$ is small compared to unity, we can usually set the exponential equal to one in (7.23b). Also, in place of the angular illumination function $f(\theta)$, (6.25) [9] we have $2\alpha_{oz}$ ($= -2\gamma_{T+C}$), as a result of the direct evaluation of (7.7) in (7.19).

The beam pattern function, A_{RT} , insures a vanishingly small value of $M_{RT}^{(0)}(\infty|\dots)$ for scatter angles off the specular direction, since from (7.13b) and (6.39) specifically,

$$A_{RT} \doteq (\bar{R}_0 \bar{S})^2 \frac{(g_T g_R)^2 2\pi^2}{k_{oAB}^2} \exp \left(-\frac{3}{4} k_o^2 \left[\left(\frac{2\alpha_{ox} - b_{TRx}}{A} \right)^2 + \left(\frac{2\alpha_{oy} - b_{TRY}}{B} \right)^2 \right] \right), \quad (7.25)$$

(where we have absorbed the k_o^2 -factor into the A, B's (and k_o into b_{TR}), e.g., A_T, A_R are $O(L^2)$, viz., are effective aperture areas now, cf. 1a of

Sec. 6.5; also note the factor k_0^2 in the exponent now). We have replaced $(\bar{R}_0 \bar{S})_Z$ by $\bar{R}_0 \bar{S}$ (referred to the reference plane, S_0 , of the gravity wave component) with the help of (7.17), using the fact that $|\langle \zeta_S \hat{n}_G \cdot \nabla R_0 S \rangle| \ll 1$, cf. (7.18a). Since $A^{-1} = (R_{OT}^2/A_T + R_{OR}^2/A_R)$, cf. (6.32a,b), is large, only when $2\alpha_{ox} - b_{TRx}$, etc. is small will A_{RT} not effectively vanish. (Here we use (6.44)-(6.46) for $2\alpha_{ox} - b_{TR}$ in various configurations.) Thus, for the near-specular directions only does A_{RT} differ from zero significantly.

Furthermore, for the gaussian gravity wave surface we have specifically the familiar result

$$F_{1G} = \langle e^{2ik_0 \alpha_{oz} \zeta_G} \rangle = e^{-2k_0^2 \sigma_G^2 \alpha_{oz}^2}. \quad (7.26)$$

As expected, for rough surfaces $(2k_0 \sigma_G \alpha_{oz})^2 \gg 1$, $F_{1G} \rightarrow 0$ and the coherent component vanishes.

B. The Incoherent Component ($k=0$)

Our next concern is the incoherent component (7.14a), for which we need now $M_{RT}^{(0)}(\tau|\dots)$, Eq. (7.11c). At this point we can simplify (7.11c) by the following series of modifications:

- 1). We begin by expanding the exponential term in (7.11c), using (7.3) viz.:

$$\begin{aligned} e^{2ik_0 \alpha_{ox} (\zeta_2 - \zeta_1)} &= e^{2ik_0 \alpha_{oz} (\zeta_{2G} - \zeta_{1G})} [1 + 2ik_0 \alpha_{ox} \cdot (\hat{n}_{2G} \zeta_{2S} - \hat{n}_{1G} \zeta_{1S}) \\ &\quad + k_0^2 (2\alpha_{ox} \cdot \hat{n}_{G1})(2\alpha_{ox} \cdot \hat{n}_{G2}) \zeta_{2S} \zeta_{1S} - k_0^2 (2\alpha_{ox} \cdot \hat{n}_G \zeta_S)^2 + \dots]. \end{aligned} \quad (7.27a)$$

Using the postulated homogeneity and stationarity of each component of the wave surface, we get

$$\begin{aligned} e^{2ik_0 \alpha_{ox} (\zeta_2 - \zeta_1)} &= e^{2ik_0 \alpha_{oz} (\zeta_{2G} - \zeta_{1G})} [e^{-k_0^2 (2\alpha_{ox} \cdot \hat{n}_G)^2 \zeta_S^2} \\ &\quad + 2ik_0 \alpha_{ox} \cdot (\hat{n}_{G2} \zeta_{2S} - \hat{n}_{G1} \zeta_{1S}) + k_0^2 (2\alpha_{ox} \cdot \hat{n}_{1G})(2\alpha_{ox} \cdot \hat{n}_{2G}) \zeta_{2S} \zeta_{1S} + \dots]. \end{aligned} \quad (7.27b)$$

2). Next, we reinsert the factors $(\hat{n} \cdot 2\alpha_0)/n_z)_G$ back into the integrand of A_{RT} in (7.11c) and then integrate each factor in A_{RT} by parts (one over r_1 and one over \underline{r} with r_1 held fixed, since ζ_G, ζ_S are stationary and homogeneous here, in the manner of p. 198 of [9], but only for the leading term of the series (7.27b), to achieve the desired simplification. When the "illuminated" portion of the surface is large compared to (the square of the [acoustic]) wavelength, e.g., $\Lambda_S \gg \lambda_0^2$, or $k_0^2 \Lambda_S \gg 1$, or more precisely $k_0^2 A_1 \gg 1$, cf. (6.52), we can neglect the terms containing the derivatives of the beam patterns. The result is, for the first term in (7.27b), where we use also (7.18):

$$\left(\frac{\hat{n}_1 \cdot 2\alpha_0}{n_{z1}}\right)_G \left(\frac{\hat{n}_2 \cdot 2\alpha_0}{n_{z2}}\right)_G e^{2ik_0 \alpha_0 \cdot (\zeta_{2G} - \zeta_{1G})} = \left[\frac{\alpha_{0x}^2 + \alpha_{0y}^2 + \alpha_{0z}^2}{\alpha_{0z}^2} \right]^2 e^{2i\alpha_0 k_0 (\zeta_{2G} - \zeta_{1G})}, \quad (7.27c)$$

$k_0^2, A_1 \gg 1.$

We emphasize that Eq. (7.27c), et seq., applies basically in the "high-frequency" régimes, where $(2k_0 \alpha_{0z} \sigma_G)^2 \gg 1$. In the alternative "low-frequency" cases $(2k_0 \alpha_{0z} \sigma_G)^2 \ll 1$, however, we may approximate the normal factor (\hat{n}) by writing

$$\left(\frac{\hat{n} \cdot 2\alpha_0}{n_z}\right)_G \doteq -2\alpha_{0z} \quad (7.27d)$$

since the slopes (ζ_{Gx}, ζ_{Gy}) are here small. This is Eckart's approximation [32]. Then, integration by parts is not required.

3). Applying (7.27c) to (7.27b) in (7.11c) allows us to write for the factors averaged over the various surface components $\zeta_{G1}, \zeta_{Gx}, \dots$ etc:*

*This procedure is equivalent to a direct expansion of the exponential containing the soliton-ripple component in (7.7) and then integrating $[\hat{n} \cdot (\hat{i}_{0T} - \hat{i}_{0R})/n_z]_{G+S \doteq G}$ by parts for the first term of the resulting series, where again we require $\Lambda_S k_0^2 \gg 1$, or $k_0^2 A_1 \gg 1$, cf. [9], p. 198. This is then followed by the indicated calculation of the second-moment in question.

$$\langle \rangle_{\zeta_{1G}} \doteq \left[\frac{\alpha_{0x}^2 + \alpha_{0y}^2 + \alpha_{0z}^2}{\alpha_{0z}/2} \right]^2 F_{2G} + \langle e^{2k_0 i \alpha_0 \cdot (\zeta_{2G} - \zeta_{1G})} \rangle \quad (7.28)$$

$$\cdot k_0^2 (\hat{n}_1 \cdot 2\alpha_0 / n_{z1})_G (\hat{n}_2 \cdot 2\alpha_0 / n_{z2})_G (2\alpha_0 \cdot \hat{n}_{1G}) (2\alpha_0 \cdot \hat{n}_{2G}) \zeta_{2S} \zeta_{1S} + \dots >_{G,S}$$

where specifically we replace the (interior) exponential term in the series (7.27b) by unity, since here $4k_0^2 (\alpha_0 \cdot \hat{n}_z)^2 \zeta_S^2 \ll 1$, and where now

$$F_{2G} = F_2(-2i\alpha_{0z}k_0, 2i\alpha_0k_0)_G = \exp \{ -b_0^2 k_0^2 \sigma_G^2 [1 - \rho_G(\Delta \underline{r}, \tau + \Delta \underline{r} \cdot \hat{j}_{0R}/c_0)] \}, \quad (7.29)$$

$$\sigma_G^2 = \langle \zeta_G^2 \rangle; \quad b_0 = \cos \theta_{OT} + \cos \theta_{OR},$$

is the second-order characteristic function of the gaussian gravity-wave component. Here ρ_G is the normalized directional space-time covariance function of ζ_G , viz.

$$\sigma_{G^2}^2 \equiv K_G(\Delta \underline{r}, \tau + \Delta \underline{r} \cdot \hat{j}_{0R}/c_0) = \int_{-\infty}^{\infty} \int \zeta_{1G} \zeta_{2G} w_2(\zeta_{1G}, \zeta_{2G}; \Delta \underline{r}, \tau) d\zeta_{1G} d\zeta_{2G}, \quad (7.30)$$

where, of course, $\langle \zeta_G \rangle = \langle \zeta_{G,S} \rangle = 0$. The quantity $\Delta \underline{r} \cdot \hat{j}_{0R}/c_0$ represents a doppler delay produced by the moving surface [34], (a delay which we can usually ignore henceforth).

4). Since the correlation distance, ℓ_G , for the large-scale surface, $\rho_G(\ell_G, \dots) \equiv e^{-1}$, is large vis-à-vis ℓ_S , $\rho(\ell_S, \dots) = e^{-1}$, for the small-scale surface, e.g., $\ell_G \gg \ell_S$, so that $\zeta_{2G} \doteq \zeta_{1G}$ for all $\Delta \underline{r} \sim \ell_S (\ll \ell_G)$, we may set $\zeta_{2G} \doteq \zeta_{1G}$ in (7.28). The result is

$$\langle \rangle_{\zeta_{1G}} \doteq \left(\frac{\alpha_{0x}^2 + \alpha_{0y}^2 + \alpha_{0z}^2}{\alpha_{0z}/2} \right)^2 F_{2G} + k_0^2 \left\langle \left(\frac{2\alpha_0 \cdot \hat{n}}{n_z} \right)_G^2 (2\alpha_0 \cdot \hat{n})_G^2 \right\rangle K_S(\Delta \underline{r}, \tau + \dots), \quad (7.31)$$

$$k_0^2 A_1 \gg 1,$$

where in more compact form we write

$$\langle \rangle_{\zeta_G} \doteq \left(\frac{\alpha_{ox}^2 + \alpha_{oy}^2 + \alpha_{oz}^2}{\alpha_{oz}} \right)^2 F_{2G} + k_o^2 N_{G-inc}^{(0)}(\underline{\alpha}_o) K_S, \quad (\ell_G \gg \ell_S) \quad (7.31a)$$

with now

$$N_{G-inc}^{(0)}(\underline{\alpha}_o) \equiv \left(\frac{2\underline{\alpha}_o \cdot \hat{n}}{n_z} \right)_G^2 (2\underline{\alpha}_o \cdot \hat{n})_G^2 \quad (7.32)$$

the incoherent "tilt" factor, cf. (7.24). With the help of (7.4) we find that

$$N_{GS}^{(0)}(\underline{\alpha}_o)_{inc} = \left\langle \frac{(2\alpha_{ox}\zeta_x + 2\alpha_{oy}\zeta_y - 2\alpha_{oz})^4}{(1+\zeta_x^2 + \zeta_y^2)} \right\rangle_G \quad (7.33a)$$

$$= 16 \left\langle \frac{(\alpha_{ox}\zeta_x + \alpha_{oy}\zeta_y - \alpha_{oz})^4}{(1+\zeta_x^2 + \zeta_y^2)} \right\rangle_G \equiv 16 \hat{N}_{G-inc}^{(0)}, \quad \begin{array}{l} \text{[general R}\neq\text{T} \\ \text{(bistatic, etc.)]} \end{array} \quad (7.33b)$$

and specifically, cf. (5.28), (5.30), with symmetrical pdf's of ζ_{Gx} , ζ_{Gy} [cf. (7.54) ff.]:

$$\begin{aligned} N_{GS}^{(0)}(\theta_{oT})_{inc-back} \Big|_{\phi_{oT}=\pi/2} &= 16 \left\{ \sin^4 \theta_{oT} \left\langle \frac{\zeta_y^4}{1+\zeta_x^2 + \zeta_y^2} \right\rangle_G \right. \\ &\quad \left. + 6 \sin^2 \theta_{oT} \cos^2 \theta_{oT} \left\langle \frac{\zeta_y^2}{1+\zeta_x^2 + \zeta_y^2} \right\rangle_G + \cos^4 \theta_{oT} \left\langle \frac{1}{1+\zeta_x^2 + \zeta_y^2} \right\rangle_G \right\}, \quad (7.33c) \end{aligned}$$

$$N_G^{(0)}(\theta_{oT})_{inc-spec} \Big|_{\phi_{oT}=\phi_{oR}=\pi/2} = 16 \cos^4 \theta_{oT} \left\langle \frac{1}{1+\zeta_x^2 + \zeta_y^2} \right\rangle_G. \quad (7.33d)$$

In fact, for the general case here (with $\phi_{oT} = \pi/2$) we get

$$\hat{N}_{GS}^{(0)}(\underline{\alpha}_o)_{inc} \Big|_{\phi_{oT}=\pi/2} = \alpha_{oy}^4 \left\langle \frac{\zeta_y^4}{1+\zeta_x^2 + \zeta_y^2} \right\rangle_G + 6\alpha_{oy}^2 \alpha_{oz}^2 \left\langle \frac{\zeta_y^2}{1+\zeta_x^2 + \zeta_y^2} \right\rangle_G + \alpha_{oz}^4 \left\langle \frac{1}{1+\zeta_x^2 + \zeta_y^2} \right\rangle_G \quad (7.33e)$$

(which are evaluated in (7.66) ff.).

5). Applying (7.31a) to (7.11), with (7.13) as it becomes (7.23b) allows us to write specifically the second-moment function (7.14) for the incoherent component ($k = 0$):

$$M_{X \rightarrow X}^{(0)}(\tau) = \text{Re} \{ k_0^2 G^{(1)} k_0(\tau)_{in} e^{-i\omega_0 \tau} [M_{RT}^{(0)}(\tau | \dots) - (2\alpha_{oz})^2 e^{-4k_0^2 \alpha_{oz}^2 \sigma_G^2 - k_0^2 \sigma_S^2 N_{G-coh}^{(0)} A_{RT}}] \} \quad (7.34)$$

where now

$$M_{RT}^{(0)}(\tau | \dots)_{(k_{0A1}^2 \gg 1)} \doteq \overline{R_0^2} \overline{S^2} \int_{-\infty}^{\infty} \int_{-\infty}^{\infty} Q_{RT}(\underline{r}_1 | f_0) Q_{RT}(\underline{r}_1 + \underline{\Delta r} | f_0)^* e^{2ik_0 \alpha_0 \cdot \underline{\Delta r}} \cdot \left\{ \left(\frac{\alpha_{ox}^2 + \alpha_{oy}^2 + \alpha_{oz}^2}{\alpha_{oz}^2/2} \right)^2 F_2(-2ik_0 \alpha_{oz}, 2ik_0 \alpha_{oz})_G + k_{0G-inc}^2 N_S^{(0)} K_S(\underline{\Delta r}, \tau, \dots) \right\} d\underline{r}_1 d(\underline{\Delta r}) \quad (7.34a)$$

$$A_{RT} \doteq \overline{R_0^2} \overline{S^2} \int_{-\infty}^{\infty} \int_{-\infty}^{\infty} Q_{RT} Q_{RT}^* e^{-2ik_0 \alpha_0 \cdot \underline{\Delta r}} d\underline{r}_1 d(\underline{\Delta r}) = \overline{R_0^2} \overline{S^2} I_1(k_{0\alpha_0}), \quad (7.34b)$$

with I_1 given explicitly by (6.39) here for the general gaussian beam patterns of Sec. 6. Following Bass and Fuks [1], Sections 22, 23, we make the indicated approximations of removing the averages of the reflection coefficients and shadowing functions from under the integral operations, with the observation that these quantities are slowly varying over the regions in which Q_{RT} is noticeably different from zero. (In fact, we can set $\overline{R_0^2} = \overline{R_0^2} = 1$ here for air-water interfaces, but note that $\overline{S^2} \neq \overline{S^2}$, usually, cf. pp. 288, 291 vs. pp. 308, 315 of [1].)

6). At this point we take advantage of the fact that F_{2G} and K_S depend only on the distance difference $\underline{\Delta r}$, because of homogeneity. Thus we can integrate over \underline{r}_1 in (7.34a), using (6.36), (6.40). In addition, because of the short correlation distance ℓ_S vis-à-vis the domain of "illuminated" wave surface, i.e., the region on S_0 , Fig. 5.1, where Q_{RT} is non-

negligible, we may set $\Delta r \doteq 0$ in $I_3(\Delta r)$, (6.40), e.g., since A, B, (6.32), are small compared to unity. The resulting expression for $M_{RT}^{(0)}(\tau|\dots)$, (7.34a), becomes (in (these "high-frequency") relations:

$$M_{RT}^{(0)} \doteq \overline{R_0^2} \overline{S^2} \int_{-\infty}^{\infty} d(\Delta r) I_3(\Delta r) F_{2G}(\Delta r, \tau) \left(\frac{\alpha_{0x}^2 + \alpha_{0y}^2 + \alpha_{0z}^2}{\alpha_{0z}^2/2} \right)^2 e^{i2k_{0z} \Delta r} \\ + I_3(0) k_{0G-inc}^2(\alpha_0) \int_{-\infty}^{\infty} K_S(\Delta r, \tau, \dots) e^{2ik_{0z} \Delta r} d(\Delta r). \quad (7.35)$$

The first term of (7.35) embodies the (non-diffractive) scattering attributable to the large-scale or gravity-wave surface, where the Kirchoff conditions are assumed to hold (cf. remarks after (7.6)). Here the "high-frequency" condition $[(k_{0z} b_0 \sigma_G) \gg 1]$ is assumed to apply cf. remarks in 2). above. Otherwise, in the "low frequency" cases $(k_{0z} b_0 \sigma_G)^2 \ll 1$, (7.27d) is used directly, and the factor $[(\alpha_{0x}^2 + \alpha_{0y}^2 + \alpha_{0z}^2)/\alpha_{0z}^2/2]^2$ is replaced by $(2\alpha_{0z})^2$ in the first term of (7.35).

The second term of (7.35) gives the scattering due to the small-scale, or soliton structure, which rides independently on the large-scale surface. This is generally nonvanishing, since $N_{G-inc}^{(0)} > 0$ as $\theta_{OT} \rightarrow \pi/2$, as we shall see, cf. (7.56), because of the tilted surface (ζ_g). This component we shall call a perturbational component, because of its small Rayleigh number usually, even though we do not employ the standard perturbation theory to derive it, cf. [4]. [In fact, if we were dealing with capillary waves (ζ_s) riding on the gravity wave surface, the slopes of these capillary waves are steep, cf. Figs. 4.10, 4.17 of Phillips [27], so that conventional perturbation techniques are not strictly valid, even though the elevations themselves are suitably small, cf. remarks, Sec. 1.]

C. Remarks on Spectra and Covariance Functions

The last integral of (7.35) is recognized as a form of wave-number-time intensity spectrum, here of the small-scale surface ζ_s . Different forms of such spectra, depending on the details of the definition, can be obtained from the fundamental quantity, the covariance function, K_S here.

Accordingly, let us consider the following forms and definitions (for two-dimensional wave numbers $\underline{k} = (k_x, k_y)$):

$$W_a(\underline{k}|\tau) \equiv \int_{-\infty}^{\infty} K_a(\underline{\Delta r}, \tau) e^{i\underline{k} \cdot \underline{\Delta r}} d(\underline{\Delta r}), \quad (7.36)$$

for surface (a). Here the fundamental definition is the space-time covariance function:

$$K_a(\underline{\Delta r}, \tau) \equiv \langle \zeta_a(\underline{r}_1, t_1) \zeta_a(\underline{r}_1 + \underline{\Delta r}, t_1 + \tau) \rangle = \overline{\zeta_{1a} \zeta_{2a}}, \quad \langle \zeta_a \rangle = 0, \quad (7.37)$$

where, as before, we have assumed that the surface elevation, ζ_a , is both homogeneous and stationary. The transform relation corresponding to (7.36) is easily found by multiplying both sides of (7.36) by $(2\pi)^{-2} \exp(-i\underline{k} \cdot \underline{\Delta r})$, integrating over \underline{k} , observing that

$$\int_{-\infty}^{\infty} e^{i\underline{k} \cdot (\underline{\Delta r}' - \underline{\Delta r})} \frac{d\underline{k}}{(2\pi)^2} = \delta(\underline{\Delta r}' - \underline{\Delta r}). \quad (7.38)$$

The result is

$$K_a(\underline{\Delta r}, \tau) = \int_{-\infty}^{\infty} W_a(\underline{k}|\tau) e^{-i\underline{k} \cdot \underline{\Delta r}} \frac{d\underline{k}}{(2\pi)^2} \quad (7.39)$$

so that, for example, the mean-square surface elevation σ_a^2 is, from (7.37),

$$\left\{ \begin{aligned} \langle \zeta_a^2 \rangle &= K_a(0,0) = \int_{-\infty}^{\infty} W_a(\underline{k}|0) \frac{d\underline{k}}{(2\pi)^2} \equiv \sigma_a^2, \\ \therefore \rho_a(0,0) &\equiv K_a(0,0)/\sigma_a^2 = 1, \end{aligned} \right. \quad (7.40)$$

$$(7.40a)$$

when our spectral definition (7.36) is used, as we shall do so here henceforth. Consequently, the last integral in (7.35) is seen to be

$$\int_{-\infty}^{\infty} K_S(\underline{\Delta r}, \tau + \dots) e^{2i\underline{k}_{00} \cdot \underline{\Delta r}} d(\underline{\Delta r}) = W_S(2\underline{k}_{00}|\tau) \equiv \sigma_S^2 W_S(2\underline{k}_{00}|\tau), \quad (7.41)$$

the wave-number-time spectrum of the small-scale surface; \hat{w}_s is the normalized spectral density, both defined according to (7.36) above. We shall use this result subsequently, in Section 8.

Next, let us consider the Wiener-Khintchine forms (Sec. 3.2-2, [45])

$$W_a(f) \equiv 2 \int_{-\infty}^{\infty} K_a(\tau) e^{-i\omega\tau} d\tau \equiv 2 \int_{-\infty}^{\infty} d\tau \int_{-\infty}^{\infty} K_a(\underline{\Delta r}, \tau) e^{i\mathbf{k} \cdot \underline{\Delta r} - i\omega\tau} d(\underline{\Delta r}), \quad (7.42a)$$

$\omega = 2\pi f$

with the inverse relation

$$\hat{K}_a(\tau) = \frac{1}{2} \int_{-\infty}^{\infty} W_a(f) e^{i\omega\tau} df = \int_{-\infty}^{\infty} K_a(\underline{\Delta r}, \tau) e^{i\mathbf{k} \cdot \underline{\Delta r}} d(\underline{\Delta r}). \quad (7.42b)$$

Also, in terms of $W_a(\mathbf{k}|\tau)$, etc., we have the transform pairs

$$W_a(\mathbf{k}, \omega) \equiv \int_{-\infty}^{\infty} W_a(\mathbf{k}|\tau) e^{-i\omega\tau} d\tau = \int_{-\infty}^{\infty} \int_{-\infty}^{\infty} K_a(\underline{\Delta r}, \tau) e^{i\mathbf{k} \cdot \underline{\Delta r} - i\omega\tau} d(\underline{\Delta r}) d\tau \quad (7.43a)$$

$\omega = 2\pi f,$

and

$$K_a(\underline{\Delta r}, \tau) = \int_{-\infty}^{\infty} \int_{-\infty}^{\infty} W_a(\mathbf{k}, \omega) e^{i\omega\tau - i\mathbf{k} \cdot \underline{\Delta r}} \frac{d\omega}{2\pi} \frac{d\mathbf{k}}{(2\pi)^2}, \quad (7.43b)$$

so that

$$\overline{\zeta_a^2} = \sigma_a^2 = K_a(0,0) = \int_{-\infty}^{\infty} \int_{-\infty}^{\infty} W_a(\mathbf{k}, \omega) \frac{d\omega d\mathbf{k}}{(2\pi)^3} = \int_{-\infty}^{\infty} W_a(\mathbf{k}|0) \frac{d\mathbf{k}}{(2\pi)^2}, \quad (7.44)$$

by (7.40).

Similarly, using $\underline{v} = \mathbf{k}/2\pi$, $f = \omega/2\pi$ as the basic variables for spatial frequency and frequency, respectively, we can write

$$\left\{ \begin{aligned} W_a(\underline{v}|\tau) &= \int_{-\infty}^{\infty} K_a(\underline{\Delta r}, \tau) e^{2\pi i \underline{v} \cdot \underline{\Delta r}} d(\underline{\Delta r}) = W_a(\mathbf{k}|\tau); \quad \underline{v} = \mathbf{k}/2\pi, \end{aligned} \right. \quad (7.45a)$$

$$\left\{ \begin{aligned} K_a(\underline{\Delta r}, \tau) &= \int_{-\infty}^{\infty} W_a(\underline{v}|\tau) e^{-2\pi i \underline{v} \cdot \underline{\Delta r}} d\underline{v}, \end{aligned} \right. \quad (7.45b)$$

II. Phillips. [27]; Sec. 4.1:

$$(\underline{r} \rightarrow \underline{\Delta r}; t \rightarrow \tau): \quad Z_a(\underline{\Delta r}, \tau)_p = \langle \zeta_{1a} \zeta_{2a} \rangle = K_a(\underline{\Delta r}, \tau) \quad (7.50a)$$

$$Z \rightarrow k; n \rightarrow \omega \quad X(k, \omega) = \int_{-\infty}^{\infty} \int Z_a(\underline{\Delta r}, \tau)_p e^{i\omega\tau - i\mathbf{k} \cdot \underline{\Delta r}} \frac{d\tau d(\underline{\Delta r})}{(2\pi)^3} \quad (7.50b)$$

$$\left. \begin{aligned} X &\equiv W(\underline{k}, \omega)_p = W_a(\underline{k}, \omega)/(2\pi)^3 \\ \Psi(k) &\equiv W(\underline{k})_p = (2\pi)^{-2} W_a(\underline{k}|0) \\ \Phi(\omega) &\equiv \int W(\underline{k}, \omega)_p d\underline{k} = W_a(\omega)/2\pi \end{aligned} \right\} \begin{aligned} &\therefore W_a(\underline{k}, \omega)_{B+F} = W_a(\underline{k}, \omega)_p / \sigma_a^2. \\ &= W_a(\underline{k}, \omega)/(2\pi)^3 \sigma_a^2, \text{ etc.} \end{aligned} \quad (7.51)$$

III. McDaniels and Gorman [4], Eq. (16):

$$W_a(\underline{k}|0)_{McD+G} = \frac{1}{2\pi} \int_{-\infty}^{\infty} K_a(\underline{\Delta r}, 0) e^{i\underline{\Delta r} \cdot \underline{k}} d(\underline{\Delta r}) \text{ vs. (7.41)} \quad (7.51a)$$

$$\therefore W_a(\underline{k}|0)_{McD+G} = (2\pi)^{-1} W_a(\underline{k}|0)_{Mid}. \quad (7.51b)$$

IV. Bahar [23], Eq. (14b):

$$W_a(\underline{k}|0)_{B+B} = \pi^{-2} W_a(\underline{k}|0)_{Mid}, \quad (7.51c)$$

$$\therefore W_a(\underline{k}|0)_{B+B} = \frac{2}{\pi} W_a(\underline{k}|0)_{McD+G}. \quad (7.51d)$$

D. Capillary Wave-Number Spectra

For the record it is instructive to summarize the specific results for capillary wave-number spectra, which are needed in subsequent investigations.

Proceeding from the defining relation (7.36) we have

$$W_{cap}(k_x, k_y|0) \equiv \int_{-\infty}^{\infty} K_{cap}(\underline{\Delta r}, 0) e^{i\mathbf{k} \cdot \underline{\Delta r}} d(\underline{\Delta r}) \quad (7.52a)$$

$$= \frac{1}{2} \int_{-\infty}^{\infty} W_c(f_s) \langle \delta(\underline{v} - \underline{K}_s(\hat{\alpha})/2\pi) \rangle_{\hat{\alpha}} df_s, \quad \underline{v} \equiv \underline{K}_s/2\pi, \quad f_s \geq 0, \quad (7.52b)$$

where W_c is the point (intensity)-spectrum of the (pure) capillary surface,

ζ_c , assumed here to be homogeneous and stationary, and α is the wave direction. Since in polar coordinates

$$\delta(\underline{v} - \underline{K}_S(\hat{\alpha})) = \delta(|\underline{v}| - F_\alpha(\omega_S))\delta(\phi_v - \hat{\alpha}), \quad \underline{K}_S = \underline{K}_S(f_S), \quad \omega_S = 2\pi f_S, \quad (7.53)$$

where \underline{K}_S and f_S are related by the dispersion law $K_S = 2\pi/\lambda_S = a_c^{1/3} \omega_S^{2/3}$, with $a_c = \rho_{\text{water}}/\mathcal{J}$, where ρ_{water} is the density of water ($\approx 1 \text{ gm/cm}^3$) and \mathcal{J} = surface tension ($= 74 \text{ dynes-cm}$), we find that

$$\delta(v - \frac{|\underline{K}_S(\omega_S)|}{2}) = \frac{3\sqrt{2\pi v}}{2a_c^{1/2}} \delta(f_S - K_S^{3/2}/2\pi a_c^{1/2}), \quad f_S \geq 0. \quad (7.54)$$

Thus, (7.52b) becomes directly, with $k = \sqrt{k_x^2 + k_y^2}$, $\phi_v = \tan^{-1}(k_y/k_x)$:

$$W_{\text{cap}}(k, \phi_v | 0) = \frac{3\sqrt{K_S}}{4a_c^{1/2}} W_c(f_S = K_S^{3/2}/2\pi a_c^{1/2}) \langle \delta(\phi_v - \hat{\alpha}) \rangle_{\hat{\alpha}}, \quad f_S \geq 0. \quad (7.55)$$

A similar calculation for (pure) gravity waves, where $K_S = \omega_S^2/g$ is the dispersion law, gives

$$W_g(\underline{k} | 0) = \frac{\pi}{2} g K_S^{-3/2} W_g\left(\frac{1}{2\pi} \sqrt{K_S g}\right) \langle \delta(\phi_v - \hat{\alpha}) \rangle_{\hat{\alpha}}, \quad f_S \geq 0. \quad (7.56)$$

In the above we have

$$\left. \begin{aligned} \langle \delta(\phi_v - \hat{\alpha}) \rangle_{\hat{\alpha}} &= w_1(\hat{\alpha} - \hat{\alpha}_0); & -\pi/2 < \hat{\alpha} - \hat{\alpha}_0 < \pi/2 \\ &= 0, \text{ elsewhere} \end{aligned} \right\} \quad (7.57)$$

where $w_1(\hat{\alpha} - \hat{\alpha}_0)$ is the pdf of wavefront directions. No backward waves are permitted here: ($f_S > 0$) and $(\hat{\alpha} - \hat{\alpha}_0) \leq \pi/2$.

For our results above $K_S = 2\pi v = 2k_0 \sin \theta_{0T}$, $\phi_{0T} = \pi/2$, e.g., $k_x = 0$, $k_y = 2k_0 \sin \theta_{0T}$ and $K_S = (k_x^2 + k_y^2)^{1/2}$, with $\phi_v = \pi/2$. Thus, if $\hat{\alpha}_0 = 0$, so that the transmitting and receiving beams are cross-wind to the mean wave direction ($\hat{\alpha} = 0$), $W_g(k, \phi_v | 0) = 0$, since $w_1(\pi/2) = 0$ here.

A variety of point spectra, W , is available. If we choose the Pearson-Moskowitz spectrum [8], we can write specifically

$$W_{P.M.}(f_s) = \frac{a}{\omega_s} e^{-b/\omega_s^4}; \quad a = 8.10 \cdot 10^{-3} g^2; \quad b = 0.74 g^4 / v^4; \quad (7.58)$$

$$v = \text{m/sec}, \quad g = \text{m/sec}^2.$$

For the purely capillary cases we have, accordingly, $\omega_s = (K_s/a_c)^{3/2}$, while for the (purely) gravity wave situations, $\omega_s = \sqrt{K_s g}$.

In the general case the dispersion relation of the combined gravity-capillary wave is

$$\omega_s = (gK_s + \frac{1}{\rho} K_s^3)^{1/2}, \quad \text{or} \quad f_s = \frac{1}{2\pi} (gK_s + \frac{1}{\rho} K_s^3)^{1/2}, \quad (7.59)$$

so that

$$\delta(v - F_s(\omega_s)) = \frac{3\sqrt{2\pi v}}{2\sqrt{a_c}} \delta(f_s - \frac{1}{2\pi} [gK_s + K_s^3 a_c]^{1/2}), \quad (7.60)$$

in (7.53) et seq.

7.4 Extensions

Here we summarize various additional results, needed in our analysis above. These are:

A. The Diffraction Terms ($k \geq 1$)

These are obtained from (7.16) in (7.15), and clearly depend critically on the statistics of $\langle \Delta v_1^{(k)} \Delta v_2^{(k)} \rangle_R$. To date we have only evaluated the case $k=1$: diffuse (single-point) diffraction. For this we have found that [41 II, III]

$$(k=1) \quad \langle \Delta v_1^{(1)} \Delta v_2^{(1)} \rangle_R = |J_1| \delta(\underline{Ar}-0), \quad \text{where } |J| \equiv |\zeta_{xx}\zeta_{yy} - \zeta_{xy}^2|. \quad (7.61)$$

Thus, $|J|$ is a measure of the surface curvature (at stationary phase points). Here

$$|J|_{G+S} \doteq |J_G - \frac{1}{\sqrt{1+\zeta_{Gx}^2+\zeta_{Gy}^2}} J_S| \doteq \frac{1}{\sqrt{1+\zeta_{Gx}^2+\zeta_{Gy}^2}} |J_S| \doteq |J_S|, \quad (7.61a)$$

since $\langle (1+\zeta_{Gx}^2+\zeta_{Gy}^2)^{-1/2} \rangle = 1 + O(2\sigma_{Gx}^2) \doteq 1$; (see below the coefficient of

$\cos^4 \theta_{OT}$ in (7.66); also, $|J_G| \ll |J_S|$, because ζ_{Gx}, ζ_{Gy} are essentially constant in the region in question about ζ_S , where ζ_S has (local) stationary phase points. [Also, we can show formally that [41, II]]

$$(k \geq 1) \quad \langle \Delta v_1^{(k)} \Delta v_2^{(k)} \rangle_R = R_{12}^{(k)}(r_1, t_1; r_2, t_2) \quad (\geq 0), \quad (7.62)$$

where $R_{12}^{(k)}$ is proportional to the joint probability of having k -coupled scatterers jointly at (r_1, t_1) and (r_2, t_2) .

We remark, however, that in most cases these diffraction terms ($k \geq 1$) are considerably smaller than the ($k=0$) components, cf. remarks in Sec. 3.3. In any case, see Sec. 8.5 for an evaluation of $M_{X-\langle X \rangle}^{(1)}(0)$, (7.15), (7.16).

B. The Evaluation of the "Tilt-Factor," $N_{G-inc}^{(0)}$

The "tilt-factor" $N_{G-inc}^{(0)}$, (7.33), can be readily evaluated in the isotropic cases; (we reserve the general anisotropic case to a subsequent study). Before we proceed to an evaluation, however, it is immediately evident from (7.33c) that $N_{G-inc}^{(0)} > 0$ when $\theta_{OT} \rightarrow \pi/2$, or $\phi_{\text{grazing}} = 0$. This nonvanishing result is qualitatively consistent with other results [cf. Eq. (27), Eq. A.14 of [4], and (4) in (2) of [3]; also Sec. III of [29]], as $\theta_{OT} \rightarrow \pi/2$. However, these earlier results use an ad hoc mechanism: special modulation of the grazing angle--to account for the "tilt" produced here naturally through the explicit (slow) time-variability of \hat{n}_G , cf. (7.4) and the comments after Eq. (5.21).

Since ζ_G is gaussian, $\langle \zeta_G \rangle = 0$, the pdf of the slopes is likewise, such that

$$w_1(\zeta_{Gx}, \zeta_{Gy}) = \frac{e^{-\zeta_{Gx}^2/2\sigma_{Gx}^2 - \zeta_{Gy}^2/2\sigma_{Gy}^2}}{2\pi\sigma_{Gx}\sigma_{Gy}}; \quad \sigma_{xy}^2 \equiv \overline{\zeta_{Gx}\zeta_{Gy}} = 0. \quad (7.63)$$

We use (7.63) in the isotropic case $\sigma_{Gx} = \sigma_{Gy}$ for direct evaluation of the averages in (7.33c) for backscatter regimes. We consider the integrals

$$\begin{aligned} I^{(0),(2),(4)} &= \int_{-\infty}^{\infty} \int_{-\infty}^{\infty} \frac{(1, y^2, y^4)}{1+x^2+y^2} e^{-(x^2+y^2)/2\sigma_x^2} \frac{dx dy}{2\pi\sigma_x^2} \\ &= \int_0^{\infty} dr \int_0^{2\pi} d\phi [1, r^2 \sin^2 \phi, r^4 \sin^4 \phi] \frac{e^{-r^2/2\sigma_x^2}}{2\pi\sigma_x^2} r dr d\phi \end{aligned}$$

$$= \frac{1}{2\pi\sigma_x^2} \int_0^\infty (2\pi, \pi r^2, 3\pi^4/4) \frac{re^{-r^2/2\sigma^2}}{1+r^2} dr. \quad (7.64)$$

These integrals may be expressed in terms of the exponential integral, e.g.,

$$\frac{1}{2} \int_0^\infty \frac{e^{-a^2 y}}{1+y} dy = -\frac{e^{a^2}}{2} \text{Ei}(-a^2) \quad (7.65a)$$

Using the fact that $a^2 = 1/2\sigma_x^2 \gg 1$, here, and the expansion

$$-e^x \text{Ei}(-x) \approx 2\sigma_x^2 \sum_{m=0}^\infty (-1)^m m! (2\sigma_x^2)^m; \quad x = a^2 = 1/2\sigma_x^2, \quad (7.65b)$$

we find finally that (7.33c) reduces to

$$\boxed{N_{\text{GS}}^{(0)}(\theta_{\text{OT}})_{\text{inc-back}} \doteq 16\{3(\sigma_{\text{Gx}}^2)^2 \sin^4 \theta_{\text{OT}} + 6\sigma_{\text{Gx}}^2 \sin^2 \theta_{\text{OT}} \cos^2 \theta_{\text{OT}} + \cos^4 \theta_{\text{OT}}\};} \quad (7.66a)$$

$$(\phi_{\text{OT}} = \pi/2) \quad (\sigma_{\text{Gx}} = \sigma_{\text{Gy}}),$$

which becomes $48\sigma_{\text{Gx}}^2 (>0)$ when $\theta_{\text{OT}} \rightarrow \pi/2$, demonstrating its nonvanishing nature, as noted above. Similarly, from (7.33b) and the above we get directly

$$\boxed{N_{\text{GS}}^{(0)}(\theta_{\text{OT}})_{\text{inc-for-spec}}|_{\phi_{\text{OT}}=\phi_{\text{OR}}=\pi/2} \doteq 16[1 + O(2\sigma_{\text{Gx}}^2)] \cos^4 \theta_{\text{OT}}.} \quad (7.66b)$$

Similarly, for the general case we get from (7.33e) in these isotropic situations:

$$N_{\text{GS}}^{(0)}(\alpha_o)_{\text{inc}}|_{\phi_{\text{OT}}=\pi/2} \doteq 16\{3(\sigma_{\text{Gx}}^2)^2 \alpha_{\text{oy}}^4 + 6\sigma_{\text{Gx}}^2 \alpha_{\text{oy}}^2 \alpha_{\text{oz}}^2 + \alpha_{\text{oz}}^4\}. \quad (7.66c)$$

Here (7.66b), unlike the backscatter cases, vanishes as $\theta_{\text{OT}} \rightarrow \pi/2$. Note, however, from (5.24), (5.25) that $N_{\text{inc}}^{(0)} > 0$, generally, as $\theta_{\text{OT}} \rightarrow \pi/2$, cf. (7.66c).

C. Shadowing Functions \bar{S} , \bar{S}^2

The rôle of the shadowing functions \bar{S} , \bar{S}^2 is extensively discussed in Sections 22, 23 of [1]. We summarize the principal results needed here. The precise forms depend on whether monostatic (R=T) or bistatic (R≠T) operation is involved.

With $a \equiv (\tan \theta)/\sigma_{x=y} = \cot \theta_{OT}/\sigma_{x=y}$, we have for \bar{S} in the coherent component [(k=0): (7.13), (7.25)]

$$\bar{S}_{R\neq T}|_{\text{weak shadowing}} = \Theta(a/\sqrt{2}) [1 - \Lambda_N(a)] \Big|_{a^2 \gg 1} : \text{Eq. (22.39), [1], p. 288,} \quad (7.67a)$$

$$\approx (1 - \frac{1}{a} \sqrt{\frac{2}{\pi}} e^{-a^2/2}) (1 - \frac{1}{a^3 \sqrt{2\pi}} e^{-a^2/2}) \Big|_{a^2 \gg 1} \quad (7.67b)$$

$$\bar{S}_{R\neq T}|_{\text{strong shadowing}} = \{\text{Eq. (22.52, [1], p. 291)}\} e^{-2k_0^2 \sigma_G^2 \cos^2 \theta_{OT}}. \quad (7.68)$$

Here we have specifically

$$\Lambda_N(a) = \frac{1}{2a} \left\{ \sqrt{\frac{2}{\pi}} e^{-a^2/2} - a(1 - \Theta[a/\sqrt{2}]) \right\}; \quad \Theta(x) \equiv \frac{2}{\sqrt{\pi}} \int_0^x e^{-t^2} dt : \quad (7.68a)$$

error function.

These results also apply in the Snell direction for forward scattering, R≠T, obeying (5.29).

For \bar{S}^2 , associated with the intensity of the incoherent components, we find that

$$\text{back-scatter} \left\{ \begin{aligned} \bar{S}_{R\neq T}^2 &= \frac{1}{1 + \Lambda_N(a)}, \text{ Eq. (23.29a), p. 308, [1]} & (7.69a) \\ &\approx \Lambda_N(a)^{-1} \Big|_{a \ll 1} : \text{strong shadowing;} & (7.69b) \\ &\approx 1 - \Lambda_N(a) \Big|_{a \gg 1} : \text{weak shadowing, cf. pp. 308-311, [1].} \end{aligned} \right.$$

$$\text{forward scatter} \left\{ \begin{aligned} \bar{S}_{R\neq T}^2 &= \frac{1}{1 + \Lambda_N(a) + \Lambda_N(b)}, \text{ Eq. (23.40), p. 315, [1]:} \\ a &= \frac{\cot \theta_{OT}}{\sigma_{x=y}}; \quad b = \frac{\cot \theta_{OR}}{\sigma_{x=y}} \end{aligned} \right. \quad (7.69c)$$

For details, see subsections 4,5 of Sec. 22, and pp. 304-315, of [1].

8. Limiting Cases of Scatter Intensities for Random, Two-Scale Surface Models

The two limiting cases which we consider here are respectively (1) the "high-frequency", large-scale gravity wave surface (G), where $(k_0 b_0 \sigma_G = k_0 (\cos \theta_{OT} + \cos \theta_{OR}) \langle \zeta_G^2 \rangle)^2 \gg 1$, and (2) the "low-frequency" condition, where $(k_0 b_0 \sigma_G)^2 \ll 1$, viz., large and small Rayleigh numbers for this large-scale surface wave component. The small-scale, or soliton-ripple surface (S), is such that its Rayleigh number is always small, e.g. $(k_0 b_0 \sigma_S)^2 \ll 1$, $\sigma_S^2 \equiv \langle \zeta_S^2 \rangle$. Moreover, critical to the specific results here is the fact that the correlation distance* of the small-scale surface is likewise small vis-à-vis that of the large-scale component, e.g., $\ell_S \ll \ell_G$. (This fact ensures the explicit separability of the two components in the detailed analysis, cf. Sec. 7.)

Our task here is to provide specific relations for the mean scatter intensities under a variety of operating régimes: (1) "high-frequency" (G), backward and "foreward" scatter, both incoherent and coherent; and (2) the same for the "low-frequency" (G) cases, including specular (Snell) and non-specular directions. These results, in turn, are employed in Section 2 to give the desired scattering cross-sections, which are the ultimate analytical goals of this initial study. For the most part, the diffraction terms ($k \gg 1$) are ignorable vis-à-vis the "classical" ($k=0$) contributions studied here.

Before examining the various special cases above, let us note the following general results:

8.1 Scattering Intensities: General Forms for "High Frequencies"

From (7.34) and (7.35) we have directly the following "high-frequency" form for the incoherent scatter intensities ($\tau=0$) of these two-component wave surfaces:

$$\begin{aligned} (k_0 b_0 \sigma_G)^2 \gg 1: \quad M_{\mathbf{x} \leftarrow \mathbf{x}}^{(0)}(0) &= G^{(1)} K_0(0) \sqrt{R_0^2 S^2} \left[k_0^2 \left(\frac{\alpha_{0x}^2 + \alpha_{0y}^2 + \alpha_{0z}^2}{\alpha_{0z}^2} \right)^2 I_2(2\alpha_0 \mathbf{b}_{TR} | \hat{\mathbf{D}}) \right. \\ &\quad \left. + k_0^4 N_{G-inc}^{(0)}(2\alpha_0) I_3(0) W_S(2\alpha_0 k_0 | 0) \right], \end{aligned} \quad (8.1)$$

*For the moment we use an "isotropic" distance $\ell = \sqrt{\ell_x^2 + \ell_y^2}$ to describe this quantity; generally, a wave surface has two correlation distances, ℓ_x , ℓ_y , cf. [1], Sec. 3.

where the term $M_{\langle X \rangle}^{(0)}(\infty | \dots) \rightarrow 0$ in (7.34) for these high-frequency situations, cf. A, Sec. 7.3, and $A_1 (= 2\pi/\sqrt{AB})$ is such that $k_0^2 A_1 \gg 1$, cf. (7.27c) et seq. Here and throughout, $2\alpha_0 = (2\alpha_{0x}, 2\alpha_{0y})$, cf. $\underline{\Delta r} \cdot 2\alpha_0$ in I_2 , I_3 : $\underline{\Delta r}$ has only x,y components.

Since F_{2G} (7.29) in (7.34a) becomes here for the gaussian gravity wave surface, on expanding $\rho_G(\Delta l, 0)$:

$$F_{2G} = e^{-(k_0 b_0 \sigma_G)^2 (1 - \rho_G[\underline{\Delta r}, 0])} = e^{-(k_0^2/2) \underline{\Delta r} \cdot \hat{\underline{D}}_M \cdot \underline{\Delta r}}, \quad (k_0 b_0 \sigma_G)^2 \gg 1, \quad (8.2)$$

where now the dyadic

$$\hat{\underline{D}}_M = \begin{bmatrix} b_{0\sigma_{Gx}}^2 & b_{0\rho_{xy}}^2 \\ b_{0\rho_{xy}}^2 & b_{0\sigma_{Gy}}^2 \end{bmatrix} \doteq \begin{bmatrix} b_{0\sigma_{Gx}}^2 & 0 \\ 0 & b_{0\sigma_{Gy}}^2 \end{bmatrix}, \quad \rho_{xy} \doteq 0; \quad b_0 = \cos\theta_{0T} + \cos\theta_{0R}; \quad (8.2a)$$

and

$$\therefore \hat{\underline{D}}_M^{-1} = \frac{1}{b_0^2} \begin{bmatrix} 1/\sigma_{Gx}^2 & 0 \\ 0 & 1/\sigma_{Gy}^2 \end{bmatrix}; \quad \det \hat{\underline{D}}_M = b_0^4 (\sigma_{Gx}^2 \sigma_{Gy}^2 - \rho_{xy}^2) \doteq b_0^4 \sigma_{Gx}^2 \sigma_{Gy}^2 (> 0). \quad (8.2b)$$

We see that I_2 in (8.1) is specifically

$$I_2(2\alpha_0 - \underline{b}_{TR}) = \iint \underline{Q}_{RT} \underline{Q}_{RT}^* e^{2ik_0 \alpha_0 \cdot \underline{\Delta r} - (k_0^2/2) \underline{\Delta r} \cdot \hat{\underline{D}}_M \cdot \underline{\Delta r}} \underline{dr} d(\underline{\Delta r}) \quad (8.3a)$$

$$\doteq \frac{(g_T g_R)^2 2\pi^2}{k_0^2 \sqrt{AB(\theta)} \det \hat{\underline{D}}_M} e^{-\frac{1}{2}(2\alpha_0 - \underline{b}_{TR}) \cdot \hat{\underline{D}}_M^{-1} \cdot (2\alpha_0 - \underline{b}_{TR})}, \quad (8.3b)$$

(with k_0^2 absorbed into A, B, cf. remarks (6.43) ff.), from (6.43) (subject to the approximations (6.42)). Moreover, from (6.40) and (6.52), we have

$$I_3(0) = (g_T g_R)^2 \pi / \sqrt{AB} = (g_T g_R)^2 A_1 / 2. \quad (8.4)$$

Applying (8.2b), (8.3b), (8.4) to (8.1) then yields the following general high-frequency form for the incoherent scatter intensity for arbitrary directions of incidence and observation, with the finite dimensions of the transmitting and receiving arrays taken into account:

$$\begin{aligned}
M_{X \rightarrow X}^{(0)}(0) \Big|_{(\text{Hi-Freq})} &\approx G^{(1)} K_0(0) \bar{R}_0^2 \bar{S}^2 A_1 (g_T g_R)^2 \\
&\cdot \left[\left(\frac{\alpha_{0x}^2 + \alpha_{0y}^2 + \alpha_{0z}^2}{\alpha_{0z}/2} \right)^2 \frac{\pi \exp \left(-\frac{1}{2} \left[\frac{(2\alpha_{0x} - b_{TRx})^2}{b_0^2 \sigma_{Gx}^2} + \frac{(2\alpha_{0y} - b_{TRy})^2}{b_0^2 \sigma_{Gy}^2} \right] \right)}{\sigma_{Gx} \sigma_{Gy} b_0^2} \right. \\
&\quad \left. + \frac{k_0^4}{2} N_G^{(0)}(2\alpha_0)_{\text{inc}} W_S(2\alpha_0 | 0) \right]. \quad (8.5)
\end{aligned}$$

Generally, $b_{TRx,y} \doteq 0$, if one is sufficiently in the far-field of the scattering surface, so that here, cf. Fig. (5.1), (8.5) reduces to the simpler result

$$\begin{aligned}
(b_{TR} \doteq 0) \quad M_{X \rightarrow X}^{(0)}(0) \Big|_{\substack{(\text{Hi-Freq}) \\ k_0^2 A_1 \gg 1}} &\approx G^{(1)} K_0(0) \bar{R}_0^2 \bar{S}^2 (g_T g_R)^2 A_1 \\
&\cdot \left[\left(\frac{\alpha_{0x}^2 + \alpha_{0y}^2 + \alpha_{0z}^2}{\alpha_{0z}/2} \right)^2 \frac{\pi \exp \left\{ -\left[\frac{(2\alpha_{0x})^2}{2b_0^2 \sigma_{Gx}^2} + \frac{(2\alpha_{0y})^2}{2b_0^2 \sigma_{Gy}^2} \right] \right\}}{b_0^2 \sigma_{Gx} \sigma_{Gy}} \right. \\
&\quad \left. + \frac{k_0^4}{2} N_G^{(0)}(2\alpha_0)_{\text{inc}} W_S(2\alpha_0 k_0 | 0) \right]. \quad (8.6)
\end{aligned}$$

The first term of (8.6) represents the "geometrical acoustic" (i.e., high-frequency, $k_0 \rightarrow \infty$) solution, for the specular point, or facet, (acoustic) scatter from the large-scale gravity wave component. As expected, it is independent of frequency. The second term of (8.6) represents the "perturbational" or small-scale component solution through first-order Bragg scatter ($\sim W_S$), which is always nonvanishing ($k_0 < \infty$). [Various, less general forms of (8.6) have been obtained by a number of authors recently; this point is discussed more fully in Sections 2 and 4.]

The coherent component of the scatter intensity, $M_{X \rightarrow X}^{(0)}(0)$, is similarly obtained from (7.23)-(7.26) in (7.13). The result is

$$M_{\langle X \rangle}^{(0)}(0) = G^{(1)} K_0(0)_{in} k_0^2 \bar{R}_0^{-2} \bar{S}^2 A_1^2 (g_T g_R)^2 \cdot \left[\frac{(-2\alpha_{oz})^2}{2} e^{-b_0^2 k_0^2 \sigma_G^2 + k_0^2 \sigma_S^2 N_{G-coh}^{(0)}} - \frac{3k_0^2}{4} \left\{ \frac{(2\alpha_0 - b_{TR})_x^2}{A} + \frac{(2\alpha_0 - b_{TR})_y^2}{B} \right\} \right], \quad (8.7)$$

which is valid for all frequencies (and the various other conditions of Sec. 5.5, Sec. 6). Here we have, cf. (6.32),

$$A = \frac{A_T}{R_{OT}^2} + \frac{A_R}{R_{OR}^2}; \quad B = a_T(\theta)^2 \frac{A_T}{R_{OT}^2} + a_R(\theta)^2 \frac{A_R}{R_{OR}^2}, \quad (8.7a)$$

cf. (6.11a), where we have absorbed the k_0^2 -factor in (6.17) into A_T, A_R , so that these quantities represent the effective aperture (or array) areas of the transmitter (T) and receiver (R). For the high frequency cases considered here, $b_0^2 \sigma_G^2 k_0^2 \gg 1$, so that $M_{\langle X \rangle}^{(0)}(0) \rightarrow 0$, as noted above, cf. (8.1) et seq.

8.2 Scattering Intensities: General Forms for "Low Frequencies"

For the "low-frequency" cases we use (7.27d), with (7.23b), (7.25), to write for the incoherent scatter intensity (7.34) now, on expanding F_{2G} in (7.34a), with $[\alpha_{ox}^2 + \alpha_{oy}^2 + \alpha_{oz}^2 / \alpha_{oz} / 2]^2$ replaced by $(-2\alpha_{oz})^2$ since the condition $k_0^2 A_1 \gg 1$ may not hold:

$$M_{X-\langle X \rangle}^{(0)}(0) \Big|_{\text{low freq}} \doteq G^{(1)} K_0(0)_{in} \{ k_0^2 b_0^2 e^{-k_0^2 b_0^2 \sigma_G^2} [\bar{R}_0^2 \bar{S}^2 - \bar{R}_0^{-2} \bar{S}^2 e^{-k_0^2 \sigma_S^2 N_{G-coh}^{(0)}}] \cdot I_1(2\alpha_0 - b_{TR}) + \bar{R}_0^2 \bar{S}^2 b_0^4 k_0^4 \int K_G(\underline{\Delta r}, 0) I_3(\underline{\Delta r}) e^{2ik_0 \alpha_0 \cdot \underline{\Delta r}} d(\underline{\Delta r}) + \bar{R}_0^2 \bar{S}^2 I_3(0) k_0^4 N_{G-inc}^{(0)} W_S(2\alpha_0 k_0 | 0) \}, \quad (8.8)$$

where we have integrated over \underline{r} to get $I_3(\underline{\Delta r})$, (6.36), (6.40) in the second term. Since A, B , (8.7a) are small compared to the regions $\underline{\Delta r}$

where $K_G(\underline{\Delta}r, 0)$ is significant, we can set $\underline{\Delta}r \rightarrow 0$ in $I_3(\underline{\Delta}r)$ without noticeably changing the result. Accordingly, (8.8) reduces to the following expression

$$\boxed{M_{X-\langle X \rangle}^{(0)} \Big|_{\text{Low Freq}} = G^{(1)} K_0(0)_{\text{in}} \{ \Delta_{RS}(\alpha_0) + \overline{R_0^2} \overline{S^2} (g_T g_R)^2 A_1 \cdot \left[\frac{k_0^4}{2} b_0^4 W_G(2\alpha_0 k_0 | 0) + \frac{k_0^4}{2} N_{GS-\text{inc}}^{(0)} W_S(2\alpha_0 k_0 | 0) \right] \}} \quad (8.9)$$

where

$$\Delta_{RS}(\alpha_0) \equiv k_0^2 b_0^2 e^{-k_0^2 b_0^2 \sigma_G^2} \left(\overline{R_0^2} \overline{S^2} - \overline{R_0^2} \overline{S^2} e^{-k_0^2 \sigma_S^2 N_{G-\text{coh}}^{(0)}} \right) I_1(2\alpha_0 - b_{TR}), \quad (8.9a)$$

$$\equiv 0, \quad (2\alpha_0 - b_{TR})_x \text{ or } y \neq 0, \quad k_0^2 b_0^2 \sigma_G^2 \ll 1, \quad (8.9b)$$

since from (6.39) (with k_0^2 -factor absorbed, and added in the exponent):

$$I_1(2\alpha_0 - b_{TR}) = \frac{(g_T g_R)^2}{k_0^2} A_1^2 e^{-\frac{3}{2} k_0^2 \left[\frac{(2\alpha_{0x} - b_{TR})^2}{A} + \frac{(2\alpha_{0y} - b_{TR})^2}{B} \right]} \quad (0 < A, B < 1). \quad (8.9c)$$

Furthermore, when $\overline{R_0^2} = \overline{R_0^2} \equiv R_0^2 (=1)$, usually here, and $\overline{S^2} = \overline{S^2} \equiv 1$ (weak shadowing), with $k_0^2 \sigma_S^2 N_{G-\text{coh}}^{(0)} \ll 1$, cf. (7.24), $N_{G-\text{coh}}^{(0)} \equiv 4\alpha_{0z}^2 = b_0^2$, so that $k_0^2 \sigma_S^2 N_{G-\text{coh}}^{(0)} \equiv k_0^2 b_0^2 \sigma_S^2 \ll 1$, then $\Delta_{RS}(\alpha_0) \equiv 0$, even when $2\alpha_0 - b_{TR} = 0$, as noted in (8.9c).

8.3 (Monostatic) Backscatter Intensities

For the incoherent backscatter intensity at "high frequencies," we get from (8.6) directly, with $2\alpha_{0x} = 0$, $2\alpha_{0y} = 2\sin\theta_{0T}$, ($\theta_{0T} = \pi/2$), and $b_{TR} \equiv 0$, the well-known result (with respect to the first term), cf. Tolstoy and Clay ([9], Eq. 6.75),

$$\boxed{M_{X-\langle X \rangle}^{(0)} \Big|_{\substack{\theta_{0T}=\pi/2 \\ \text{Hi-Freq} \\ \text{back}}} = G^{(1)} K_0(0)_{\text{in}} (g_T g_R)^2 \overline{R_0^2} \overline{S^2} A_1 \cdot \left[\frac{\pi e^{-\left\{ \frac{\tan^2 \theta_{0T}}{2\sigma_{Gy}^2} \right\}}}{\sigma_{Gx} \sigma_{Gy} \cos^4 \theta_{0T}} + \frac{k_0^4}{2} N_{GS}^{(0)}(2\alpha_0)_{\text{inc}} W_S(2\alpha_0 k_0 | 0) \right]}. \quad (8.10)$$

The coherent backscatter scatter intensity $M_{\langle X \rangle}^{(0)}(0)$ (8.7) vanishes, because of the high-frequency condition, $4\cos^2\theta_{OT} b_{00}^2 k_{00}^2 G^2 \gg 1$: the number of coherent "specular points," or facets, backscattering at θ_{OT} , and even as $\theta_{OT} \rightarrow 0$ (Snell angle), vanishes because of the extreme roughness of the surface. The contributions from the incoherent "specular points" (first-term of (8.10)) likewise rapidly vanish as $\theta_{OT} \rightarrow \pi/2$ (grazing), as their number, effective at θ_{OT} , becomes vanishingly small as $\theta_{OT} \rightarrow \pi/2$. This is not the case, of course, for the "tilted" contribution, of the small-scale soliton waves, since $N_{G-inc}^{(0)} > 0$, cf. (7.56a,b). Here, since $\alpha_{ox}=0$, $\alpha_{oy}=\sin\theta_{OT}$, $W_S(2\alpha_0 k_0|0) = W_S(0, 2k_0 \sin\theta_{OT}|0)$. Particular models for W_S , (7.41), are discussed in Section 3 preceding.

Similarly, in the "low-frequency" cases we use (8.9)-(8.9c) (where $\Delta_{RS}=0$), to get the incoherent backscatter intensity

$$M_{X-\langle X \rangle}^{(0)}(0) \Big|_{\substack{\phi_{OT}=\pi/2 \\ \text{Low-Freq} \\ \text{back}}} \doteq G^{(1)} K_0(0) \ln R_0^{-2} \bar{S}^2 (g_T g_R)^2 A_1 [8k_0^4 \cos^4\theta_{OT} W_G(0, 2k_0 \sin\theta_{OT}|0) + \frac{k_0^4}{2} N_{G-inc}^{(0)} W_S(0, 2k_0 \sin\theta_{OT}|0)] , \quad (8.11)$$

which reveals the expected first-order Bragg scatter terms ($\sim W_G, W_S$).

The corresponding coherent backscatter intensity is found directly from (8.7), with $b_{TR} \doteq 0$, viz.:

$$M_{\langle X \rangle}^{(0)}(0) \Big|_{\substack{\phi_{OT}=\pi/2 \\ \text{Low-Freq} \\ \text{back}}} \doteq G^{(1)} K_0(0) \ln R_0^{-2} \bar{S}^2 (g_T g_R)^2 A_1 k_0^2 \left[2A_1 \cos^2\theta_{OT} e^{-\frac{3k_0^2 \sin^2\theta_{OT}}{B}} \right] \doteq 0 \quad B \ll 1, \quad (8.12)$$

unless $\theta_{OT} = 0$ (vertical direction), whereupon (8.12) reduces at once to

$$M_{\langle X \rangle}^{(0)}(0) \Big|_{\substack{\phi_{OT}=\pi/2 \\ \text{Low Freq} \\ \text{back:Snell}}} \doteq 2G^{(1)} K_0(0) \ln R_0^{-2} \bar{S}^2 (g_T g_R)^2 A_1^2 k_0^2, \quad (\theta_{OT} = 0). \quad (8.12a)$$

8.4 (Bistatic) Scatter Intensities

With bistatic, or "forward" scatter, the facet terms vanish at high frequencies, except for a small case about the specular, or Snell angle, where $2\alpha_{oy} = 2\alpha_{ox} = 0$, cf. (5.29a), (5.30), since $\sigma_{Gx}^2, \sigma_{Gy}^2 \ll 1$, cf. (8.6), where these facet terms become

$$M_{X-\langle X \rangle}^{(0)}(0) \underset{\substack{\text{Hi Freq} \\ \text{Snell: } \phi_{OT} = \pi/2}}{\sim} \frac{-(2\alpha_{oy})^2 / b_o^2 \sigma_{Gy}^2}{\sigma_{Gx}^2 \sigma_{Gy}^2} \frac{\pi}{\sigma_{Gx}^2 \sigma_{Gy}^2}; (\alpha_{ox} = 0 = \alpha_{oy}), \quad \theta_{OT} < \pi/2, \quad (8.13)$$

cf. Bass and Fuks, ([1], Sec. 20, 1, 2, esp. Eqs. (20.28), (20.32); also [5], Eq. (13a), where $\gamma=0$ at the Snell angle). The complete high-frequency incoherent intensity, (8.6), with forward scatter at the Snell angle, so that (5.29a), (5.30) apply, becomes specifically for these two-scale surface models

$$M_{X-\langle X \rangle}^{(0)}(0) \underset{\substack{\text{Hi-Freq} \\ k_o^2 \gg 1 \\ \text{Snell}}}{\Big|}_{\phi_{OT} = \pi/2} \approx G^{(1)} K_o(0) \overline{R_o^2} \overline{S^2} (g_T g_R)^2 A_1 \left[\frac{\pi}{\sigma_{Gx} \sigma_{Gy}} + 8k^4 \cos^4 \theta_{OT} W_S(0,0|0) \right], \quad (8.14)$$

where by (7.56), $N_{G-inc}^{(0)} \rightarrow 16 \cos^2 \theta_{OT}$ and $\theta_{OT} < \pi/2$. For $\theta_{OT} \rightarrow \pi/2$, strong shadowing becomes dominant for the facet term, so that its contribution vanishes. The small-scale term likewise disappears (See [1], Sec 20, (2) for conditions). From (8.7), it is seen that the coherent term always vanishes at these high frequencies.

With bistatic ("forward") scatter at low frequencies (8.7), (8.9) apply. At the Snell angle, we again have $2\alpha_{ox} = 2\alpha_{oy} = 0$, $b_o = 2 \cos \theta_{OT}$, so that specifically ($\Delta_{RS} \doteq 0$)

$$M_{X-\langle X \rangle}^{(0)}(0) \underset{\substack{\text{Low Freq} \\ \text{Snell}}}{\Big|} \approx G^{(1)} K_o(0) \overline{R_o^2} \overline{S^2} (g_T g_R)^2 A_1 [8k_o^4 \cos^2 \theta_{OT} W_G(0,0|0) + \frac{k_o^4}{2} N_G^{(0)}(0)_{inc} W_S(0,0|0)], \quad (8.15a)$$

and

$$M_{\langle X \rangle}^{(0)}(0) \underset{\substack{\text{Low Freq} \\ \text{Snell}}}{\Big|} \approx 2G^{(1)} K_o(0) \overline{R_o^2} \overline{S^2} A_1^2 k_o^2 (g_T g_R)^2 \cos^2 \theta_{OT}. \quad (8.15b)$$

As we see from (7.36),

$$W_a(0,0|0) = \int K_a(\Delta r, 0) d(\Delta r) = n \ell_a^2 \sigma_a^2, \quad (8.16)$$

where $n = O(10^\circ)$, and ℓ_a is an (isotropic) correlation distance. (See Section 3 for a discussion.)

8.5 Scatter Intensity of the Diffuse Diffraction Term ($k=1$)

Applying (7.52) and (7.52a) to each term of (7.16) in (7.15), where we note that $\langle \Delta v_G^{(k)} \Delta v_S^{(k)} \rangle_R = \langle \Delta v_G^{(k)} \rangle_R \langle \Delta v_S^{(k)} \rangle_R = 0$, since the gravity wave and soliton components are postulated to be independent, we get directly, with the help of (7.52a):

$$M_{RT}^{(1)}(0|\dots) = \int_{-\infty}^{\infty} \overline{O_{RT}} \overline{O_{RT}^*} \overline{R_0^2} \overline{S^2} \left\langle \left[\left(\frac{\hat{i} \cdot \zeta_G}{n_z} \right)^2 |J_G| + \left(\frac{\hat{i} \cdot \zeta_S}{n_z} \right)^2 |J_S| \right] \right\rangle_{\zeta_G, \zeta_S, \text{etc.}} dr_1 \quad (8.16a)$$

where $|J_{G,S}| = |\zeta_{xx}\zeta_{yy} - \zeta_{xy}^2|_{G,S}$ = (absolute) curvature of each surface (G,S), cf. (7.52). Removing the $\overline{R_0^2} \overline{S^2}$ from under the integral sign as before, and using (7.3), (7.4) we get directly for (8.16a)

$$\begin{aligned} M_{RT}^{(1)}(0|\dots) &= \overline{R_0^2} \overline{S^2} I_3(0) \{ (1 + \sigma_{Gx}^2 + \sigma_{Gy}^2) |\overline{\zeta_G^2 J_G}| + |\overline{\zeta_S^2 J_S}| \} \\ &= (g_T g_R)^2 \overline{R_0^2} \overline{S^2} \frac{A_1}{2} \{ \overline{\zeta_G^2 |J_G|} + \overline{\zeta_S^2 |J_S|} \} \end{aligned} \quad (8.16b)$$

from (6.36), (6.40), (6.52): the fact that $I_3(0) = (g_T g_R)^2 A_1/2$, and the fact that $\sigma_{Gx}^2, \sigma_{Gy}^2 \ll 1$ along with the statistical independence of ζ_G , and (ζ_{Gx}, ζ_{Gy}) for gaussian processes (at the same point in space-time).

Accordingly, from (7.15) the desired diffuse scatter intensity ($k=1$) becomes

$$M_{X-\langle X \rangle}^{(1)}(0) = G^{(1)} K_0(0)_{in} (g_T g_R)^2 \frac{A_1}{2} [\overline{R_0^2} \overline{S^2} \{ \langle \zeta_G^2 |J_G| \rangle + \langle \zeta_S^2 |J_S| \rangle \}] \quad (8.17)$$

with $G^{(1)}$ given as before by (7.11a). As expected, these diffuse diffraction

terms (8.17) are (1), independent of frequency, and (2) independent of directionality: there is no focusing of the scattered energy or dependence on the angles of incidence and viewing, as in the "classical" case ($k=0$).

The former property, (1), stems from the "quasi-optical" character of the scattering regions around each stationary phase point on each surface, while (2) is likewise a consequence of the fact that the local surface has all possible slopes, considered over the ensemble of possible stationary phase points, so that there is no dominant subset of "specular points" at any given viewing angle (i.e., surface slope). This is quite different from the high-frequency, specular-point or "speckle" situation in the "classical" case ($k=0$), cf. (8.6), (8.10), (8.14), where only the stationary phase-points with comparatively large local flat (i.e., tangent-plane) areas (facets) are considered, sufficiently widely separated that their reflected signals undergo large phase changes, and such that $k_0 \rho \gg 1$, where $\rho (= \sqrt{r_1 r_2})$ is the effective radius of curvature (r_1, r_2 being the associated gaussian radii of curvature). Then it is possible to distinguish numbers of such facets at any specified angle (apart from very small grazing angles where shadowing conceals the facets), from which a resultant, directional incoherent radiation is observed, [5]. In our present "quasi-optical" cases ($k \geq 1$) we have $k_0 \rho \leq 1$, rather than $k_0 \rho > (>) 1$ for $k=0$, and there is no preferred direction of scattering ($k=1$). Directional scattering does, however, appear in the multiple-scatter terms ($k \geq 2$), in view of the directional character of the correlation function $R_{12}^{(k)}(r_1, t_1; r_2, t_2)$, cf. (7.53). See [41, II] for details.

8.6 Extension to Include Explicit Capillary Waves

In our preceding wave surface models, cf. (7.4b), we have not explicitly distinguished the "capillary wave" component (ζ_c) from the "gravity-wave" component (ζ_g) in the (single) continuous wave surface, ζ_g , cf. (7.3). Although the so-called capillary term (when present) is small vis-a-vis the gravity component and the separate, soliton ripples (ζ_s), it cannot be neglected at small grazing angles and high frequencies, where the "geometrical acoustic" or specular-point scatter term itself becomes vanishingly small.

Using (7.3) for ζ_g we consider first:

A. The Coherent Component ($k=0$)

Here we have now for (7.19) the following expression for the second-moment function:

$$M_{RT}^{(0)}(\infty|\dots) = \left| \left\langle \left(\frac{\hat{n} \cdot 2\alpha_0}{n_z} \right)_G e^{2ik_0\alpha_0 z \zeta_G} (1 + 2ik_0\alpha_0 \cdot \hat{n}_G \zeta_S + 2ik_0\alpha_0 \cdot \hat{i}_z \zeta_C - \frac{k_0^2}{2} [(2\alpha_0 \cdot \hat{n}_G)^2 \zeta_S^2 + (2\alpha_0 \cdot \hat{i}_z)^2 \zeta_C^2 + (\dots) \zeta_C \zeta_S] \dots) \right\rangle \right|^2 A_{RT} \quad (8.18)$$

With $\zeta_g, \zeta_c, \zeta_s$ taken to be statistically independent, with $\zeta_g + \zeta_c = \zeta_G$ gaussian*, so that ζ_G, ζ_{Gx} , etc. are likewise statistically independent, we see that (8.18) reduces to

$$M_{RT}^{(0)}(\infty|\dots) = |F_1(2i\alpha_0 k_0)_g \{-2\alpha_{0z} + \frac{k_0^2}{2} \sigma_{S \text{ GS-coh}}^{2N(0)} + \frac{k_0^2}{2} \sigma_{C \text{ GC-coh}}^{2N(0)} + \dots\}|^2 A_{RT} \quad (8.19)$$

where now

$$F_{1g} = \langle e^{2i\alpha_0 k_0 z \zeta_g} \rangle = \text{c.f. of } (-\zeta_g) (\doteq e^{-2\alpha_0^2 k_0^2 \sigma_g^2}), \text{ cf. (7.26).} \quad (8.19a)$$

The "tilt-factor" $N_{G\text{-coh}}^{(0)}$ is given by (7.22), (7.22a), (7.24). The "tilt-factor" $N_{C\text{-coh}}^{(0)}$ is obtained from

$$N_{C\text{-coh}}^{(0)} = \left\langle \left(\frac{\hat{n} \cdot 2\alpha_0}{n_z} \right)_G (\hat{i}_z \cdot 2\alpha_0)^2 \right\rangle_G = -(2\alpha_{0z})^3. \quad (8.20)$$

The other factors are given as before: cf. (7.25) for A_{RT} . Thus, (7.23) is extended now to

$$M_{RT}^{(0)}(\infty|\dots) = (2\alpha_{0z})^2 A_{RT} |F_{1g}|^2 e^{-k_0^2 \sigma_g^2 + k_0^2 \sigma_S^2 N_{G\text{-coh}}^{(0)} + k_0^2 \sigma_C^2 N_{C\text{-coh}}^{(0)}} \quad (8.21)$$

where we can drop the terms $k_0^2 \sigma_S^2 N_{G\text{-coh}}^{(0)}, k_0^2 \sigma_C^2 N_{C\text{-coh}}^{(0)}$ ($\ll 1$) in the exponent,

*Note that ζ_g, ζ_c are not individually gaussian, strictly, since ζ_c is certainly not gaussian. (However, in practice we may treat ζ_g as an approximately normal process, since ζ_c is small vs. ζ_g , usually, and $\therefore \zeta_g \doteq \zeta_G$.)

and $F_{1g} \doteq F_{1G}$, since $\sigma_G^2 \doteq \sigma_g^2$. Thus, for the coherent component of scattering $M_{<X>}^{(0)}(0)$ is now given by (8.7), with the exponential term of (8.21), which is practically replaced by $\exp(-b_0^2 k_0^2 \sigma_G^2)$, $\sigma_g^2 \doteq \sigma_G^2$.

B. The Incoherent Component ($k=0$)

Our modification of the preceding results [Sec. 7.3B et seq.] starts with (7.29). We employ the aforementioned technique of splitting the wave-number spectrum, discussed in Sec. 2.1 above. We begin by rewriting the exponent of (7.29) as

$$b_0^2 k_0^2 \sigma_G^2 (1 - \rho_G) = b_0^2 k_0^2 \sigma_G^2 (1 - \delta_g - \delta_c); \quad \delta_g + \delta_c = \rho_G; \quad \sigma_g^2 + \sigma_c^2 = \sigma_G^2, \quad (8.22)$$

where $\rho_G(0,0) = 1$ is truly normalized, but $\delta_{g,c}(0,0) < 1$. Further rewriting gives

$$b_0^2 k_0^2 \sigma_G^2 (1 - \rho_G) = b_0^2 k_0^2 \{ \sigma_g^2 (1 - \delta'_g) + \sigma_c^2 (1 - \delta'_c) \};$$

$$\delta'_g \equiv \frac{\sigma_G^2}{\sigma_g^2} \delta_g, \quad \delta'_c \equiv \frac{\sigma_G^2}{\sigma_c^2} \delta_c. \quad (8.23)$$

Now δ'_g, δ'_c are properly normalized. Accordingly, we have for (7.29)

$$\begin{aligned} F_{2G} &= \exp \{ -b_0^2 k_0^2 \sigma_G^2 (1 - \rho_G) \} = (\exp [-b_0^2 k_0^2 \sigma_g^2 (1 - \delta'_g)]) \{ 1 + k_0^2 b_0^2 \sigma_c^2 (1 - \delta'_c) + \dots \} \\ &= e^{-b_0^2 k_0^2 \sigma_g^2 (1 - \delta'_g)} \{ 1 + \sigma_c^2 \delta'_c - k_0^2 b_0^2 \sigma_c^2 + \dots \} \\ &\doteq e^{-b_0^2 k_0^2 \sigma_g^2 (1 - \delta'_g)} \{ 1 + k_0^2 b_0^2 \sigma_G^2 \delta'_c + \dots \}, \\ &\quad k_0^2 b_0^2 \sigma_c^2 \ll 1, \end{aligned} \quad (8.24)$$

since the capillary component is very small, even at high frequencies: $k_0 = 83.78 \text{ rad} \cdot \text{m}^{-1}$ ($\approx 20 \text{ kHz}$), $\cos 80^\circ = 0.174$, $\sigma_c = 0.5 \text{ mm}$. This gives $(k_0 b_0 \sigma_c)^2 = [(83.78) \cdot 2 \cdot 0.174 \cdot (5 \cdot 10^{-4})]^2 = 2.13 \cdot 10^{-4} \ll 1$, $= 5.33 \cdot 10^{-3}$ at 100 kHz, etc.

The covariance functions $\hat{\rho}_g, \hat{\rho}_c$ are specifically, from (2.3),

$$\sigma_{G\hat{\rho}_g}^2(\Delta r, \tau') = \int_{-\infty}^{\infty} W_g(\underline{k}|\tau') e^{-i\underline{k} \cdot \underline{\Delta r}} \frac{d\underline{k}}{(2\pi)^2} = \int_{-k_D}^{k_D} W_g(\underline{k}|\tau') e^{-i\underline{k} \cdot \underline{\Delta r}} \frac{d\underline{k}}{(2\pi)^2} \quad (8.25a)$$

$$\sigma_{G\hat{\rho}_c}^2(\underline{\Delta r}, \tau') = \int_{-\infty}^{\infty} W_c(\underline{k}|\tau) e^{-i\underline{k} \cdot \underline{\Delta r}} \frac{d\underline{k}}{(2\pi)^2} = \int_{k_D}^{\infty} W_c(\underline{k}|\tau') \cos \underline{k} \cdot \underline{\Delta r} \frac{d\underline{k}}{2\pi} \quad (8.25b)$$

Equation (7.31) is now extended to

$$\begin{aligned} \text{Eq. (7.31)} \doteq & \left(\frac{\alpha_{ox}^2 + \alpha_{oy}^2 + \alpha_{oz}^2}{\alpha_{oz}/2} \right)^2 F_{2g} + \left\langle \left(\frac{\hat{n}_1 \cdot 2\underline{\alpha}_0}{n_{z1}} \right)_G \left(\frac{\hat{n}_2 \cdot 2\underline{\alpha}_0}{n_{z2}} \right)_G \right\rangle b_0^2 k_0^2 \sigma_{G\hat{\rho}_c}^2 \\ & + k_0^2 N_{GS-inc}^{(0)} K_S(\underline{\Delta r}, \tau') , \end{aligned} \quad (8.26)$$

where $\zeta_{Gx,y}$ and ζ_c are independent (cf. remarks following (8.18a) above) and where $N_{GS-inc}^{(0)}$ is given by (7.32), (7.33), (7.65), (7.66), and

$$F_{2g} = e^{-b_0^2 k_0^2 \sigma_g^2 (1-\hat{\rho}_g')} \quad (8.27)$$

for the essentially gaussian "gravity-wave" component. [Since $\sigma_g^2 \doteq \sigma_G^2$ here, $\hat{\rho}_g' \doteq \hat{\rho}_g$ and $\hat{\rho}_g(0,0) \doteq 1$.]

With (8.26) as the argument in { } of (7.34a) we may proceed as in (7.35), to get now

$$\begin{aligned} M_{RT}^{(0)} = \overline{R_0^2} \overline{S^2} \left\{ \int_{-\infty}^{\infty} d(\underline{\Delta r}) I_3(\underline{\Delta r}) F_{2g}(\underline{\Delta r}, \tau) \left(\frac{\alpha_{ox}^2 + \alpha_{oy}^2 + \alpha_{oz}^2}{\alpha_{oz}/2} \right)^2 e^{2i\underline{k}_{\alpha_0} \cdot \underline{\Delta r}} \right. \\ + I_3(0) k_0^2 N_{Gc-inc}^{(0)} \int_{-\infty}^{\infty} \sigma_{G\hat{\rho}_c}^2(\underline{\Delta r}, \tau) e^{2i\underline{k}_{\alpha_0} \cdot \underline{\Delta r}} d(\underline{\Delta r}) \\ \left. + I_3(0) k_0^2 N_{GS-inc}^{(0)}(\underline{\alpha}_0) \int_{-\infty}^{\infty} K_S(\underline{\Delta r}, \tau) e^{2i\underline{k}_{\alpha_0} \cdot \underline{\Delta r}} d(\underline{\Delta r}) \right\} , \end{aligned} \quad (8.28)$$

where

$$N_{Go-inc}^{(0)}(\tau) = \left\langle \frac{\hat{n}_1 \cdot 2\alpha_0}{n_{z1}} \frac{\hat{n}_2 \cdot 2\alpha_0}{n_{z2}} \right\rangle_G b_0^2; \quad N_{Gc-inc}^{(0)}(0) = \left\langle \left(\frac{\hat{n} \cdot 2\alpha_0}{n_z} \right)_G^2 \right\rangle_G b_0^2 \equiv N_{GS-inc}^{(0)} \quad (8.28a)$$

At this point we proceed as in Section (8.1), using (8.25b) to write finally the extended version of (8.6):

$$\begin{aligned} (b_{TR} \neq 0) \quad M_{X-\langle X \rangle}^{(0)}(0) \Big|_{\substack{\text{"Hi-freq"} \\ k_{oA1}^2 \gg 1}} &= G^{(1)} K_0(0) \overline{R_0^2} \overline{S^2} (g_T g_R)^2 A_1 \\ &\cdot \left[\left\{ \left(\frac{\alpha_{ox}^2 + \alpha_{oy}^2 + \alpha_{oz}^2}{\alpha_{oz}/2} \right)^2 \frac{\pi}{b_{o\sigma Gx}^2 b_{o\sigma Gy}^2} e^{-\left[\frac{(2\alpha_{ox})^2}{2b_{o\sigma Gx}^2} + \frac{(2\alpha_{oy})^2}{2b_{o\sigma Gy}^2} \right]} \right. \right. \\ &\quad \left. \left. + \frac{k_o^4}{2} N_{Gc-inc}^{(0)} W_c(2\alpha_o k_o |_{x,y} | 0) \right\}_G \right. \\ &\quad \left. + k_o^4 N_{GS-inc}^{(0)}(0) W_S(2\alpha_o k_o |_{x,y} | 0) \right], \quad \sigma_g \doteq \sigma_G. \end{aligned} \quad (8.29)$$

The coherent component is given by (8.21) in (8.7) (with $\sigma_g \doteq \sigma_G$), for all frequencies.

$$\begin{aligned} M_{\langle X \rangle}^{(0)}(0) &= G^{(1)} K_0(0) \overline{R_0^2} \overline{S^2} (g_T g_R)^2 A_1 k_o^2 \left[(-2\alpha_{oz})^2 e^{-b_{o\sigma G}^2 k_o^2} \right. \\ &\quad \left. \cdot e^{-\frac{3k_o^2}{4} \left[\frac{(2\alpha_o - b_{TR})_x^2}{A} + \frac{(2\alpha_o - b_{TR})_y^2}{B} \right]} \right] \end{aligned} \quad (8.30)$$

Similarly, we find that the "low-frequency" version of (8.9) becomes

$$\begin{aligned} M_{X-\langle X \rangle}^{(0)}(0) \Big|_{\text{"Low-Freq"}} &\doteq G^{(1)} K_0(0) \overline{R_0^2} \overline{S^2} (g_T g_R)^2 A_1 \\ &\cdot \left[\left\{ \frac{k_o^4 b_o^4}{2} W_g(2\alpha_o k_o |_{x,y} | 0) + \frac{k_o^4}{2} N_{Gc}^{(0)}(2\alpha_o)_{inc} W_c(2\alpha_o k_o |_{x,y} | 0) \right\}_G \right. \\ &\quad \left. + \frac{k_o^4}{2} N_{GS}^{(0)}(2\alpha_o)_{inc} W_S(2\alpha_o k_o |_{x,y} | 0) \right], \end{aligned} \quad (8.31)$$

where $\Delta_{RS}(\alpha_0)$ is given by (8.9a,b), etc.

We can now specialize (8.29)-(8.31) to the various scatter geometries, as we may wish, e.g., "backscatter," forward scatter in the Snell direction, etc. The results appear as the various cross-sections presented in Sections 2, 3 above. Finally, for the diffraction terms, cf. Sec. 8.5, the extensions are directly made as given in Section 3.3.

9. References: Acoustic Scattering Cross Sections for Truly Composite Wind-Wave Surfaces: Scattering without Bubbles

- [1]. F. G. Bass and I. M. Fuks, Wave Scattering from Statistically Rough Surfaces (Trans. and Ed. by C. B. and J. F. Vesecky), Pergamon Press (New York), 1979. See Chapter 10 and references therein.
- [2]. L. Brekovskii and Y. Lysanov, Fundamentals of Ocean Acoustics, Springer Series in Electro-physics 8, Springer-Verlag (New York), 1982. See Sec. 1.6, Fig. 1.26, Chapter 9, and references.
- [3]. S. T. McDaniel and A. D. Gorman, "Acoustic and Radar Sea-Surface Backscatter," J. Geophysical Research, **87**, 4127-4136 (1982). Also, experimental references therein.
- [4]. _____, "Examination of the Composite-Roughness Scattering Model," JASA **73**, No. 5, May, 1983, pp. 1476-1486. See Fig. 4, also references therein.
- [5]. D. E. Barrick, "Rough Surface Scattering Based on the Specular Point Theory," IEEE Trans. Antennas and Propagation; Vol. AP-16, No. 4, July 1968, pp. 449-454. See also D. B. Barrick and E. Bahar, "Rough Surface Scattering Using Specular Point Theory," ibid., Vol. AP-29, No. 5, Sept., 1981, pp. 798-800.
- [6]. W. I. Roderick, High Frequency Acoustics Project, since 1982-, Naval Underwater Systems Center (NUSC), New London, Conn. 06320; (Code 10). Roderick reports high-frequency scattering data at up to 20 knots mean wind speeds without bubbles. More precisely, operating at vertical incidence ($\theta_{OT}=0$) the receiving system was (interior) noise-limited such that if bubbles were present in the volume below the water/air interface, their (back-)scattering

strength would have to be more than -47 db to be apparent. For the same ocean, and system conditions, at grazing angles of 9° ($\theta_{OT}=81^\circ$) the effects of bubbles in the volume would be discernable at scattering strengths $[-47 \text{ db} - (\cos 81^\circ)^{-1} \text{ db}] = -47+8 = -39 \text{ (dbs)}$ or larger, which compares with -30 db actually observed for surface scatter, cf. Table 3.2. (At pulse durations $O(\frac{1}{2} \text{ ms})$ the instantaneous scattering layer is $\frac{3}{4} \text{ m}$ thick.) No volume scatter at or above this level was noted. This indicates that the observed (backscatter) returns are well dominated by the surface scattering mechanisms.

- [7]. J. G. Zornig, P. M. Schultheiss, and J. Snyder, "Bistatic Surface Scattering Strength at Short Wavelengths," Tech. Rpt. CS-9, June 1977, ONR Contract N00014-75-C-1014.
- [8]. L. Fortuin, "The Sea Surface as a Random Filter for Underwater Sound Waves," Ph.D. Thesis, Delft Univ., Holland, 1973.
- [9]. I. Tolstoy and C. S. Clay, Ocean Acoustics, McGraw-Hill (New York), 1966. Chapter 6.
- [10]. C. W. Horton, Sr., "A Review of Reverberation, Scattering, and Echo Structure," JASA 51, 1049-1061, 1972.
- [11]. C. S. Clay and H. Medwin, Acoustical Oceanography, John Wiley (New York), 1977, Chapter 10, Appendix A-10.
- [12]. D. Middleton, "A Statistical Theory of Reverberation and Similar First-Order Scattered Fields. Parts I, II, IEEE Trans. Information Theory, Vol. IT-13, 372-392, 393-414 (1967); Parts III, IV, *ibid.*, Vol. IT-18, 35-67, 68-90 (1972). This is a quasi-phenomenological theory ("FOM" theory), whose key concept is the replacement of complex boundary conditions with point scatterers having suitable impulse response functions. (See [8], [10] for a discussion; also [13].)
- [13]. V. V. Ol'shevskii, Characteristics of Sea Reverberation, Plenum Press - Consultant's Bureau (New York), 1967. Russian original Nauka Press, Moscow, 1966.
- [14]. R. H. Mellen, Personal communication, 1984; see also [15]. (B-K Inc., 291 Shaw Street, New London, Conn. 06320.)
- [15]. W. L. Konrad, D. G. Browning, R. H. Mellen, "Doppler Spectra of Sea-Surface Backscatter at High Acoustic Frequencies," NUSC Tech. Document 6735, July 1, 1982, (New London Laboratories).

- [16]. J. Lighthill, Waves in Fluids, Cambridge University Press (New York), 1978, 1979; Sec. 2.12, pp. 463-469.
- [17]. O. H. Shemdin, "Wind-Generated Current and Phase Speed of Wind Waves," J. of Physical Oceanography, Vol. 2, 1972, pp. 411-419.
- [18]. A. H. Schooley, "Profiles of Wind-Created Water Waves in the Capillary-Gravity Transition Region," J. of Marine Research, Vol. 16, 1958, pp. 100-108.
- [19]. M. L. Banner and O. M. Phillips, "On Incipient Breaking of Small Waves," J. of Fluid Mechanics, Vol. 65, 1974, p. 647-656.
- [20]. J. Walker, "The Charm of Hydraulic Jumps, Starting with Those Observed in the Kitchen Sink," "The Amateur Scientist," in Scientific American, Vol. 299, pp. 176-186, April 1981.
- [21]. B. F. Kur'yanov, "The Scattering of Sound at a Rough Surface with Two Types of Irregularity," Soviet Journal of Physical Acoustics 8, No. 3, 252-257 (1962); in English, 1963. See [1], Chapter 10, and bibliography therein.
- [22]. D. E. Barrick and W. H. Peake, "A Review of Scattering from Surfaces with Different Roughness Scales," Radio Science, Vol. 3 (New Series), No. 8, August, 1968, pp. 865-868.
- [23]. E. Bahar, "Scattering Cross Sections for Composite Random Surfaces: Full Wave Analysis," Radio Science, Vol. 16, No. 6, Nov.-Dec., 1981, pp. 1327-1335.
- [24]. E. Bahar and D. Barrick, "Scattering Cross Sections for Composite Surfaces that Cannot be Treated as Perturbed-Physical Optics Problems," Radio Science, Vol. 18, No. 2, March-April, 1983, pp. 129-137.
- [25]. E. Bahar, D. E. Barrick, and M. A. Fitzwater, "Computations of Scattering Cross-Sections for Composite Surfaces and the Specification of the Wavenumber where Spectral Splitting Occurs," IEEE Trans. on Antennas and Propagation, Vol. AP-31, No. 5, Sept. 1983, pp. 698-709.
- [26]. B. Kinsman, Wind Waves, Prentice Hall (Englewood Cliffs, New Jersey), 1965, Section 3.6 and Eq. (3.6:20.1) for deep water.
- [27]. O. M. Philips, The Dynamics of the Upper Ocean, Cambridge University Press (New York), 1966. See Sec. 3.2 and Eq. 3.2.3, $d \rightarrow \infty$.

- [28]. Reference [1], Chapter 5.
- [29]. W. Bachman, "A Theoretical Model for the Backscattering Strength of a Composite-Roughness Sea Surface," JASA 54, No. 3, March, 1973, pp. 712-716. (Also references therein.)
- [30]. E. Bahar, "Scattering Cross-Sections for Random Rough Surfaces: Full Wave Analysis," Radio Science, Vol. 16, No. 3, pp. 331-341, May-June 1981.
- [31]. _____, "Resolution of the Discrepancies between Different Physical Optics Solutions for Rough Surface Scattering," JASA, Vol. 71, No. 6, June, 1982, pp. 1352-1358.
- [32]. C. Eckart, "The Scattering of Sound from the Sea Surface," JASA, Vol. 25, 566-570 (1953).
- [33]. Ref. [1], §33, Secs. 1-3, pp. 429-438.
- [34]. D. Middleton, "Doppler Effects for Randomly Moving Scatterers and Platforms," JASA 61, No. 5, May, 1977, pp. 1231-1250.
- [35]. C. S. Cox and W. H. Munk, "Measurement of the Roughness of the Sea Surface from Photographs of the Sun's Glitter," J. Optical Soc. of America, Vol. 44, No. 11, pp. 838-850, 1954.
- [36]. N. N. Galubin, "Backscattering of Sound by a Disturbed Sea Surface," Soviet Journal of Physical Acoustics, Vol. 22, 193-197 (1976) (English translation).
- [37]. J. G. Lilly and S. O. McConnell, "Surface Reverberation Measurements in Dabob Bay and the Open Ocean, JASA, Supplement 1, Vol. 63, 524, 1978.
- [38]. R. M. Hoover and F. E. Kaprocki, "Sound Backscattering in the Ocean at 25 and 60 kc," PSUORL NOrd 16597-24, Applied Research Laboratory, Penn State Univ., Univ. Park, PA, 1957.
- [39]. Ref. [27], Sec. 4.5.
- [40]. G. S. Brown, "Backscattering from a Gaussian-distributed, Perfectly Conducting Rough Surface," IEEE Trans. Antennas and Propagation, Vol. AP-26, no. 3, pp. 472-482, 1978; see also, *ibid.*, Vol. AP-26, no. 6, pp. 943-946, 1980.
- [41]. D. Middleton, "New Approaches to Scattering Theory for Linear Random Media, with Applications to Underwater Acoustics";
"Part I - Canonical Formulations, Innovations, and Operators";

"Part II - Statistical-Physical Models of the Scattering Operator";
"Part III - Examples: Volume and Surface Scattering."
(to be submitted to JASA, '84). A concise outline of highlights
is provided in [42], [43].

- [42]. _____, "The Underwater Medium as a Generalized Communication Channel," pp. 589-612 of Underwater Acoustics and Signal Processing, NATO Advanced Study Institute, August, 1980; D. Reidel Publishing Co., Dordrecht, Holland, 1981.
- [43]. _____, "Channel Characterization and Threshold Reception for Complex Underwater Acoustic Media," EASCON (IEEE), Sept. 29-Oct. 1, 1980, Arlington, Va.; Publication No. 0531-6863/80/0000-0171.
- [44]. E. Bahar, "Full-Wave Solutions for the Scattered Radiation Fields from Rough Surfaces with Arbitrary Slope and Frequency," IEEE Trans. Ant. and Propagation, Vol. AP-28, No. 1, pp. 11-21, January 1980, and references therein.
- [45]. D. Middleton, An Introduction to Statistical Communication Theory, McGraw-Hill (New York), 1960.
- [46]. H. W. Marsh and R. H. Mellen, "Boundary Scattering Effects in Underwater Sound Propagation," Radio Science, Vol. 1 (New Series), No. 3, March, 1966, pp. 339-346.
- [47]. A. C. Scott, F.Y.F. Chu, and D. W. McLaughlin, "The Soliton: A New Concept in Applied Science," Proc. IEEE, Vol. C1, No. 10, Oct. 1973, pp. 1443-1483. [See also the entire issues, No. 10.]

INITIAL DISTRIBUTION LIST

Addressee	No. of Copies
NOSC, Code 013 (Dr. E. Cooper)(3), 7133 (Dr. C. Persons), 5322 (Dr. J. Northrup), (Dr. F. Fisher, Dr. F. Speigs (Marine Physical Lab))	7
ONR, ONR-425 (Dr. M. McKisic, Dr. R. Fitzgerald, R. Obrochta), -411SP (Dr. N. Gerr), -410 (Dr. E. Wegman), -425 (Dr. Bradley)	6
NRL	1
ITS/NTIA: U.S. Dept. of Commerce, (Dr. A. Spaulding, D. Crombie, Dr. C. Rush)	3
ARL, UNIV OF TEXAS, (Dr. G. Wilson, G. Ellis, Prof. C. Horton)	3
DTIC	12
NAVPGSCOL (Prof. Herman Medwin (1))	2
Science Applications Inc. (W. Chadsey, Dr. R. Becherer, Dr. G. Stegan, Dr. Tatrow, M. J. Brackett Hersey)	5
Yale University, New Haven, CT (P. H. Schulthesis)	1
Scripps Inst. of Oceanography, La Jolla, CA (Dr. W. Munk)	1
ARL/PENN STATE, STATE COLLEGE (Dr. S. McDaniel)	1
"Cyberlink," Boulder, CO (Dr. P. McManamon)	1
ARL, Johns Hopkins (Dr. J. Apel)	1
WPL-NOAA (Wave Propagation Lab) (Dr. D. Barrick)	1
Johns Hopkins Univ., Dept. of Oceanography (Prof. O. Phillips)	1
Univ. of Wisconsin, Dept. of Geophysics (Prof. C. Clay)	1
Univ. of New Mexico, Dept. of Elec. Eng. (Prof. D. Petersen)	1
B-K Inc. (Dr. R. Mellen)	1
Univ. of Miami/RSMAS (Dr. F. Tappert)	1
Dr. David Middleton, New York, NY	10